Functional MR Imaging in prostate radiotherapy
relationship with prostate histology

Alie Borren

COLOPHON

Functional MR Imaging in prostate radiotherapy - relationship with prostate histology

ISBN: 978-90-393-6117-7
Author: Alie Borren
Cover design: Alie Borren and Wim van Est, department of Pathology, AMC
Layout: Eelco Roos, department of Pathology, AMC
Printed by: Ridderprint

This project was partly financially supported by the Dutch Cancer Society (grant no. UU-2009-4310).
Financial supported for the publication of this thesis was kindly provided by Röntgen Stichting Utrecht.

Functional MR Imaging in prostate radiotherapy
relationship with prostate histology

Functionele MRI voor prostaat radiotherapie
relatie met prostaat histologie

Proefschrift

ter verkrijging van de graad van doctor aan de Universiteit Utrecht
op gezag van de rector magnificus, prof. dr. G. J. van der Zwaan,
ingevolge het besluit van het college voor promoties
in het openbaar te verdedigen op
dinsdag 3 juni 2014 des middags te 2.30 uur

door

Aaltje Borren

geboren op 7 februari 1984
te Harderwijk

Promotoren:	Prof. dr. M. van Vulpen
	Prof. dr. P.J. van Diest
Copromotoren:	Dr. M.E.P. Philippens
	Dr. U.A. van der Heide

Contents

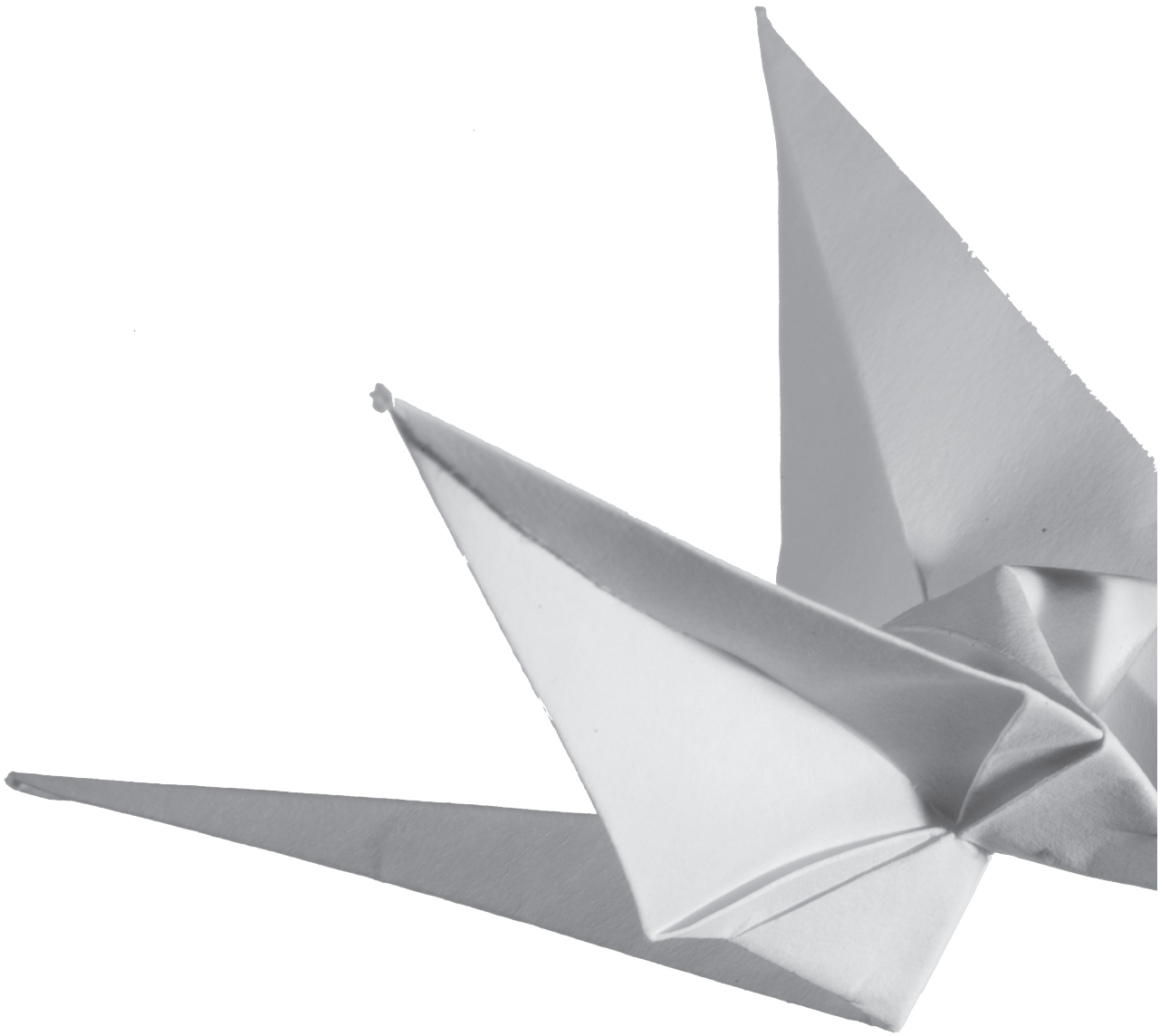

1

Introduction and thesis outline

Prostate cancer radiotherapy – Clinical perspective

Prostate cancer is the number one diagnosed malignancy in men, accounting for 11.428 (11%) newly diagnosed cancer patients in the Netherlands in 2011.[1] The incidence of prostate cancer increases with age, with most cases arising in men aged 65 years and older.[2] One out of every nine men will develop prostate cancer before the age of 80 years.

The clinical behavior of prostate cancer ranges from indolent to aggressive and fatal disease. According to serum prostate specific antigen (PSA) level, tumour stage and Gleason score, the disease is classified into low-, intermediate- and high-risk prostate cancer.[3]

Prostate cancer is a multifocal disease with two or more cancer foci in over 75% of all prostate cancer patients.[4-7] Treatment of prostate cancer is therefore targeted at the entire prostate gland. With surgery, the whole gland is removed, while with radiotherapy the whole gland is irradiated. In radiotherapy, the standard of care is to treat the entire prostate with a homogeneous radiation dose, irrespective of prostate cancer risk levels and irrespective of the location of the tumours. In patients with intermediate- to high-risk prostate cancer (PSA ≥10 ng/mL, Gleason score ≥7, or tumour stage ≥T2b) treatment with external beam radiotherapy (EBRT) results in 5-10 years biochemical progression free survival rates ranging from 50% to 85%.[8-11] This is significantly worse in comparison with outcome after EBRT of low-risk patients, in which 5-10 years biochemical progression free survival rates are reaching 95%.[11,12] Comparable survival rates are observed after treatment with brachytherapy.[13] In both patient groups, radiation treatment strategies might be improved. First, treatment outcome of patients with intermediate- to high-risk prostate cancer might be improved by increasing the radiation dose. Second, treatment of patients with low-risk prostate cancer might be improved by selectively treating the tumour area, instead of treating the entire prostate gland.

Irradiation of the whole prostate gland goes along with side effects due to unavoidable radiation dose to surrounding organs at risk such as rectum and bladder. This toxicity has negative impact on quality of life of prostate cancer patients. Focal treatment of the tumour area, while sparing normal tissue, might reduce toxicity in carefully selected patients with low-risk disease. In patients with unfavorable disease profiles, higher doses may be beneficial.[9,14-16] Dose escalation up to a dose of 86 Gy has been shown to improve biochemical progression free survival.[9-12,17,18] However, increasing the dose to the entire prostate will come with unacceptable toxicity due to high doses to surrounding organs at risk. Nevertheless, when exclusively boosted to a small area in the prostate, an ablative dose can be delivered, while sparing organs at risk.

A critical step in focal treatment is the selection of tumour areas. Among the multiple tumour foci in one prostate, there is mostly a dominant tumour focus present with regard to tumour volume. The location of the dominant tumour is important, as it determines disease outcome and local recurrences frequently originate at this site.[19-22] Additionally, to obtain optimal tumour control probability, boost areas may be selected based on specific tissue characteristics associated with tumour aggressiveness and radioresistance.[23] For example, high Gleason score, high

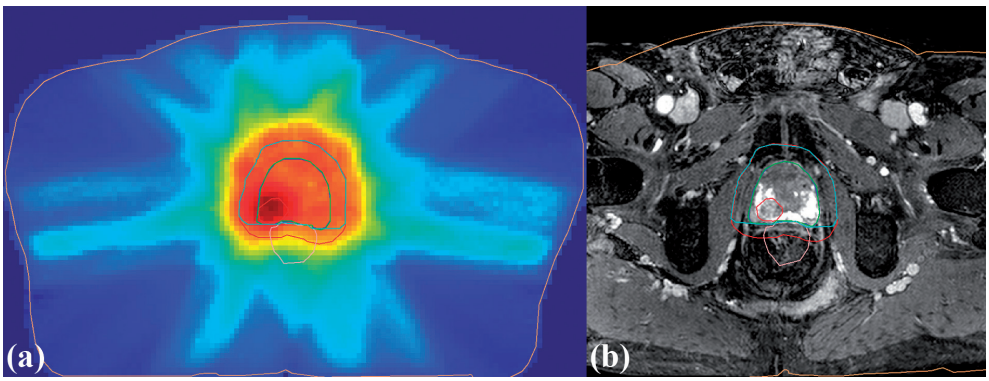

Figure 1. a) Dose plan with 95 Gy boost at the delineated tumour region in the peripheral zone of the prostate, with in b) the corresponding tumour delineation on MRI.

cell density, high microvessel density and hypoxic areas.[24-28] Several studies have shown that it is feasible to irradiate the dominant tumour with very high dose.[29,30] A recently started randomized phase III trial will show the benefit of a focal ablative boost to the dominant tumour (Figure 1).[31]

Multiparametric MRI for delineation of tumour areas

Accurate delineation of tumour areas is an essential and challenging element of focal treatment. It has been established that multiparametric magnetic resonance imaging (mp-MRI) is the modality of choice to localise prostate tumours.[32,33] High diagnostic performance is reached when anatomical T2w imaging is combined with functional techniques reflecting tissue characteristics and physiology, like diffusion-weighted imaging (DWI) and dynamic contrast-enhanced MRI (DCE-MRI).[34,35]

With DWI the random motion of free water molecules is measured. Increased cellularity and reduced extracellular space in prostate cancer restricts the free diffusional motion of water molecules, resulting in a reduction of the apparent diffusion coefficient (ADC).[36,37] In healthy prostate tissue, larger ducts and glandular structures allow less restricted diffusional motion, resulting in higher ADC values.

DCE-MRI is an imaging technique which visualizes the perfusion of tissue by dynamically imaging the distribution of a contrast agent. Neovascularisation in prostate tumours results in a disorganized network of many small and leaky blood vessels. The leakage of contrast agent from blood vessels into tumour tissue, and consequently the measured signal enhancement curves, will therefore be different from normal tissue. The signal enhancement is quantified using tracer kinetic models, of which for prostate the Tofts model is most common.[38] In this model, the parameters K^{trans} and k_{ep} describe the transfer of contrast agent from blood vessels

to prostate tissue and vice versa. The parameters v_e expresses the volume of extracellular extravascular space. Tumour tissue is associated with elevated K^{trans} and k_{ep} and with decreased v_e.
While in diagnostic setting mp-MRI is used to predict whether or not a patient has prostate cancer, the use of mp-MRI in the radiotherapy setting comes with new challenges. Target localization for treatment planning of focal boost areas puts higher demands on tumour detection accuracy. Every single voxel inside the prostate has to be assigned to either tumour or normal prostate tissue. In this way, the entire tumour area can be delineated accurately. From previous studies it is known that accurate delineation of tumour areas is difficult, as DCE-MRI and DWI often provide apparent inconsistent information about the precise tumour boundaries.[39] This can be due to heterogeneity of the tumour tissue, but also non-malignant prostate tissue can be very heterogeneous due to benign changes. Benign prostatic hyperplasia (BPH), cystic changes and prostatitis are frequently found in elderly men and might resemble tumour tissue in ADCs and K^{trans} values. Especially BPH is very common and considered normal with aging. The prevalence of BPH is >50% in men aged 60 years and older.[40] It is challenging to distinguish tumour from these benign changes.

Thesis outline

The main goal of this thesis is to understand the histological background of functional MR imaging of the prostate to come to robust and accurate delineation of tumour areas.
In current clinical practice, prostate tumour delineation is a manual procedure in which it is difficult to deal with the inconsistent information of the different MR images. To improve the robustness of MRI-based prostate tumour delineations, a statistical model is presented in chapter 2, predicting tumour presence on voxel level in the peripheral zone of the prostate. This model is developed on a group of radiotherapy patients and pathologically validated on a group of prostatectomy patients.
The diagnostic performance of the presented statistical model is high. Nevertheless, tumour voxel detection is not perfect. Certain tumour parts remain undetected and parts of the non-tumour peripheral zone are incorrectly assigned to tumour tissue. In chapter 3, the limitations in sensitivity and specificity of prostate tumour detection with the statistical model are explored in relation to the cell density and microvessel density of prostate tissue.
Although it is well known that regions with low ADC values are suspicious for prostate cancer, ADC maps can be rather vague and the interpretation is challenging. Small tumours and parts of tumours might be easily missed. For accurate tumour delineation including all tumour voxels, more information is needed about the relationship between ADC and histological variables on voxel level. Therefore, in chapter 4, a detailed comparison is performed between ADC maps and cell density and relative glandular area of benign and malignant prostate tissue.
The high prevalence of BPH in the central gland of the prostate poses an additional challenge in the differentiation of benign tissue from tumour. Therefore, in chapter 5 the radiological

and histological appearance of BPH is investigated and compared with tumour regions. Finally, in chapter 6 the relation between DCE-MRI parameters and the expression of hypoxia-inducible factor (HIF) -1α and HIF-2α is investigated. From recent studies it is known that the immunohistochemical expression of HIF is related to worse prostate cancer outcome.[28,41,42] Tumour areas with high HIF-expression might therefore be in need of more aggressive treatment with focal boost.

Summarized, this thesis addresses several aspects regarding prostate tumour voxel detection and delineation, in relation to histological characteristics.

References

1. The Netherlands Cancer Registry. Incidence of prostate cancer in The Netherlands 2011. *www.cijfersoverkanker.nl.* Jan 4, 2014.
2. Crawford ED. Understanding the epidemiology, natural history, and key pathways involved in prostate cancer. Urology 2009;73:S4-10.
3. Ash D, Flynn A, Battermann J, et al. ESTRO/EAU/EORTC recommendations on permanent seed implantation for localized prostate cancer. Radiother Oncol 2000;57:315-21.
4. Karavitakis M, Ahmed HU, Abel PD, Hazell S, Winkler MH. Anatomically versus biologically unifocal prostate cancer: a pathological evaluation in the context of focal therapy. Ther Adv Urol 2012;4:155-60.
5. Karavitakis M, Winkler M, Abel P, Livni N, Beckley I, Ahmed HU. Histological characteristics of the index lesion in whole-mount radical prostatectomy specimens: implications for focal therapy. Prostate Cancer Prostatic Dis 2011;14:46-52.
6. Chen ME, Johnston DA, Tang K, Babaian RJ, Troncoso P. Detailed mapping of prostate carcinoma foci: biopsy strategy implications. Cancer 2000;89:1800-9.
7. Meiers I, Waters DJ, Bostwick DG. Preoperative prediction of multifocal prostate cancer and application of focal therapy: review 2007. Urology 2007;70:3-8.
8. D'Amico AV, Chen MH, Renshaw AA, Loffredo M, Kantoff PW. Androgen suppression and radiation vs radiation alone for prostate cancer: a randomized trial. JAMA 2008;299:289-95.
9. Al-Mamgani A, Heemsbergen WD, Levendag PC, Lebesque JV. Subgroup analysis of patients with localized prostate cancer treated within the Dutch-randomized dose escalation trial. Radiother Oncol 2010;96:13-8.
10. Dearnaley DP, Sydes MR, Graham JD, et al. Escalated-dose versus standard-dose conformal radiotherapy in prostate cancer: first results from the MRC RT01 randomised controlled trial. Lancet Oncol 2007;8:475-87.
11. Spratt DE, Pei X, Yamada J, Kollmeier MA, Cox B, Zelefsky MJ. Long-term survival and toxicity in patients treated with high-dose intensity modulated radiation therapy for localized prostate cancer. Int J Radiat Oncol Biol Phys 2013;85:686-92.
12. Zietman AL, Bae K, Slater JD, et al. Randomized trial comparing conventional-dose with high-dose conformal radiation therapy in early-stage adenocarcinoma of the prostate: long-term results from proton radiation oncology group/american college of radiology 95-09. J Clin Oncol 2010;28:1106-11.
13. Hinnen KA, Battermann JJ, van Roermund JG, et al. Long-term biochemical and survival outcome of 921 patients treated with I-125 permanent prostate brachytherapy. Int J Radiat Oncol Biol Phys 2010;76:1433-8.
14. Pollack A, Zagars GK, Starkschall G, et al. Prostate cancer radiation dose response: results of the M. D. Anderson phase III randomized trial. Int J Radiat Oncol Biol Phys 2002;53:1097-105.
15. Morgan PB, Hanlon AL, Horwitz EM, Buyyounouski MK, Uzzo RG, Pollack A. Radiation dose and late failures in prostate cancer. Int J Radiat Oncol Biol Phys 2007;67:1074-81.
16. Zelefsky MJ, Yamada Y, Fuks Z, et al. Long-term results of conformal radiotherapy for prostate cancer: impact of dose escalation on biochemical tumor control and distant metastases-free survival outcomes. Int J Radiat Oncol Biol Phys 2008;71:1028-33.

17. Peeters ST, Heemsbergen WD, Koper PC, et al. Dose-response in radiotherapy for localized prostate cancer: results of the Dutch multicenter randomized phase III trial comparing 68 Gy of radiotherapy with 78 Gy. J Clin Oncol 2006;24:1990-6.

18. Kuban DA, Levy LB, Cheung MR, et al. Long-term failure patterns and survival in a randomized dose-escalation trial for prostate cancer. Who dies of disease? Int J Radiat Oncol Biol Phys 2011;79:1310-7.

19. Wise AM, Stamey TA, McNeal JE, Clayton JL. Morphologic and clinical significance of multifocal prostate cancers in radical prostatectomy specimens. Urology 2002;60:264-9.

20. Cellini N, Morganti AG, Mattiucci GC, et al. Analysis of intraprostatic failures in patients treated with hormonal therapy and radiotherapy: implications for conformal therapy planning. Int J Radiat Oncol Biol Phys 2002;53:595-9.

21. Pucar D, Hricak H, Shukla-Dave A, et al. Clinically significant prostate cancer local recurrence after radiation therapy occurs at the site of primary tumor: magnetic resonance imaging and step-section pathology evidence. Int J Radiat Oncol Biol Phys 2007;69:62-9.

22. Arrayeh E, Westphalen AC, Kurhanewicz J, et al. Does local recurrence of prostate cancer after radiation therapy occur at the site of primary tumor? Results of a longitudinal MRI and MRSI study. Int J Radiat Oncol Biol Phys 2012;82:e787-93.

23. Bentzen SM. Theragnostic imaging for radiation oncology: dose-painting by numbers. Lancet Oncol 2005;6:112-7.

24. Epstein JI. An update of the Gleason grading system. J Urol 2010;183:433-40.

25. Webb S, Nahum AE. A model for calculating tumour control probability in radiotherapy including the effects of inhomogeneous distributions of dose and clonogenic cell density. Phys Med Biol 1993;38:653-66.

26. Weidner N. Intratumor microvessel density as a prognostic factor in cancer. Am J Pathol 1995;147:9-19.

27. Mucci LA, Powolny A, Giovannucci E, et al. Prospective study of prostate tumor angiogenesis and cancer-specific mortality in the health professionals follow-up study. J Clin Oncol 2009;27:5627-33.

28. Vergis R, Corbishley CM, Norman AR, et al. Intrinsic markers of tumour hypoxia and angiogenesis in localised prostate cancer and outcome of radical treatment: a retrospective analysis of two randomised radiotherapy trials and one surgical cohort study. Lancet Oncol 2008;9:342-51.

29. Fonteyne V, Villeirs G, Speleers B, et al. Intensity-modulated radiotherapy as primary therapy for prostate cancer: report on acute toxicity after dose escalation with simultaneous integrated boost to intraprostatic lesion. Int J Radiat Oncol Biol Phys 2008;72:799-807.

30. Singh AK, Guion P, Sears-Crouse N, et al. Simultaneous integrated boost of biopsy proven, MRI defined dominant intra-prostatic lesions to 95 Gray with IMRT: early results of a phase I NCI study. Radiat Oncol 2007;2:36.

31. Lips IM, van der Heide UA, Haustermans K, et al. Single blind randomized Phase III trial to investigate the benefit of a focal lesion ablative microboost in prostate cancer (FLAME-trial): study protocol for a randomized controlled trial. Trials 2011;12:255.

32. Turkbey B, Mani H, Shah V, et al. Multiparametric 3T prostate magnetic resonance imaging to detect cancer: histopathological correlation using prostatectomy specimens processed in customized magnetic resonance imaging based molds. J Urol 2011;186:1818-24.

33. Padhani AR. Integrating multiparametric prostate MRI into clinical practice. Cancer Imaging 2011;11 Spec No A:S27-37.

34. Futterer JJ, Heijmink SW, Scheenen TW, et al. Prostate cancer localization with dynamic contrast-enhanced MR imaging and proton MR spectroscopic imaging. Radiology 2006;241:449-58.

35. Oto A, Kayhan A, Jiang Y, et al. Prostate cancer: differentiation of central gland cancer from benign prostatic hyperplasia by using diffusion-weighted and dynamic contrast-enhanced MR imaging. Radiology 2010;257:715-23.

36. Gibbs P, Liney GP, Pickles MD, Zelhof B, Rodrigues G, Turnbull LW. Correlation of ADC and T2 measurements with cell density in prostate cancer at 3.0 Tesla. Invest Radiol 2009;44:572-6.

37. Langer DL, van der Kwast TH, Evans AJ, et al. Prostate tissue composition and MR measurements: investigating the relationships between ADC, T2, K(trans), v(e), and corresponding histologic features. Radiology 2010;255:485-94.

38. Tofts PS, Brix G, Buckley DL, et al. Estimating kinetic parameters from dynamic contrast-enhanced T(1)-weighted MRI of a diffusable tracer: standardized quantities and symbols. J Magn Reson Imaging 1999;10:223-32.

39. Groenendaal G, van den Berg CA, Korporaal JG, et al. Simultaneous MRI diffusion and perfusion imaging for tumor delineation in prostate cancer patients. Radiother Oncol 2010;95:185-90.

40. Thorpe A, Neal D. Benign prostatic hyperplasia. Lancet 2003;361:1359-67.

41. Gravdal K, Halvorsen OJ, Haukaas SA, Akslen LA. Proliferation of immature tumor vessels is a novel marker of clinical progression in prostate cancer. Cancer Res 2009;69:4708-15.

42. Nanni S, Benvenuti V, Grasselli A, et al. Endothelial NOS, estrogen receptor beta, and HIFs cooperate in the activation of a prognostic transcriptional pattern in aggressive human prostate cancer. J Clin Invest 2009;119:1093-108.

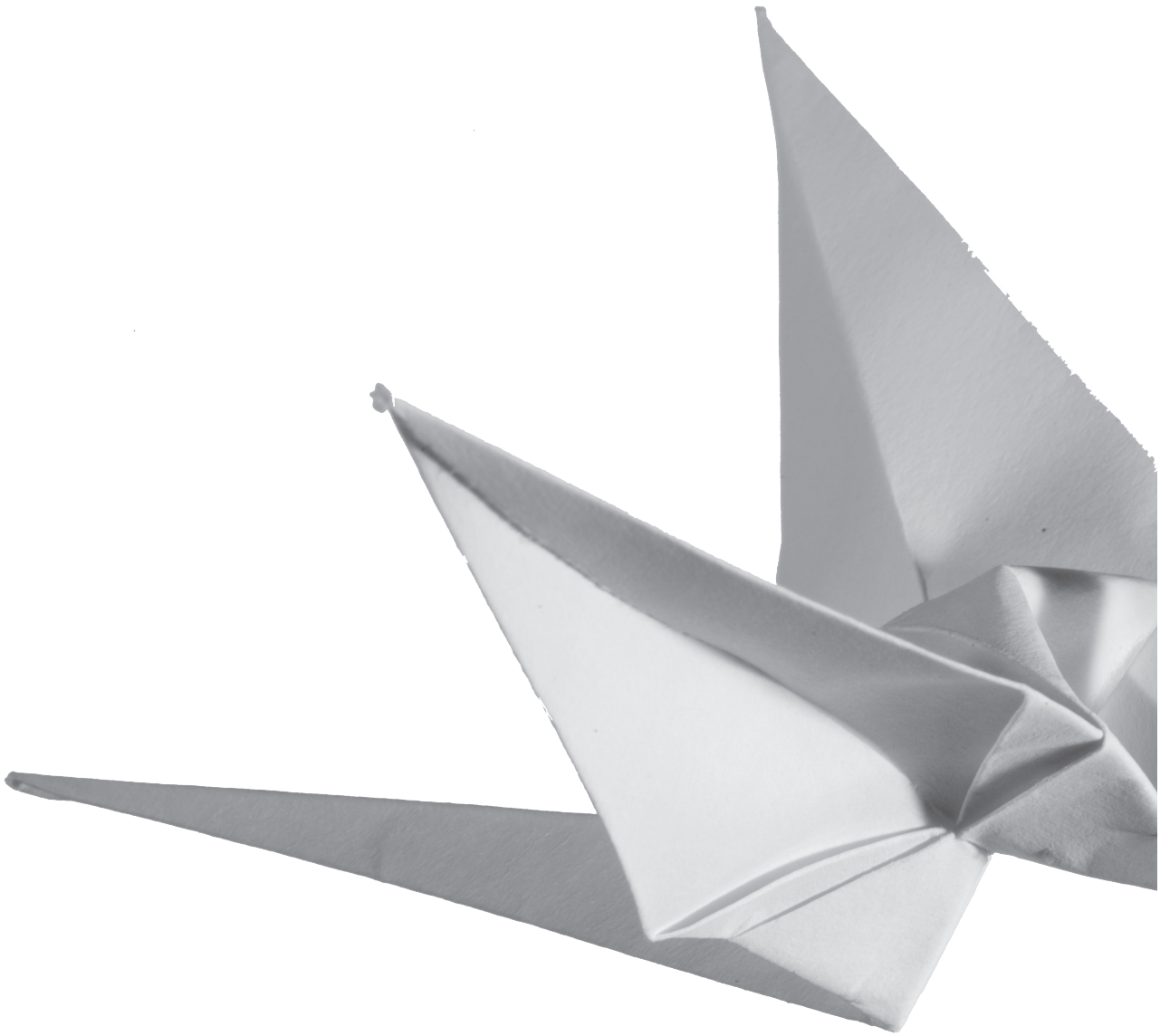

2

Pathologic validation of a model based on Diffusion-Weighted Imaging and Dynamic Contrast-Enhanced Magnetic Resonance Imaging for tumour delineation in the prostate peripheral zone

G. Groenendaal,
A. Borren,
M.R. Moman,
E. Monninkhof,
P.J. van Diest,
M.E.P. Philippens,
M. van Vulpen,
U.A. van der Heide.

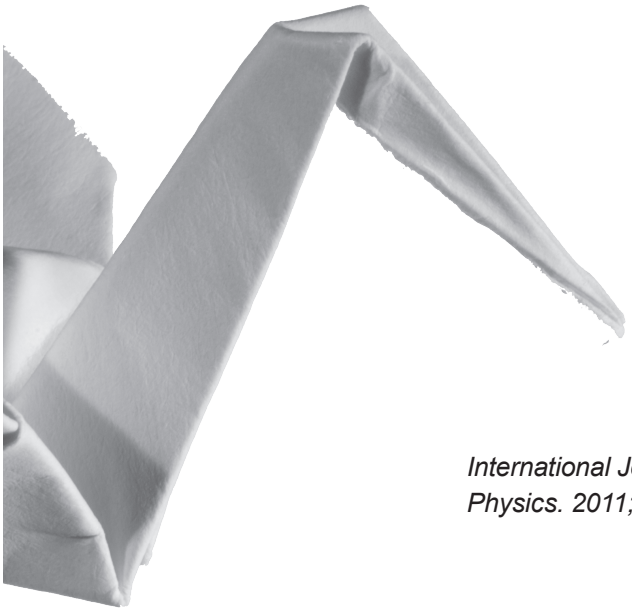

International Journal of Radiation Oncology, Biology and Physics. 2011;82:e537-e544

Abstract

Background

For focal boost strategies in the prostate, the robustness of magnetic resonance imaging-based tumour delineations needs to be improved. To this end we developed a statistical model that predicts tumour presence on a voxel level ($2.5 \times 2.5 \times 2.5$ mm^3) inside the peripheral zone. Furthermore, we show how this model can be used to derive a valuable input for radiotherapy treatment planning.

Materials and methods

The model was created on 87 radiotherapy patients. For the validation of the voxelwise performance of the model, an independent group of 12 prostatectomy patients was used. After model validation, the model was stratified to create three different risk levels for tumour presence: gross tumour volume (GTV), high-risk clinical target volume (CTV), and low-risk CTV.

Results

The model gave an area under the receiver operating characteristic curve of 0.70 for the prediction of tumour presence in the prostatectomy group. When the registration error between magnetic resonance images and pathologic delineation was taken into account, the area under the curve further improved to 0.89. We propose that model outcome values with a high positive predictive value can be used to define the GTV. Model outcome values with a high negative predictive value can be used to define low-risk CTV regions. The intermediate outcome values can be used to define a high-risk CTV.

Conclusions

We developed a logistic regression model with a high diagnostic performance for voxelwise prediction of tumour presence. The model output can be used to define different risk levels for tumour presence, which in turn could serve as an input for dose planning. In this way the robustness of tumour delineations for focal boost therapy can be greatly improved.

Introduction

Evidence is emerging that local recurrences of prostate cancer are often seen at the original tumour location.[1,2] This suggests that an additional boost dose to the tumour could improve the probability of tumour control. If the boost to the tumour volume is limited, the toxicity to the organs at risk may be kept at a minimal level.[3-6] Recently, a randomised Phase III trial was begun to test the clinical benefit of such a focal boost.[7]

Functional magnetic resonance imaging (MRI) techniques, such as diffusion-weighted imaging (DWI) and dynamic contrast-enhanced (DCE) MRI, may be used to guide tumour delineation inside the prostate. Both techniques can be used to distinguish tumour from healthy tissue.[8-13] Sensitivity levels range from 54% to 84% and from 59% to 87% for DWI and DCE-MRI, respectively. Specificity values for DWI and DCE-MRI range from 74% to 100% and from 74% to 84%.[8,9,12,13] In current clinical practice, delineation of prostate tumours is a manual procedure, wherein a radiation oncologist and a radiologist decide what to include in the target, based on the available images and clinical information. Interpretation of multiparametric images can be difficult, in particular when apparently conflicting information is obtained from different MRI techniques. Indeed, in an earlier study, we found that the overlap between regions identified as suggestive by DWI and DCE-MRI is quite limited.[14] A very simple approach to deal with this inconsistency was to define the region indicated by both modalities as suggestive as gross tumour volume (GTV). Regions identified by only one of the modalities could be interpreted as a high-risk clinical target volume (CTV). However, to improve the robustness of interpretation of the images, automated methods are required that translate multiparametric data into appropriate segmentations of the target volume.

To improve the robustness of MRI-based prostate tumour delineations for radiotherapy, we developed a statistical model that predicts tumour presence on a voxel level ($2.5\times2.5\times2.5$ mm^3) inside the peripheral zone (PZ). To make the model outcome applicable in a radiotherapy treatment setting, the outcome of the tumour prediction model was translated into discrete risk levels for tumour presence, which can be used as target volumes for treatment planning.

Materials and Methods

Study design

To improve the robustness of MRI-based prostate tumour delineations for radiotherapy, we first created a validated logistic regression model, which predicts tumour presence on a voxel level. After this we translated model outcome into discrete risk levels for tumour presence, which can be used as target volumes for treatment planning. To create a validated model, we performed two steps: model creation and model validation. Creation of the model was performed on 87 radiotherapy patients. From radiotherapy patients, a ground truth for the tumour delineations was not available. Therefore, validation could not be performed on this patient group. For the validation of the voxelwise performance of the model, an independent group of 12 prostatectomy patients was used.

To make the model applicable in a radiotherapy setting, after model validation, the model was stratified to create three different risk levels for tumour presence: GTV, high-risk CTV, and low-risk CTV.

Patients

The 87 consecutive radiotherapy patients were treated between April 2009 and July 2010. All patients had biopsy-proven prostate cancer and underwent DWI and DCE-MRI as part of standard clinical care. Patients using hormonal therapy were not included in this study because this therapy affects DCE-MRI images.[15]

The independent prostatectomy group consisted of 12 patients. The model validation on prostatectomy patients was approved by the institutional review board, and informed consent was obtained from all patients. The prostatectomy patients were included in the study between May 2005 and August 2010. Patient characteristics of the model creation group (radiotherapy patients) and the model validation group (prostatectomy patients) are summarised in Table 1.

Imaging

On all patients, a T2-weighted (T2w), balanced turbo field echo TFE, DWI, and DCE-MRI examinations were performed using a 3T Philips Achieva MR scanner. A six-element phased

Table 1. Patient characteristics

	Number of patients (%)	
Characteristic	**Model creation (radiotherapy patients)**	**Model validation (prostatectomy patients)**
Total	87	12
Primary tumour stage		
Tx	0 (0)	1 (1)
T1	38(44)	8 (75)
T2	29 (33)	3 (25)
T3	20 (23)	0 (0)
Gleason score		
6	54 (62)	4 (33)
7	31 (36)	4 (33)
8	0 (0)	3 (25)
9	2 (2)	1 (1)
PSA level (ng/mL) (range)	11 (3.1-70)	11.0 (4.3-29)
Age (y) (range)	67 (48-79)	62 (48-74)

PSA, prostate-specific antigen

array coil (sense cardiac) was used as a receive coil during the scans. The T2w images were acquired with a fast spin-echo sequence, repetition time/echo time TR/TE = 8,396/120 ms, echo train length 13, acquisition matrix 256×256, field of view (FOV) = 20 cm, slice thickness 3 mm, intersection gap 1 mm. Balanced TFE: TR/TE = 2.85/1.43 ms, echo train length = 40, acquisition matrix 192×249, FOV = 25 cm, slice thickness = 2 mm.

The DWI scans were performed by use of a multislice single shot spin-echo echo planar imaging SE-EPI sequence (FOV = 38 cm, slice thickness = 3 mm, EPI-factor = 47, intersection gap = 1 mm, TR/TE = 5,000/54 ms, acquisition matrix = 152×107, 9 averages, sense factor = 2 in anter-oposterior direction, phase encoding direction = posteroanterior, b values 300, 500, 1,000 s/mm^2).

The DCE-MRI protocol consisted of a three-dimensional spoiled gradient echo sequence (20 transverse partitions, 2.5 mm slice thickness, TR/TE = 4/1 ms, flip angle 8°, FOV = 40 cm, acquisition matrix = 160×160). Scans were repeated 120 times at 2.4-s intervals. A concentration of 0.1 mL/kg Gadobutrol (1.0M) (Gadovist, Schering AG, Berlin, Germany) contrast agent was injected with 2 mL/s, followed by a saline flush. Concentration of the contrast agent was calculated from the MR signal using preceding small flip angle scans (6, 16, and 32°, TR/TE = 50/1.1 ms). Before the application of a tracer kinetics model, a moving average filter of 3×3×3 voxels in the x, y, and z directions was used to increase the signal-to-noise ratio. Although high spatial frequency components were removed, this filtering step resulted in parameter maps with small voxels, which were useful for delineation and allowed the incorporation of K^{trans} maps in the voxelwise tumour prediction model.

For each voxel, the generalised kinetic model was fitted to the measured concentration time curves.[16] This yielded three-dimensional maps of the volume transfer constant K^{trans}. Owing to the extent of the measurement errors on the patient-specific input functions, a generic arterial input function (AIF) was used for all patients.

Model creation

In the radiotherapy group, highly suggestive and highly non-suggestive regions were delineated. This was done by an observer with 4 years of experience with the interpretation of functional MR images of the prostate. The delineation of highly suggestive volumes was based on hypointense values on the T2w, low apparent diffusion coefficient (ADC), high signal intensity on the b1000 image, and high K^{trans} values. Also, regions were delineated that were expected to be healthy on the basis of normal-appearing tissue on the T2w image, ADC, b1000, and K^{trans} values associated with healthy tissue. The voxels in these regions were used to create a logistic regression model that could be used for predicting the presence of tumour tissue. From each voxel inside the delineated volumes, the ADC and K^{trans} were retrieved, as were the minimum, median, mean, and maximum values in the adjacent 26 voxels (Table 2).

The absolute K^{trans} values depended largely on the AIF. Accurate measurement of the AIF was challenging because of the nonlinear relationship between signal and contrast agent concentration, T2*-effects at higher concentrations, B1-field inhomogeneities, and inflow artifacts.[17-20]

Therefore, K^{trans} values may vary between patients and institutes.[11,13,21] To overcome this, all K^{trans} maps were scaled to the median K^{trans} value in the total PZ before inclusion in the model. Furthermore, for each voxel, its relative position inside the prostate was retrieved from the MR scans. The relative z coordinate ranged from 0 for the most caudal slice to 1 for the most cranial slice. The relative x coordinate for each slice varied between 0 for the center of the prostate and 1 for the edge of the prostate. The relative y coordinate varied for each slide from 0 for the ventral side of the prostate to 1 for the most dorsal side of the prostate (Table 2). A logistic regression model was fitted to the data:

$$f(z) = \frac{1}{1 + e^{-z}}$$

where z is a linear combination of all included variables. Before inclusion in the model, the correlation between all variables was calculated. If the absolute Pearson correlation coefficient between two variables was larger than 0.8, only one of the two parameters was included in the logistic regression model. We started with the inclusion of all remaining parameters in the model (full model). Stepwise elimination of variables was performed based on the significance of the change in -2 log likelihood. The threshold of the p-value for removal was set to 0.15. Statistical analyses were performed using SPSS 16.0 (Chicago, IL).

Table 2. Variables retrieved from magnetic resonance imaging

Variable	Explanation
ADC_{voxel}	ADC value in voxel *i*
ADC_{mean}	Mean ADC value from voxel *i* and 26 surrounding voxels
ADC_{median}	Median ADC value from voxel *i* and 26 surrounding voxels
$ADC_{minimum}$	Minimum ADC value from voxel *i* and 26 surrounding voxels
$ADC_{maximum}$	Maximum ADC value from voxel *i* and 26 surrounding voxels
Relative K^{trans}_{voxel}	Relative K^{trans} value in voxel *i*
Relative K^{trans}_{mean}	Mean relative K^{trans} value in voxel *i* and 26 surrounding voxels
Relative K^{trans}_{median}	Median relative K^{trans} value in voxel *i* and 26 surrounding voxels
Relative $K^{trans}_{minimum}$	Minimum relative K^{trans} value in voxel *i* and 26 surrounding voxels
Relative $K^{trans}_{maximum}$	Maximum relative K^{trans} value in voxel *i* and 26 surrounding voxels
Relative x coordinate	Value from 0 (center of the prostate) to 1 (edge of the prostate)
Relative y coordinate	Value from 0 (ventral side of the prostate) to 1 (dorsal side of the prostate)
Relative z coordinate	Value from 0 (most caudal slice) to 1 (most cranial slice)

ADC, apparent diffusion coefficient

Model validation

To validate the model on prostatectomy patients, first the MR images of these patients needed to be registered to the corresponding sections stained with hematoxylin and eosin. For the first 5 patients, the prostatectomy specimens were processed and registered to the MR images as described in an earlier study.[22] The registration process was performed in three steps: 1) reconstruction of the prostate from the macroscopic slices; 2) registration of slices stained with hematoxylin and eosin to this reconstructed prostate; and 3) registration between the prostate reconstruction and the T2w MR image. On average, the registration error of this method was 2 to 3 mm.[22]

For Patients 6 through 12, the protocol was further improved. Before slicing, the prostate was first embedded in agarose gel (5%). This made it possible to cut the prostates of these patients in 3-mm slices. Furthermore, it allowed cutting the prostate at an angle similar to the angle seen on the T2w image. These improvements in the protocol decreased the registration error to 1.5 to 2.5 mm. For all patients, on average the registration error between the MR images and the histopathologic data was about 1 voxel. This error needs to be taken into account in validating the logistic regression model. Therefore, we used an approach that took into account the neighbouring voxels in the comparison of MR images with pathologic delineation. The assumption was that any displacement of tumour voxels by prostate specimen deformation would occur only from the original voxel to a neighbouring voxel (neighbouring approach). With this method, a tumour voxel was considered to correlate with suggestive imaging voxels even if it was present in a neighbouring voxel. This method was not used for healthy voxels. Using the neighbouring approach, for each patient a receiver operating curve (ROC) was created and the area under the curve (AUC) was calculated. To show the effect of the neighbouring approach, we also calculated the AUC without application of this method.

Derivation of tumour delineations based on model outcome

A logistic regression model has a continuous outcome. For the delineation of treatment volumes, this outcome needs to be stratified. We chose to define three risk levels for tumour presence: GTV, high-risk CTV, and low-risk CTV. For tumour boosting purposes, we chose to stratify the model outcome by choosing a threshold with a high tumour probability (high positive predictive value [PPV]) to define the GTV. In this way, only voxels with a high tumour probability would be boosted, keeping toxicity at minimal level. Voxels with a low tumour probability (high negative predictive value [NPV]) could be treated with the standard prostate dose. Voxels with an intermediate tumour probability were considered high-risk CTV. These voxels could also be boosted or safe margins could be applied around these prostate regions.

Tumour probability depends on tumour voxel prevalence. Therefore, to calibrate the model outcome, an estimate of the tumour voxel prevalence in a patient group is needed. To choose sensible thresholds that could be used for the definition of the GTV, high-risk CTV, and low-risk CTV, we plotted PPV and NPV curves for different model outcomes using the average tumour

Table 3. Regression coefficients for parameters in the logistic regression model

Variable	Regression coefficient
Constant	0.72
ADC_{voxel}	-4002.3
$ADC_{minimum}$	-1009.1
$ADC_{maximum}$	-1860.4
Relative K^{trans}_{voxel}	1.9
Relative $K^{trans}_{minimum}$	-0.7
Relative $K^{trans}_{maximum}$	2.8
Relative x coordinate	0
Relative y coordinate	3.0
Relative z coordinate	-1.5

ADC, apparent diffusion coefficient

voxel prevalence in the prostatectomy patient group. Furthermore, to illustrate the sensitivity of PPV and NPV curves for tumour voxel prevalence, we plotted PPV and NPV curves for a range of tumour voxel prevalences between 10% and 40%.

Results

Patients in the prostatectomy and radiotherapy groups were comparable in age and prostate-specific antigen (PSA) levels. The percentage of patients with lower T stage and higher Gleason score was larger in the prostatectomy group. The delineated suggestive and nonsuggestive regions had on average ADC values of $0.89 \times 10^{-3} \pm 0.28 \times 10^{-3}$ and $1.47 \pm 0.32 \times 10^{-3}$ and average normalised K^{trans} values of 2.05 ± 1.75 and 1.19 ± 2.74, respectively.

When correlating all possible input variables for the model, we found that maximum ADC and K^{trans} values in a kernel around a voxel of interest correlated strongly to the median and mean ADC and K^{trans} values in this kernel (Pearson correlation >0.8). Therefore, mean and median ADC and K^{trans} values were not incorporated in the model. From all other variables, only the relative x coordinate (lateral direction, Table 2) did not result in a significant change in the -2 log likelihood. The final model consisted of: the ADC and K^{trans} value in a voxel, the minimum and maximum of the ADC and K^{trans} in a kernel around this voxel, and the relative y (ventral-dorsal direction) and z (caudal-cranial direction) coordinates.

The regression coefficients of these variables are summarised in Table 3.

The model was validated in the prostatectomy patient group. An example of the model outcome is shown in Figure 1. The tumour as delineated by the pathologist is also shown. A good correspondence can be appreciated between the voxels predicted as suggestive by the model

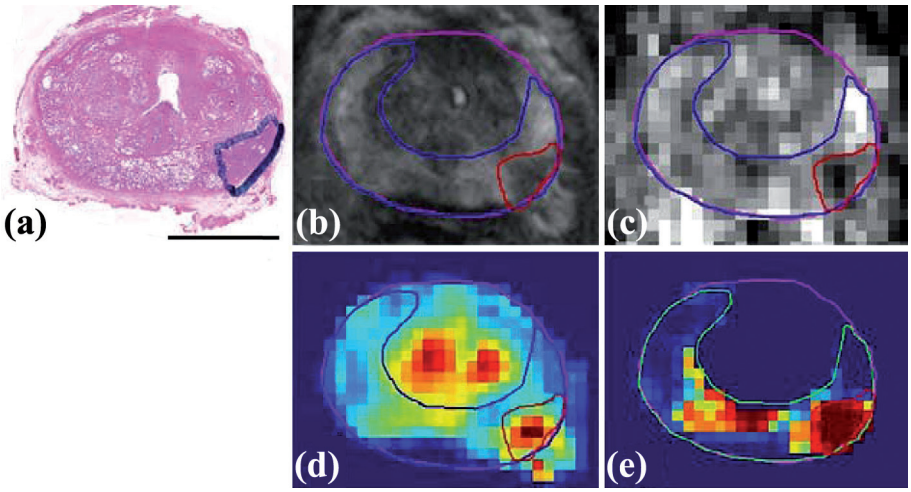

Figure 1. Patient example. (a) Hematoxylin and eosin stained section. (b) T2-weighted image. (c) Apparent diffusion coefficient map. (d) K^{trans} map. (e) Model outcome. Scale bar: 2.5 cm.

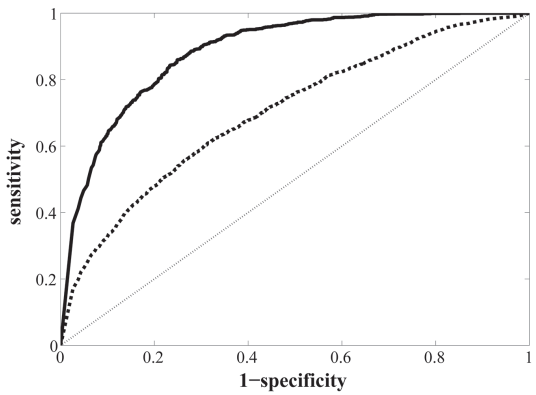

Figure 2. Average receiver operating curve for all patients.
The average area under the curve (AUC) was 0.89 when a method was applied to tissue deformation up to one voxel (black line). The average AUC was 0.70 when the compensation for tissue deformation was not applied (dashed line).

and voxels indicated as tumour voxels by the pathologist. The AUC retrieved from the ROC curve for this patient was 0.79. When the neighbouring approach was applied to compensate for registration errors up to one voxel, the AUC was 0.96. The average ROC curve yielded an AUC value of 0.70. When tissue deformations up to one voxel were compensated for, the AUC increased to 0.89 (Figure 2).

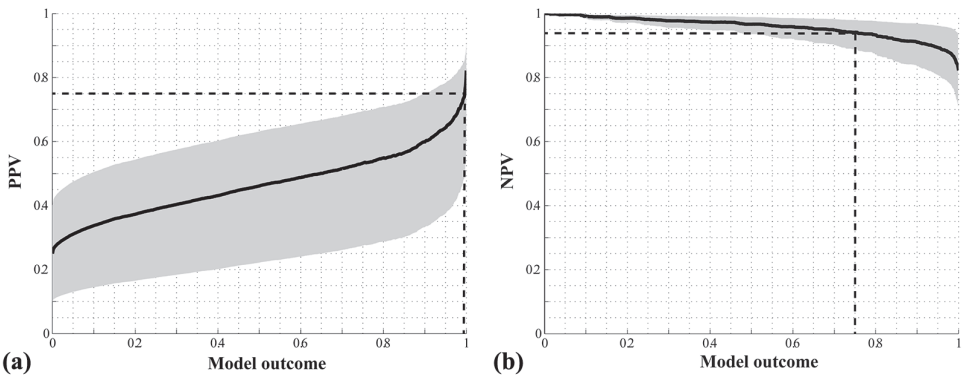

Figure 3. (a) Positive predictive value (PPV) and (b) negative predictive value (NPV) for different model outcomes. The black lines represent the PPV and NPV curves for the average tumour voxel prevalence found in the prostatectomy patient group (25%). The grey area represents the spread in these curves for tumour voxel prevalences ranging from 10% to 40% A model output with a high positive predictive value (>0.99) can be used to define a boost volume. Model outputs with a high negative predictive value (<0.72) can be used to define nonsuggestive tissue. The intermediate values (0.72-0.99) can be treated as high-risk clinical target volume.

To obtain appropriate thresholds, which can be used to define volumes for dose planning, PPV and NPV curves were plotted (Figure 3), where the black lines represent the PPV and NPV curves for the average tumour voxel prevalence in the prostatectomy patient group (25%). A model output of 0.99 was chosen to define the GTV on the basis of its high PPV. Voxels exceeding a model output of 0.99 had a tumour probability of 74%. Voxels with a model output between 0.72 and 0.99 were considered high-risk CTV. Voxels below the threshold of 0.72 had a high NPV. The risk of tumour presence in these voxels was only 5%.

The grey areas represent the spread in PPV and NPV curves for tumour voxel prevalences between 10% and 40%. Tumour voxel prevalence had only a minor effect on the NPV curve. The NPV for a threshold of 0.72 varied between 0.90 and 0.98. The PPV curve depended strongly on the tumour voxel prevalence (range, 0.48-0.85 for a threshold of 0.99). Nevertheless, given the strong increase in PPV toward the end of the PPV curve, a model outcome threshold above 0.99 to define the GTV seems appropriately independent of the exact tumour voxel prevalence. The sensitivity, specificity, PPV values, and NPV values of GTV and high-risk CTV are summarised in Table 4.

Applying the GTV and high-risk CTV thresholds for the different prostatectomy patients yielded the images in Figure 4. In these images can be seen that most of the voxels, which are considered as GTV based on model output, are confined to the tumour region. Furthermore, most of the tumour tissue is included in the high-risk CTV.

Table 4. Sensitivity, specificity, PPV and NPV of GTV and high-risk CTV

Region	High-risk CTV	GTV
Threshold model outcome	0.72	0.99
Sensitivity	0.89	0.48
Specificity	0.72	0.94
PPV*	0.26-0.68	0.48-0.85
NPV*	0.90-0.98	0.73-0.94

*for a tumour voxel prevalence between 10% and 40%.
PPV, positive predictive value; NPV, negative predictive value; GTV, gross tumour volume; CTV, clinical target volume.
Voxels with model outcome >0.99 are considered GTV and have a tumour probability of 0.48-0.85. Voxels with model outcome <0.99 have a NPV of 0.73-0.94.

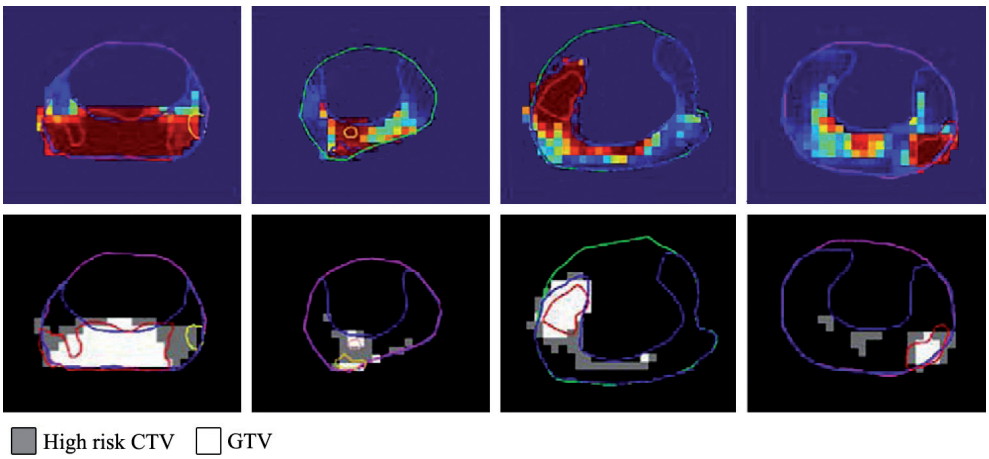

Figure 4. Model outcome translated to gross tumour volume (GTV) and high-risk clinical target volume (CTV) regions. The tumours delineated by the pathologist are shown in the figures. For compensating for registration errors for displaying these figures, the pathologic tumour delineation was shifted with a maximum of 1 voxel.

Discussion

To improve the robustness of MR-based prostate tumour delineations, we first developed a statistical model for the voxelwise (2.5×2.5×2.5 mm^3) prediction of tumour presence. Validation of this model on an independent prostatectomy patient group showed a high diagnostic performance in all patients (mean AUC = 0.89). This enabled objective interpretation of the functional MR images. To translate the model outcome to a useful input for radiotherapy dose planning, we thresholded the model to define three different risk levels for tumour presence: GTV, high-risk CTV, and low-risk CTV. These risk levels can be used for dose painting.

Ideally, a tumour prediction model would be created on a large group of prostatectomy patients. Instead, we used a large group of radiotherapy patients. Given the good performance of our model on an independent group of prostatectomy patients, we believe that our approach is justified. Prediction models have previously been developed for regions inside the prostate and on a voxelwise basis.[23-27] AUC values of the voxelwise models ranged between 0.71 and 0.82. These AUC values are hard to compare with our study because validation of the previous models was performed only on one slice per prostate.

The average error of our registration procedure is about the size of one voxel.[22] To take this error into account, we used a neighbouring method to calculate our sensitivity and specificity values. Without this method, fewer true positives and more false negatives would have been found. The method did not affect the number of true negatives and false positives. A similar method was applied by Turkbey et al. on 30 regions inside the prostate.[28]

The registration process complicates the validation of MR images with pathologic delineation. Different strategies have been applied to work around this problem, varying from performing validation on larger parts of the prostate, taking into account neighbouring regions, performing the validation only on selective regions, and manually transferring contours from pathologic delineation to the MR images.[23-28] Because of registration errors, the exact location of the border between tumour and healthy tissue on the MR images could not be validated with complete certainty. The large improvement in AUC (from 0.70 to 0.89) when the neighbouring voxels were taken into account strongly suggests that the mismatch between MR images and pathologic delineation was caused by errors in the registration process. However, even if the mismatch of one voxel between model outcome and pathologic delineation is not caused by registration errors, this does not have a large effect in radiotherapy practice. Because of the limited steepness in dose falloff, in radiotherapy practice a voxel next to a suggestive voxel would still receive a substantial dose.

At present our model is developed for PZ tissue only. The majority (~70%) of tumours are located in the PZ, which was confirmed by our own data. Because of the presence of benign hyperplasia, tumour detection is more challenging in the central gland. Therefore, most studies focus on the PZ, although promising sensitivity and specificity values for tumour detection in the central gland have been reported.[29]

We found a relatively high number of false positives close to the central gland. This can be partly explained by registration errors.

In this study we used relative instead of absolute K^{trans} values because K^{trans} values vary greatly between patients and institutes.[11,13,21] Using relative K^{trans} values gave more consistent results for the patients in our study. Another advantage of using relative values is that the method can be used more easily in other clinics. Using relative K^{trans} values based on median values in the PZ is a disadvantage when the percentage of tumour tissue inside the PZ exceeds 50%. In this situation, the median is no longer representative for healthy tissue. Using lower percentiles to scale the K^{trans} is an option. However, a better consensus between measurement protocols in different institutes and a more accurate measurement of the AIF would be more advantageous.

The patients in the radiotherapy and prostatectomy group differed in Gleason score and T stage. In our clinic, the model cannot be validated on clinical T3 tumours because patients with those tumours are generally not scheduled for prostatectomy.

To translate model outcome to a useful input for radiotherapy treatment planning, we created three different risk levels for tumour presence based on PPV and NPV, which depend on the tumour voxel prevalence in a patient. To show the sensitivity of PPV and NPV for tumour voxel prevalence, we plotted PPV and NPV curves for a range of tumour voxel prevalences. Independently from tumour voxel prevalence, a model outcome that exceeds 0.99 seems appropriate to define the GTV. Inasmuch as the NPV curve did not depend much on tumour voxel prevalence for the range studied, a model outcome between 0.72 and 0.99 seems appropriate to define a high-risk CTV. Nevertheless, in the future, stratification thresholds values may be adapted for different patient groups based on T stage, Gleason score, and PSA.

In contrast to PPV and NPV, sensitivity and specificity values did not depend on tumour voxel prevalence. We therefore expect that similar model AUC values will be found in different patients independently of T stage, Gleason score, and PSA.

In conclusion, we developed a logistic regression model for the prediction of tumour presence on a voxel level in the PZ of the prostate. This model has a high diagnostic performance and enables objective interpretation of the functional MR images. The model output can be used to define different risk levels for tumour presence, which in turn could serve as an input for dose planning. In this way the robustness of tumour delineations for focal boost therapy of the prostate can be greatly improved.

References

1. Cellini N, Morganti AG, Mattiucci GC, et al. Analysis of intraprostatic failures in patients treated with hormonal therapy and radiotherapy: implications for conformal therapy planning. Int J Radiat Oncol Biol Phys 2002;53:595-9.
2. Pucar D, Hricak H, Shukla-Dave A, et al. Clinically significant prostate cancer local recurrence after radiation therapy occurs at the site of primary tumor: magnetic resonance imaging and step-section pathology evidence. Int J Radiat Oncol Biol Phys 2007;69:62-9.
3. Pickett B, Vigneault E, Kurhanewicz J, Verhey L, Roach M. Static field intensity modulation to treat a dominant intra-prostatic lesion to 90 Gy compared to seven field 3-dimensional radiotherapy. Int J Radiat Oncol Biol Phys 1999;44:921-9.
4. van Lin EN, Futterer JJ, Heijmink SW, et al. IMRT boost dose planning on dominant intraprostatic lesions: gold marker-based three-dimensional fusion of CT with dynamic contrast-enhanced and 1H-spectroscopic MRI. Int J Radiat Oncol Biol Phys 2006;65:291-303.
5. Singh AK, Guion P, Sears-Crouse N, et al. Simultaneous integrated boost of biopsy proven, MRI defined dominant intra-prostatic lesions to 95 Gray with IMRT: early results of a phase I NCI study. Radiat Oncol 2007;2:36.
6. Miralbell R, Molla M, Rouzaud M, et al. Hypofractionated boost to the dominant tumor region with intensity modulated stereotactic radiotherapy for prostate cancer: a sequential dose escalation pilot study. Int J Radiat Oncol Biol Phys 2010;78:50-7.
7. Lips IM, van der Heide UA, Haustermans K, et al. Single blind randomized Phase III trial to investigate the benefit of a focal lesion ablative microboost in prostate cancer (FLAME-trial): study protocol for a randomized controlled trial. Trials 2011;12:255.
8. Gibbs P, Pickles MD, Turnbull LW. Diffusion imaging of the prostate at 3.0 tesla. Invest Radiol 2006;41:185-8.
9. Kumar V, Jagannathan NR, Kumar R, et al. Apparent diffusion coefficient of the prostate in men prior to biopsy: determination of a cut-off value to predict malignancy of the peripheral zone. NMR Biomed 2007;20:505-11.
10. Hosseinzadeh K, Schwarz SD. Endorectal diffusion-weighted imaging in prostate cancer to differentiate malignant and benign peripheral zone tissue. J Magn Reson Imaging 2004;20:654-61.
11. van Dorsten FA, van der Graaf M, Engelbrecht MR, et al. Combined quantitative dynamic contrast-enhanced MR imaging and (1)H MR spectroscopic imaging of human prostate cancer. J Magn Reson Imaging 2004;20:279-87.
12. Futterer JJ, Heijmink SW, Scheenen TW, et al. Prostate cancer localization with dynamic contrast-enhanced MR imaging and proton MR spectroscopic imaging. Radiology 2006;241:449-58.
13. Kozlowski P, Chang SD, Jones EC, Berean KW, Chen H, Goldenberg SL. Combined diffusion-weighted and dynamic contrast-enhanced MRI for prostate cancer diagnosis--correlation with biopsy and histopathology. J Magn Reson Imaging 2006;24:108-13.
14. Groenendaal G, van den Berg CA, Korporaal JG, et al. Simultaneous MRI diffusion and perfusion imaging for tumor delineation in prostate cancer patients. Radiother Oncol 2010;95:185-90.
15. Alonzi R, Padhani AR, Taylor NJ, et al. Antivascular effects of neoadjuvant androgen deprivation for prostate cancer: an in vivo human study using susceptibility and relaxivity dynamic MRI. Int J Radiat Oncol Biol Phys 2011;80:721-7.

16. Tofts PS, Brix G, Buckley DL, et al. Estimating kinetic parameters from dynamic contrast-enhanced T(1)-weighted MRI of a diffusable tracer: standardized quantities and symbols. J Magn Reson Imaging 1999;10:223-32.

17. Schabel MC, Parker DL. Uncertainty and bias in contrast concentration measurements using spoiled gradient echo pulse sequences. Phys Med Biol 2008;53:2345-73.

18. de Bazelaire C, Rofsky NM, Duhamel G, et al. Combined T2* and T1 measurements for improved perfusion and permeability studies in high field using dynamic contrast enhancement. Eur Radiol 2006;16:2083-91.

19. Roberts C, Little R, Watson Y, Zhao S, Buckley DL, Parker GJ. The effect of blood inflow and B(1)-field inhomogeneity on measurement of the arterial input function in axial 3D spoiled gradient echo dynamic contrast-enhanced MRI. Magn Reson Med 2011;65:108-19.

20. Cheng HL. T1 measurement of flowing blood and arterial input function determination for quantitative 3D T1-weighted DCE-MRI. J Magn Reson Imaging 2007;25:1073-8.

21. Ocak I, Bernardo M, Metzger G, et al. Dynamic contrast-enhanced MRI of prostate cancer at 3 T: a study of pharmacokinetic parameters. AJR Am J Roentgenol 2007;189:849.

22. Groenendaal G, Moman MR, Korporaal JG, et al. Validation of functional imaging with pathology for tumor delineation in the prostate. Radiother Oncol 2010;94:145-50.

23. Ozer S, Langer DL, Liu X, et al. Supervised and unsupervised methods for prostate cancer segmentation with multispectral MRI. Med Phys 2010;37:1873-83.

24. Liu X, Langer DL, Haider MA, Yang Y, Wernick MN, Yetik IS. Prostate cancer segmentation with simultaneous estimation of Markov random field parameters and class. IEEE Trans Med Imaging 2009;28:906-15.

25. Langer DL, van der Kwast TH, Evans AJ, Trachtenberg J, Wilson BC, Haider MA. Prostate cancer detection with multi-parametric MRI: logistic regression analysis of quantitative T2, diffusion-weighted imaging, and dynamic contrast-enhanced MRI. J Magn Reson Imaging 2009;30:327-34.

26. Artan Y, Haider MA, Langer DL, et al. Prostate cancer localization with multispectral MRI using cost-sensitive support vector machines and conditional random fields. IEEE Trans Image Process 2010;19:2444-55.

27. Vos PC, Hambrock T, Hulsbergen-van de Kaa CA, Futterer JJ, Barentsz JO, Huisman HJ. Computerized analysis of prostate lesions in the peripheral zone using dynamic contrast enhanced MRI. Med Phys 2008;35:888-99.

28. Turkbey B, Pinto PA, Mani H, et al. Prostate cancer: value of multiparametric MR imaging at 3 T for detection--histopathologic correlation. Radiology 2010;255:89-99.

29. Oto A, Kayhan A, Jiang Y, et al. Prostate cancer: differentiation of central gland cancer from benign prostatic hyperplasia by using diffusion-weighted and dynamic contrast-enhanced MR imaging. Radiology 2010;257:715-23.

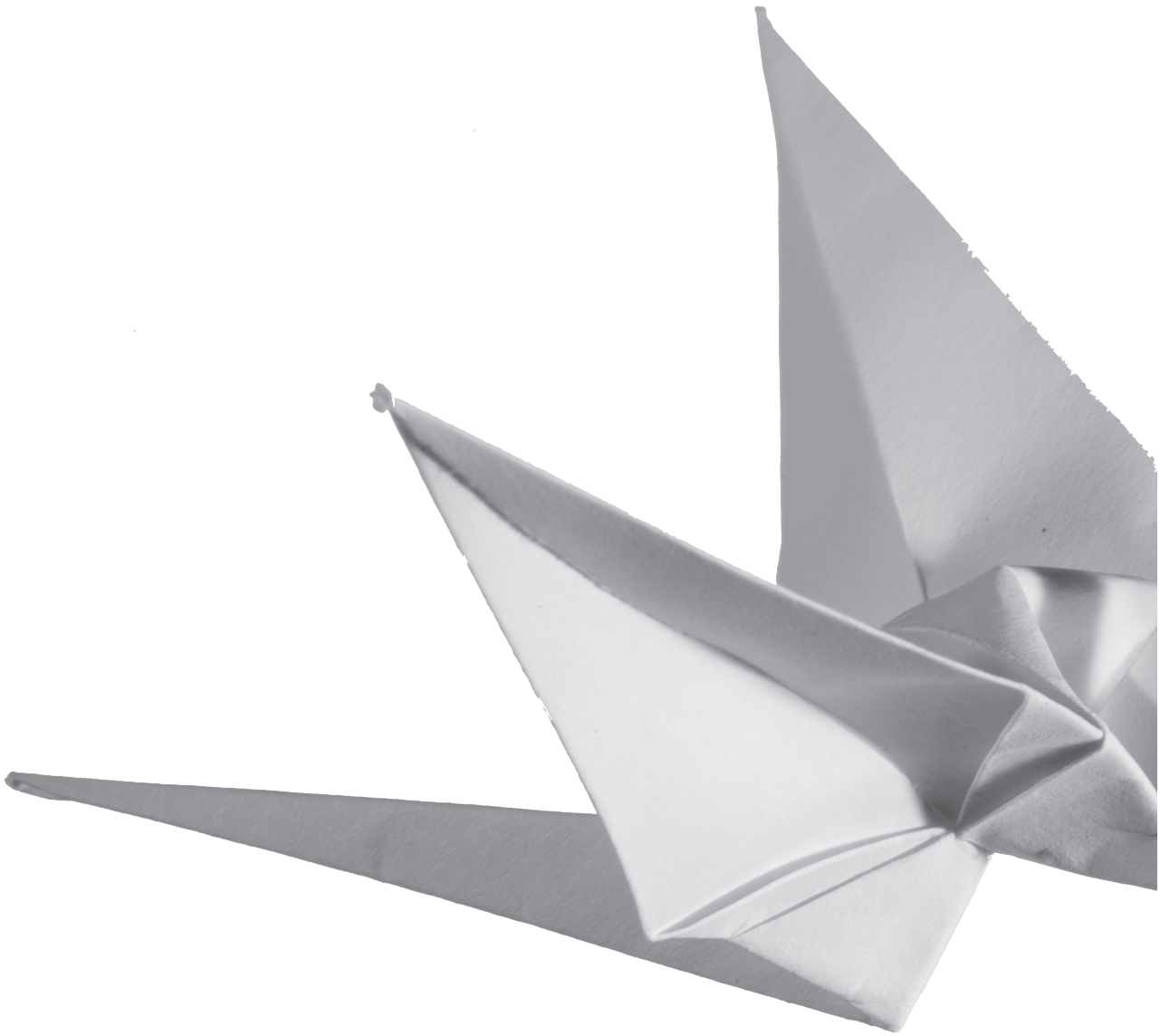

3

Accurate prostate tumour detection with multiparametric magnetic resonance imaging: Dependence on histological properties

A. Borren,*
G. Groenendaal,*
M.R. Moman,
A.E. Boeken Kruger,
P.J. van Diest,
M. van Vulpen,
M.E.P. Philippens,
U.A. van der Heide.

** these authors contributed equally to this work*

Acta Oncologica. 2014;53:88-95

Abstract

Background

To benefit most of focal treatment of prostate tumours, detection with high precision of all tumour voxels is needed. Although diffusion-weighted imaging (DWI) and dynamic contrast-enhanced magnetic resonance imaging (DCE-MRI) have good diagnostic performance, perfect tumour detection is challenging. In this study, we investigated the variation in prostate tissue characteristics Gleason score (GS), cell density (CD) and microvessel density (MVD) to explain the limitations in tumour voxel detection with a MRI-based logistic regression model.

Materials and Methods

Twelve radical prostatectomy patients underwent a pre-operative 3.0T DWI and DCE-MRI exam. The MRI scans were used to calculate voxel-wise tumour probability with a logistic regression model for the peripheral zone (PZ) of the prostate. Tumour probability maps were correlated and validated with whole-mount histology. Additionally, from the whole-mount histological sections CD, MVD and GS were retrieved for every single voxel. GS, CD and MVD of true- and false-positive voxels and of true- and false-negative voxels were compared using Mann-Whitney U-tests.

Results

False-negative tumour voxels had significantly lower CD and MVD ($p < 0.0001$) and were similar to non-tumour PZ. True-positive detected tumour voxels had high CDs and MVDs ($p < 0.0001$). In addition, tumour voxels with higher GS showed a trend towards more frequent detection ($p = 0.06$). Tumour voxels with GS $\geq$ 3+4 showed higher CD and MVD compared to tumour voxels with GS 3+3 ($p < 0.0001$).

Conclusions

Tumour voxels with low CD and MVD resemble healthy tissue and are limiting tumour voxel detection using DWI and DCE-MRI. Nevertheless, the most aggressive tumour voxels, containing high CD, MVD and GS, are more likely to be detected and can therefore be treated with high dose using focal therapy or focal boosting.

Introduction

Evidence is emerging that local recurrences of prostate tumours after radiotherapy are often seen at the original tumour site.[1] Therefore, an additional radiation boost dose to this tumour could improve the tumour control probability. By limiting the boost to the visible tumour, radiation toxicity to the organs at risk such as rectum and bladder may be minimized.[2,3] Treatment side effects can be reduced with targeted focal therapy to the index lesion only without treating the whole prostate gland.[4] In this case it is essential that all significant cancer is detected to allow for proper selection of patients for focal therapy. Treatment strategies like focal boosting and focal therapy therefore require precise delineation of the entire tumour area.

Diffusion weighted imaging (DWI) and dynamic contrast-enhanced magnetic resonance imaging (DCE-MRI) have a high sensitivity and specificity for tumour detection.[5,6] However, the use of multiparametric MRI in radiotherapy clinic requires improved tumour detection accuracy. First, on voxel level, DCE-MRI and DWI appear to provide complementary information about the presence of tumour, which, however, does not always point exactly at the same tumour locations. Second, the performance of simple thresholding of MR imaging parameters such as K^{trans} and maps of apparent diffusion coefficients (ADCs) is insufficient for accurate delineation of all tumour voxels.[7]

To deal with these challenges, in a previous study, we created a logistic regression model based on DWI and DCE-MRI.[8] This model had a high diagnostic performance (AUC=0.89). However, certain tumour parts remained undetected and parts of the non-tumour peripheral zone (PZ) were incorrectly assigned as tumour tissue. The explanation for these limitations may be found in the tissue's cell density and microvessel density, as the MR techniques DWI and DCE-MRI are believed to reflect these tissue properties.[9-11] Both non-tumour RPZ tissue and prostate tumour tissue can be highly heterogeneous with regard to these characteristics, affecting tumour detectability.[12]

In this study, the limitations in sensitivity and specificity of tumour voxel detection with a logistic regression model are explored in relation to the cell density (CD) and microvessel density (MVD) of malignant and benign PZ tissue of the prostate. Furthermore, the limitations in sensitivity are related to the GS.

Materials and Methods

Patients

This study was approved by the institutional review board and informed consent was obtained from all patients. Twelve patients were included in this study. All patients had biopsy proven prostate cancer and were scheduled for a Robotic Assisted Laparoscopic Prostatectomy (RALP). Clinical characteristics are shown in Table 1.

Table 1. Patient characteristics

Characteristic		Value
Patient age (years)*		63 (48-74)
PSA level (ng/ml)*		14.1 (6.3-29)
Pathological tumour stage#	T2a	2 (17%)
	T2c	3 (25%)
	T3a	7 (58%)
Gleason score#	3+3=6	4 (33%)
	3+4=7	5 (42%)
	3+5=8	3 (25%)

*median and (range); #patient numbers

Imaging

Prior to prostatectomy all patients underwent a T2w, balanced TFE, DWI and DCE-MRI exam using a 3T Philips Achieva MR scanner (Philips, Best, The Netherlands). To prevent prostate deformations, no endorectal coil was used. Before the MR exam, a urinary catheter was inserted to visualise the urethra in order to facilitate registration of MR-images and histological slices.
T2w images were acquired with a fast spin-echo sequence, TR/TE = 8396/120 ms, echo train length 13, acquisition matrix 256×256, field of view (FOV) = 20 cm, slice thickness 3 mm, intersection gap 1 mm, number of slices 25.
Balanced TFE: TR/TE = 2.85/1.43 ms, acquisition matrix 192×249, FOV = 25 cm, slice thickness = 2 mm, number of slices 90. A 6-element phased array coil (sense cardiac) was used as receive coil during the scans.
DWI scans were performed using a multislice single shot SE-EPI sequence (FOV = 38 cm, slice thickness = 3 mm, intersection gap = 1 mm, TR/TE = 5000/54 ms, acquisition matrix = 152×107, EPI-factor = 47, 9 averages, phase encoding direction = PA, SENSE factor = 2, b values 0, 300, 500, 1000 s/mm^2). ADC values were calculated after exclusion of the perfusion sensitive b = 0 data.
The DCE-MRI protocol consisted of a 3D spoiled gradient echo sequence (20 transverse slices, 2.5 mm slice thickness, TR/TE=4/1 ms, flip angle 8, FOV = 40 cm, acquisition matrix = 160×160). Scans were repeated 120 times at 2.4 s interval. A concentration of 0.1 ml/kg of Gadubutrol (1.0M) (Gadovist, Schering AG, Berlin, Germany) contrast was injected with 2 ml/s, followed by a saline flush. The tracer kinetics data were analyzed with the Tofts model and yielded 3D K^{trans} parameter maps.[13] The absolute values of K^{trans} depend largely on the arterial input function (AIF). Several factors make accurate measurement of the AIF challenging: the non-linear relationship between signal and contrast agent concentration, T2*-effects at higher concentrations, B1-field inhomogeneities and inflow-artifacts.[14-17] Due to the extent of the measurement errors on the patient specific input functions, a generic AIF was used, derived from a separate group of patients for which a phase-based AIF was obtained.[18] However, as

a result, absolute K^{trans} values may not be comparable between patients. To overcome this, all K^{trans} maps were scaled to the median K^{trans} value in the PZ. This results in dimensionless values of K^{trans} [min^{-1}/min^{-1}].

Logistic regression model

In a previous study, a logistic regression model was developed, which can be used for predicting the presence of tumour tissue. Experienced observers delineated highly tumour suspicious regions and healthy regions on MRI scans of radiotherapy patients. Tumour suspiciousness was based on hypointense values on T2w scans, low ADC and high K^{trans} values. The voxels in these regions were used to create the model. The final model consisted of: the ADC and K^{trans} value in a voxel, the minimum and maximum of the ADC and K^{trans} in a kernel around this voxel and the relative y (ventral-dorsal direction) and z (caudal-cranial direction) coordinate. The model was validated on a group of prostatectomy patients and yielded high diagnostic performance (mean AUC = 0.89). The continuous model outcome, ranging from 0 to 1, was stratified based upon the positive- and negative-predictive values. A threshold of 0.72 was used, which resulted in a sensitivity of 0.89 and a specificity of 0.72 for voxel-wise tumour detection.[8]

Histopathology

After prostatectomy, the left and right prostate surfaces were inked with different colours. The whole prostate was fixed in formaldehyde for approximately two days. Three carbon rods were inserted in the prostate specimen to facilitate the registration process after slicing of the prostate. Subsequently, we cut the prostate into slices of 3 mm. The precise thickness of these macroscopic slices was verified with a digital vernier caliper. Finally, whole-mount microscopic sections of 4mm were cut from the macroscopic paraffin embedded slices and stained with haematoxylin-eosin (H&E). A pathologist delineated the tumour areas on the H&E sections. Each tumour region was assigned with a GS in consensus by two observers. Digital photographs were taken of the macroscopic slices and the H&E sections including delineations were digitised using a flatbed scanner (Epson Expression 10000XL).

Registration between histopathology and MR images

To compare the MR data with histopathology, the MR images were registered to the H&E sections, as described previously by Groenendaal et al.[13] Three steps were performed: 1) registration of the H&E sections to the macroscopic slices; 2) 3D reconstruction of the prostate specimen from the macroscopic slices; and 3) registration between the prostate reconstruction and the T2w MR images. On average the registration error of this method was 2-3 mm.[13] For the last eight patients, the protocol was improved by embedding the prostate in agarose gel (5%) prior to slicing, to match for the sectioning plane of the prostate and the MRI plane. This improvement decreased the registration error with approximately 0.5 mm. For all patients, the registration error between the MR images and histopathology was on average about 1 voxel (reconstructed voxel size 2.5×2.5×2.5 mm^3).[13]

Immunohistochemical vessel staining

Tissue sections were deparaffinised, endogenous peroxidase activity was blocked and antigen retrieval was performed. Sections were incubated with an anti-CD31 monoclonal antibody (mouse-anti-human CD31, Novocastra). Subsequently, sections were incubated with HRP-conjugated secondary antibody (Novolink Polymer Detection System, Leica Microsystems) and diaminobenzidin and counterstained with hematoxylin. Throughout, appropriate positive and negative controls were used.

Tissue evaluation

Three microscopic slices per patient, containing the dominant tumour nodule and normal PZ, were chosen for further analysis and digital whole-slide images at microscopic resolution were created. Analysis of CD and MVD was performed in a grid of 2.5×2.5 mm^2, corresponding to the MRI voxels. The H&E stained sections were used for the determination of the CD. With the IHC Nuclear Algorithm v8 in ImageScope v10.0 (Aperio Technologies, Vista, CA, USA) the absolute number of cell nuclei per voxel was identified. Minimum detectable nuclear size was set at 20 μm^2. The Microvessel Analysis Algorithm v1 was used to identify CD31-stained blood vessels. The minimum vessel area threshold was set at 50 μm^2 to ignore aspecific background staining. To compensate for variation in staining intensity, the settings of the algorithms were evaluated qualitatively and optimised for every batch by adjusting them on test regions.

Data analysis

The registration error of about one voxel (2.5×2.5×2.5 mm^3) results in a misalignment between the suspicious region on the MR images and the tumour on the H&E stained sections. This may result in incorrect classification of voxels as either false negative or false positive. To exclude false-positive voxels from the data, non-tumour voxels were only taken into account if all the neighboring voxels contained non-tumour PZ tissue only. This correction method, however, results in a large reduction in the number of eligible voxels. For tumour, the amount of remaining voxels was considered too small for analysis. For tumour voxels we therefore chose an alternative approach to compensate for the registration error: we considered a tumour voxel as correctly detected when at least one neighboring voxel contained tumour tissue. This approach was previously used by Turkbey et al. on a regional level.[19]

CD and MVD were compared for the true-positive, false-negative, false-positive and true-negative voxels. For these analyses a Mann-Whitney U-test was used (SPSS version 16.0, SPSS, Chicago, IL, USA). We used a Kruskal-Wallis test to determine if MR tumour detectability was related to GS. Furthermore, we tested if CDs and MVDs differed for GS = 3+3 and GS ≥ 3+4, using a Mann-Whitney U-test. The Bonferroni method was used to correct for multiple testing, p-values $<0.05/5 = 0.01$ were considered significant.

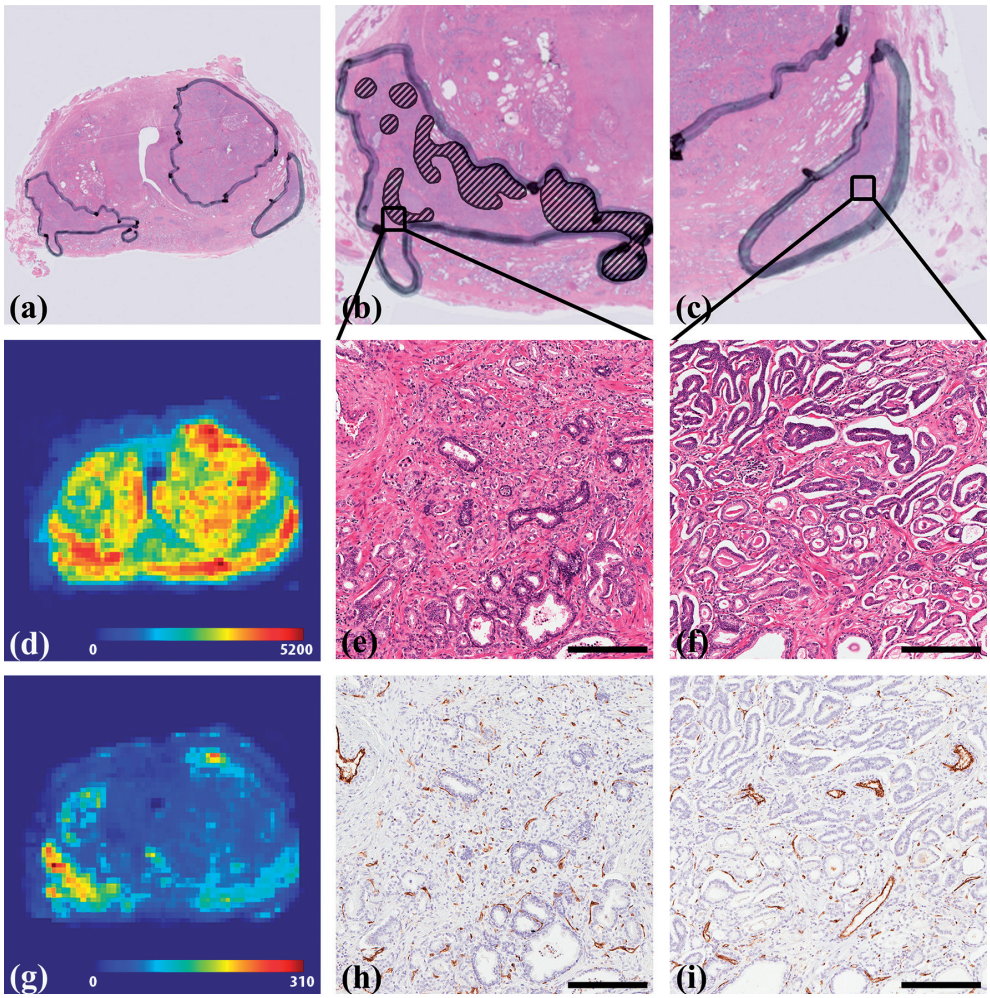

Figure 1. Example of histological parameters retrieved from the prostate slices. (a) Overview of H&E stained slice. (b) Detailed image of the right tumour. Gleason grade 4 components are delineated. The rest of the tumour consists of grade 3 components only. (c) Detailed image of the left tumour. This tumour consists only of Gleason grade 3 components. (d) Overview of the distribution of cell densities in the prostate slice (cells/mm^2). A large heterogeneity can be appreciated. (e) Detailed zoom of the H&E staining from the right tumour. Gleason grade 3 (lower left) and 4 (upper right) are both present in this image. The whole image has a size of 1 mm^2, which is the same as the pixel size in (d). (f) Detailed zoom of H&E staining of the left tumour. A large difference in microscopic structure between image (e) and (f) can be appreciated. (g) Overview of the distribution of microvessel densities in the prostate slice (vessels/mm^2). A large heterogeneity can be appreciated. (h) Detailed zoom of the CD31 microvessel staining from the right tumour. This image contains a relatively large number of small vessels (brown staining). (i) Detailed zoom of CD31 staining from the left tumour. A large difference in microscopic structure between image (h) and (i) can be appreciated. More large vessels are shown in (i) compared to (h). Scale bars: 250 µm.

Results

The detailed and heterogeneous data in this study is illustrated in two figures. In Figure 1, the histopathological properties of one prostate slice are depicted. The figure shows that prostate (tumour) tissue can be highly heterogeneous, both on the CD and MVD level. Especially on MVD, both PZ tumours are very different (Figure 1g). The heterogeneity in tissue characteristics is partly reflected by differences in Gleason patterns within a single tumour (Figure 1b). Given the relatively large voxel sizes on MRI, MR voxels are likely to show a mixture of different CD, MVD and Gleason patterns.

Figure 2 shows an example of the relation between the MR images and the spatial distribution of CD and MVD. In this figure an ADC map (a) and K^{trans} map (b) are shown, as well as the prediction of the logistic regression model(c). On these images two tumours are delineated. The left tumour has on average a low ADC (0.93×10^{-3} mm^2/s) and a high normalised K^{trans} (3.2). The right tumour consists of high ADC values (mean 1.2×10 mm^2/s) and low K^{trans} values (mean 1.1), associated with healthy tissue. Due to its low ADC and high K^{trans}, the left tumour was detected and even overestimated by the logistic regression model (Figure 2c). In contrast, a large part of the right tumour was not detected by the logistic regression model. The two tumours also differed on CD and MVD (Figure 2e and f). The left tumour consists of voxels

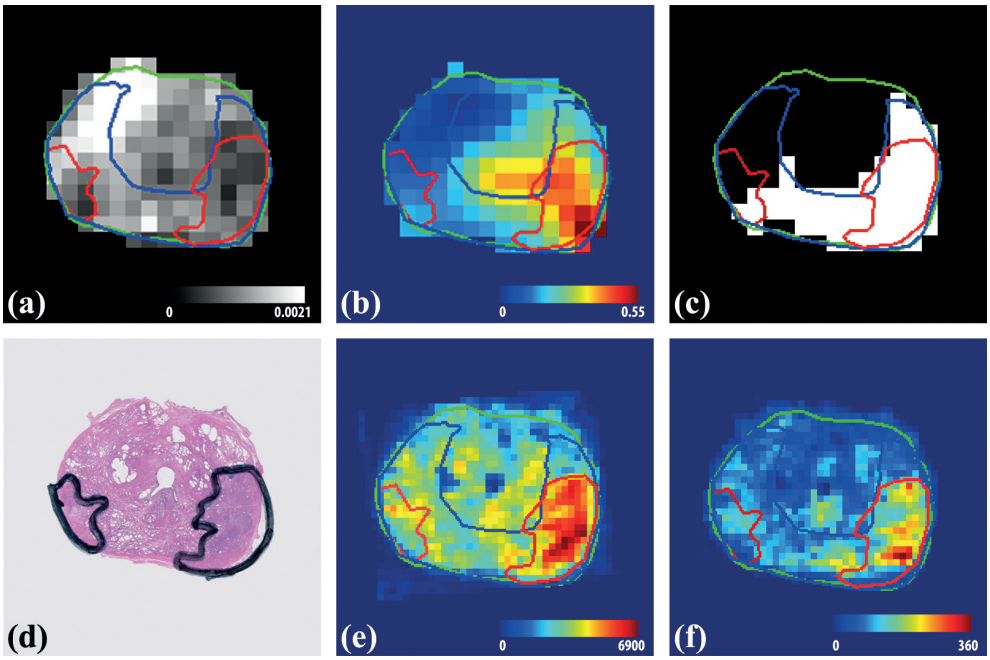

Figure 2. (a) ADC map (mm^2/s). (b) Ktrans map (min^{-1}). (c) stratified model outcome, where white is assigned to be tumour and black is assigned to be non-suspicious. (d) H&E stained section. (e) cell density (cells/mm^2). (f) microvessel density (vessels/mm^2). The left tumour is detected by the model and has a high cell and microvessel density and a Gleason score of 3+4. In contrast, the right tumour is not detected and has a low cell density and microvessel density and a Gleason score of 3+3. Cell density and microvessel density are for the image sampled on resolution of 1x1 mm^2.

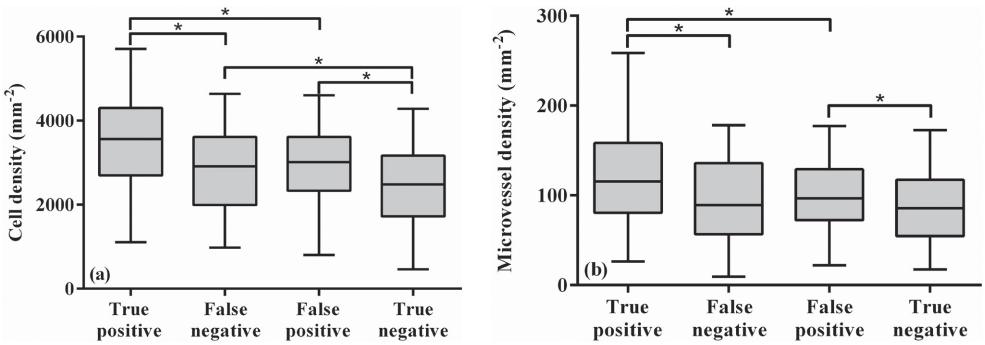

Figure 3. Cell density (a) and microvessel density (b) for MR-detected (true positives) and non-detected tumour (false negatives) voxels and for peripheral zone tissue assigned as tumour (false positives) and non-tumour (true negatives) based on MR images. Significant differences ($p < 0.0001$) are marked with an '*'.

with a high CD and MVD and has a GS of 3+4 (mean CD: 5437 cells/mm^2, mean MVD: 241 vessels/mm^2), whereas the CD and MVD in the right tumour are low with GS 3+3 (mean CD: 2657 cells/mm^2, mean MVD: 99 vessels/mm^2).

Similar results were found in all patients. The MR detected tumour voxels (true positives) had on average the highest CD, followed by the MR non-detected tumour voxels (false negatives) (median CD true positive: 3560 cells/mm^2, MR false negative: 2910 cells/mm^2, median MVD true positive: 115 vessels/mm^2, false negative: 90 vessels/mm^2) (Figures 3a and 3b). These values were compared with CDs and MVDs in non-tumour PZ voxels that were either incorrectly assigned by the model as tumour voxel (false positives) or correctly as non-tumour (true negatives). CDs and MVDs in the false-positives and true-negatives groups were 3015 cells/mm^2, 95 vessels/mm^2 and 2480 cells/mm^2, 85 vessels/mm^2, respectively. These differences in CD and MVD were all significant ($p < 0.0001$), except for the differences between the false-negative and false-positive voxels (CD: $p = 0.198$, MVD: $p = 0.234$). Also, false-negative tumour tissue had similar MVD as the MVD found in the non-tumour PZ ($p = 0.233$).

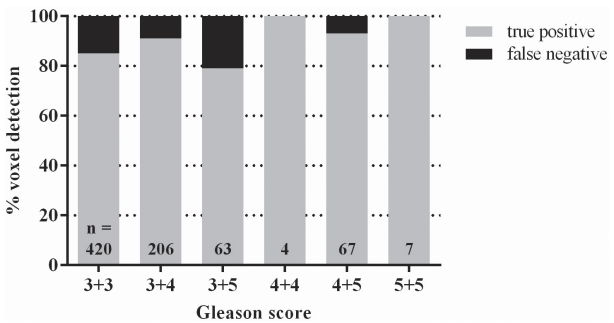

Figure 4. Percentage of true-positive and false-negative tumour voxels for the different Gleason scores. We found a trend that the tumour voxels with higher Gleason score (GS ≥ 3+4) score were easier to detect ($p = 0.06$). N, total amount of voxels per Gleason score.

In Figure 4, the percentages of true-positive and false-negative tumour voxels are plotted for the different GSs. We found a trend that the tumour voxels with higher GS were easier to detect ($p = 0.06$). This is in line with the finding that tumour tissue with a GS $\geq$ 3+4 showed a higher CD and MVD compared to tumour tissue with a GS of 3+3 ($p < 0.0001$).

Discussion

Precise prostate tumour detection, and therefore tumour delineation, is complicated by the large spread in ADC and K^{trans} values inside the tumour. In a previous study, we presented a logistic regression model with a high diagnostic performance (AUC=0.89) for detection of tumour voxels in the prostate PZ.[8] The output of this model can be used for tumour delineation. However, parts of tumours were non-detected by the model. Similarly, parts of non-tumour PZ tissue were incorrectly assigned as tumour tissue. As the model was generated based on clinical data, it can be inferred that prostate tumours frequently are delineated incompletely or that normal tissue is included in tumour areas. This will have implications for the outcome of focal boosting strategies and of focal therapy, which is an upcoming and promising treatment strategy.

In the present study, we searched for a histological explanation of the difficulty to detect all tumour voxels. We showed a significant difference in CD and MVD between detected (true positives) and non-detected tumour parts (false negatives). False-negative tumour voxels contain on average a lower density of cells and microvessels (Figure 3a and 3b). Interestingly, the false-negative tumour voxels show CDs which are similar to the values found in the false positives. Furthermore, MVDs in false-negative tumour voxels are similar to the MVDs found in non-tumour PZ tissue. This strongly indicates that the limitations in sensitivity and specificity of tumour voxel detection with MRI are caused by the underlying histology. MRI-based tumour prediction models might therefore reflect underlying histological characteristics like cell density and microvessel density, rather than predicting tumour presence.[20] Although this may be seen as a disadvantage, when it comes to radiotherapy, this reflection of histological characteristics may be beneficial. In contrast to all-or-nothing therapies like surgery, in radiotherapy it is possible to sculpt the radiation dose based on underlying tissue characteristics to obtain optimal tumour control probability.[21] A model reflecting histological properties may therefore be a valuable input for such an approach.

For translation of histological variables into prescription of radiation dose, one could argue from a radiobiological point of view, that tumour regions with a higher CD require higher radiation dose levels.[22] The relation between MVD and required dose is, however, more complicated. In many cancers, high vascularity has been associated with tumour growth and metastases. In prostate cancer, this relationship is controversial. Schlemmer et al. reported in a study including 28 patients, no correlation between MVD and GS and other clinical variables.[10] On the other hand, in a study by Mucci et al. including 572 patients, high-grade prostate tumours

showed significantly larger MVD than low-grade tumours.[23] This is consistent with what we found in the current study. Future studies are necessary to investigate the relation between imaging parameters and histological variables on one side and required dose levels on the other side.
We found a trend that tumour voxels with higher GS were easier to detect. This suggests that the most aggressive tumour parts are the most easy to detect. In addition, of voxels with GS 3+3, 85% was detected in this study. This is a high value compared with other studies.[12] It can be speculated that the histology of the detected GS 3+3 voxels is slightly different from the non-detected voxels. However, the number of patients in this study is too small to draw definitive conclusions on this.
In this study, detailed histological properties are related to MR parameter maps on voxel level. Such high resolution information about the relation between MR imaging and histology is important for precise target definition for focal boosting and focal therapy. Previous studies have shown relationships between histology and MR parameter maps. Regions with a higher CD are correlated with low ADC and high K^{trans} values.[9,24] Tumour CD was related to detectability based on ADC images.[12] Qualitative parameters retrieved from the analysis of DCE-MRI signal-enhancement curves have been related with microvasculature of prostate tumour tissue.[10,11] However, most of these studies were performed on a regional or tumour level and did not provide the detailed information which is required for focal treatment. Therefore, focus in this study was on the voxel level. In addition, most studies did not investigate the non-tumour PZ tissue in a detailed fashion. We showed that non-tumour PZ tissue is highly heterogeneous on CD and MVD. This may be partly caused by prostate intraepithelial neoplasia and prostatitis, but even healthy PZ tissue is highly heterogeneous on these characteristics.
This study shows that tumour voxels with a CD below 3000 cells/mm^2 and a MVD less than 90 vessels/mm^2 are harder to detect. Given the high similarity in CD and MVD between tumour and healthy tissue (Figure 3a and 3b), it seems unlikely that all tumour voxels can be detected using the imaging techniques DWI and DCE-MRI, unless large volumes of non-tumour tissue are included. This is, of course, not endeavored by focal boosting strategies or focal therapy. As tumour detection is still not perfect, focal boosting might be preferred above focal therapy, as with focal boosting the remaining prostate tissue receives normal dose levels. Local recurrences will be reduced, toxicity, however, will stay at same levels.
This study has some limitations. First of all, the number of patients is small. The explorative nature of this work should be kept in mind for the interpretation of the results. Due to the small registration error, we were able to relate histopathological information with MR images in a highly detailed fashion. This high-resolution comparison resulted in a high number of voxels included in this study. However, one should keep in mind that all these voxels are not completely independent. Moreover, K^{trans} values were normalised to the median values in the PZ. This method is feasible, unless >50% of the PZ is comprised of tumour. In the future, improved quantification of DCE-MRI might allow the use of absolute K^{trans} values.[18] Unfortunately, the phase images needed for this quantification method, were not available in this patient

cohort. Furthermore, this study focused only on the PZ of the prostate. This has several reasons. First, the number of transition and central zone tumours in our patient group was limited (n = 1). Second, the interpretation of MR imaging is a lot more complicated in these parts of the prostate, due to the presence of benign prostatic hyperplasia. Additionally, histological data was retrieved from patients of the same cohort as used for the initial validation of the model. To extent the applicability of the model to other institutes, the model accuracy is being validated in an independent patient cohort. Finally, in this study, we compared model outcome with the tissue characteristics CD and MVD. However, these tissue characteristics do not fully explain the large spread in the ADC and K^{trans} data. An explanation for this might be the limited measurement precision of ADC and K^{trans}. Moreover, future research should focus on what tissue characteristics explain ADC and K^{trans} values inside tumour tissue best. The ADC, for instance, might be influenced by other factors like extracellular and intracellular space and volume, as well as membrane permeability.[25]

In conclusion, we found large heterogeneity inside prostate tumours and non-tumour PZ tissue on histological level. This heterogeneity is reflected by the MR images. CDs and MVDs of false-negative tumour voxels resembled those found in non-tumour PZ tissue. This illustrates that the limitations in tumour voxel detection with MRI are related to histological characteristics. In addition, detected tumour voxels had high CDs and MVDs and voxels with higher GS showed a trend towards easier detection. As stated before, high CDs require higher radiation doses to sterilise a tumour and high MVDs may be related to tumour aggressiveness. Therefore, it could be speculated that the tumour parts requiring the highest radiation dose are detected with MRI and can be treated using focal therapy or focal boosting.

References

1. Cellini N, Morganti AG, Mattiucci GC, et al. Analysis of intraprostatic failures in patients treated with hormonal therapy and radiotherapy: implications for conformal therapy planning. Int J Radiat Oncol Biol Phys 2002;53:595-9.
2. Pickett B, Vigneault E, Kurhanewicz J, Verhey L, Roach M. Static field intensity modulation to treat a dominant intra-prostatic lesion to 90 Gy compared to seven field 3-dimensional radiotherapy. Int J Radiat Oncol Biol Phys 1999;44:921-9.
3. Singh AK, Guion P, Sears-Crouse N, et al. Simultaneous integrated boost of biopsy proven, MRI defined dominant intra-prostatic lesions to 95 Gray with IMRT: early results of a phase I NCI study. Radiat Oncol 2007;2:36.
4. Ahmed HU, Hindley RG, Dickinson L, et al. Focal therapy for localised unifocal and multifocal prostate cancer: a prospective development study. Lancet Oncol 2012;13:622-32.
5. Futterer JJ, Heijmink SW, Scheenen TW, et al. Prostate cancer localization with dynamic contrast-enhanced MR imaging and proton MR spectroscopic imaging. Radiology 2006;241:449-58.
6. Hosseinzadeh K, Schwarz SD. Endorectal diffusion-weighted imaging in prostate cancer to differentiate malignant and benign peripheral zone tissue. J Magn Reson Imaging 2004;20:654-61.
7. Groenendaal G, van den Berg CA, Korporaal JG, et al. Simultaneous MRI diffusion and perfusion imaging for tumor delineation in prostate cancer patients. Radiother Oncol 2010;95:185-90.
8. Groenendaal G, Borren A, Moman MR, et al. Pathologic validation of a model based on diffusion-weighted imaging and dynamic contrast-enhanced magnetic resonance imaging for tumor delineation in the prostate peripheral zone. Int J Radiat Oncol Biol Phys 2012;82:e537-44.
9. Xu J, Humphrey PA, Kibel AS, et al. Magnetic resonance diffusion characteristics of histologically defined prostate cancer in humans. Magn Reson Med 2009;61:842-50.
10. Schlemmer HP, Merkle J, Grobholz R, et al. Can pre-operative contrast-enhanced dynamic MR imaging for prostate cancer predict microvessel density in prostatectomy specimens? Eur Radiol 2004;14:309-17.
11. Oto A, Yang C, Kayhan A, et al. Diffusion-weighted and dynamic contrast-enhanced MRI of prostate cancer: correlation of quantitative MR parameters with Gleason score and tumor angiogenesis. AJR Am J Roentgenol 2011;197:1382-90.
12. Langer DL, van der Kwast TH, Evans AJ, et al. Intermixed normal tissue within prostate cancer: effect on MR imaging measurements of apparent diffusion coefficient and T2--sparse versus dense cancers. Radiology 2008;249:900-8.
13. Groenendaal G, Moman MR, Korporaal JG, et al. Validation of functional imaging with pathology for tumor delineation in the prostate. Radiother Oncol 2010;94:145-50.
14. Schabel MC, Parker DL. Uncertainty and bias in contrast concentration measurements using spoiled gradient echo pulse sequences. Phys Med Biol 2008;53:2345-73.
15. de Bazelaire C, Rofsky NM, Duhamel G, et al. Combined T2* and T1 measurements for improved perfusion and permeability studies in high field using dynamic contrast enhancement. Eur Radiol 2006;16:2083-91.
16. Cheng HL, Wright GA. Rapid high-resolution T(1) mapping by variable flip angles: accurate and precise measurements in the presence of radiofrequency field inhomogeneity. Magn Reson Med 2006;55:566-74.

17. Roberts C, Little R, Watson Y, Zhao S, Buckley DL, Parker GJ. The effect of blood inflow and B(1)-field inhomogeneity on measurement of the arterial input function in axial 3D spoiled gradient echo dynamic contrast-enhanced MRI. Magn Reson Med 2011;65:108-19.

18. Korporaal JG, van den Berg CA, van Osch MJ, Groenendaal G, van Vulpen M, van der Heide UA. Phase-based arterial input function measurements in the femoral arteries for quantification of dynamic contrast-enhanced (DCE) MRI and comparison with DCE-CT. Magn Reson Med 2011;66:1267-74.

19. Turkbey B, Pinto PA, Mani H, et al. Prostate cancer: value of multiparametric MR imaging at 3 T for detection--histopathologic correlation. Radiology 2010;255:89-99.

20. Rosenkrantz AB, Mendrinos S, Babb JS, Taneja SS. Prostate cancer foci detected on multiparametric magnetic resonance imaging are histologically distinct from those not detected. J Urol 2012;187:2032-8.

21. Bentzen SM. Theragnostic imaging for radiation oncology: dose-painting by numbers. Lancet Oncol 2005;6:112-7.

22. Webb S, Nahum AE. A model for calculating tumour control probability in radiotherapy including the effects of inhomogeneous distributions of dose and clonogenic cell density. Phys Med Biol 1993;38:653-66.

23. Mucci LA, Powolny A, Giovannucci E, et al. Prospective study of prostate tumor angiogenesis and cancer-specific mortality in the health professionals follow-up study. J Clin Oncol 2009;27:5627-33.

24. Langer DL, van der Kwast TH, Evans AJ, et al. Prostate tissue composition and MR measurements: investigating the relationships between ADC, T2, K(trans), v(e), and corresponding histologic features. Radiology 2010;255:485-94.

25. Anderson AW, Zhong J, Petroff OA, et al. Effects of osmotically driven cell volume changes on diffusion-weighted imaging of the rat optic nerve. Magn Reson Med 1996;35:162-7.

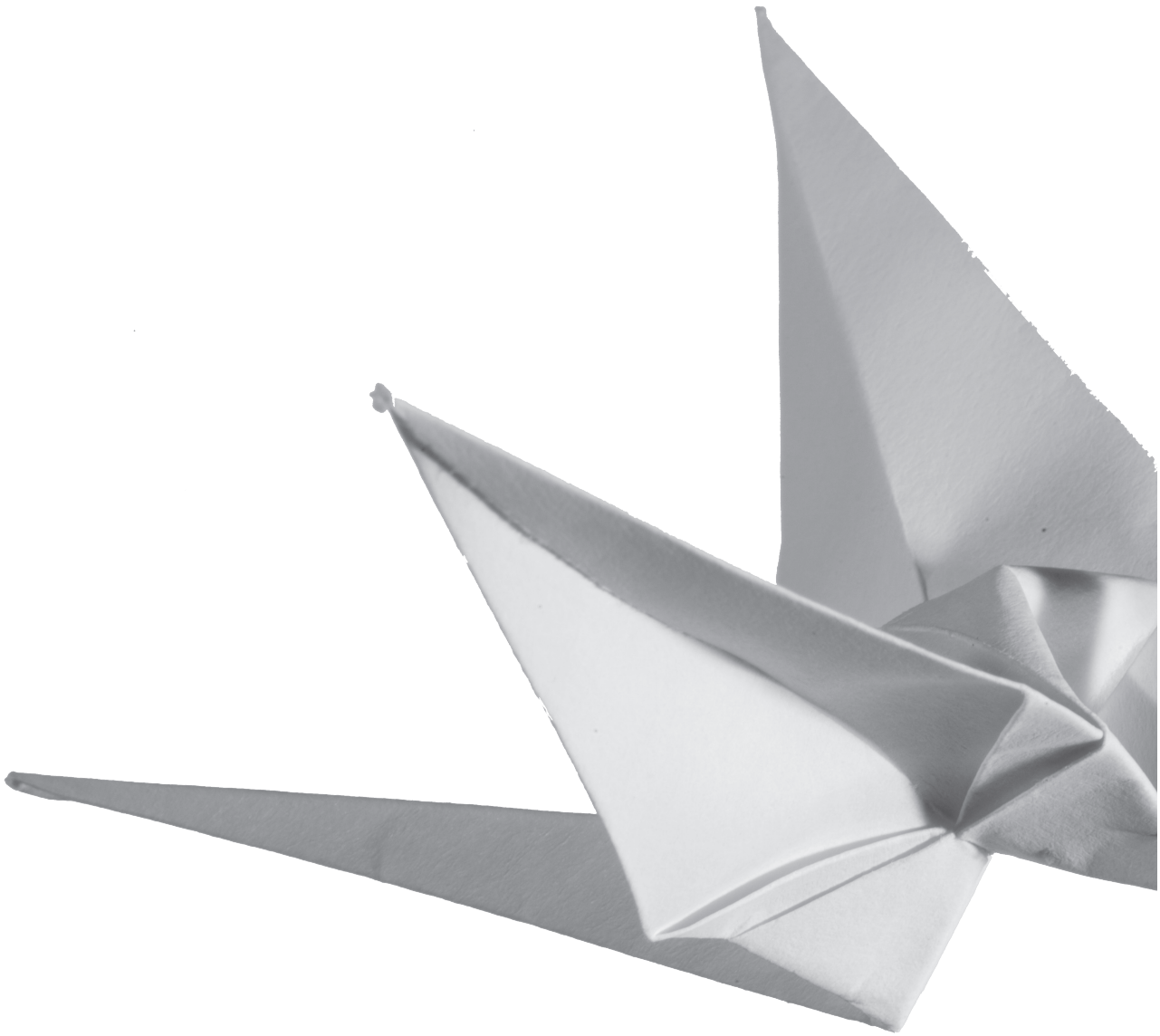

4

Why prostate tumour delineation based on apparent diffusion coefficient is challenging: An exploration of the tissue microanatomy

A. Borren,
M.R. Moman,
G. Groenendaal,
A.E. Boeken Kruger,
P.J. van Diest,
P. van der Groep,
U.A. van der Heide,
M. van Vulpen,
M.E.P. Philippens.

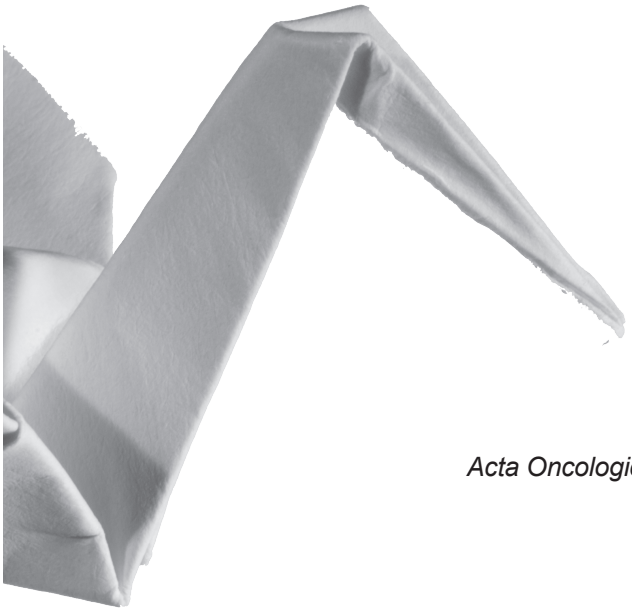

Acta Oncologica. 2013;52:1629-1636

Abstract

Background

Focal boosting of prostate tumours to improve outcome, requires accurate tumour delineation. For this, the apparent diffusion coefficient (ADC) derived from diffusion-weighted MR imaging (DWI) seems a useful tool. On voxel level, the relationship between ADC and histological presence of tumour is, however, ambiguous. Therefore, in this study the relationship between ADC and histological variables was investigated on voxel level to understand the strengths and limitations of DWI for prostate tumour delineation.

Materials and Methods

Twelve radical prostatectomy patients underwent a pre-operative 3.0T DWI exam and the ADC was calculated. From whole-mount histological sections cell density and glandular area were retrieved for every voxel. The distribution of all variables was described for tumour, peripheral zone (PZ) and central gland (CG) on regional and voxel level. Correlations between variables and differences between regions were calculated.

Results

Large heterogeneity of ADC on voxel level was observed within tumours, between tumours and between patients. This heterogeneity was reflected by the distribution of cell density and glandular area. On regional level, tumour was different from PZ having higher cell density ($p = 0.007$), less glandular area ($p = 0.017$) and lower ADCs ($p = 0.017$). ADC was correlated with glandular area ($r = 0.402$) and tumour volume ($r = -0.608$), but not with Gleason score. ADC tended to decrease with increasing cell density ($r = -0.327$, $p = 0.073$). On voxel level, correlations between ADC and histological variables varied among patients, for cell density ranging from $r = -0.439$ to $r = 0.261$ and for glandular area from $r = 0.593$ to $r = 0.207$.

Conclusions

The variation in ADC can to a certain extent be explained by the variation in cell density and glandular area. The ADC is highly heterogeneous, which reflects the heterogeneity of malignant and benign prostate tissue. This heterogeneity might however obscure small tumours or parts of tumours. Therefore, DWI has to be used in the context of multiparametric MRI.

Introduction

Dose escalation has proven to benefit treatment outcome in patients with prostate cancer.[1,2] However, increasing the dose to the entire prostate gland comes with the cost of more toxicity to organs at risk such as the rectum and bladder. As local recurrences frequently originate at the site of the macroscopic tumour, focal boost of the tumour area alone might improve tumour control.[3,4] Recently, a randomised phase III trial was started to investigate the benefit of focal lesion ablative microboost (FLAME trial).[5]

An essential element of focal boosting is the accurate delineation of the tumour area. It has been widely established that magnetic resonance imaging (MRI) is the modality of choice to localise prostate tumours.[6,7] The diagnostic performance of MRI for prostate cancer detection has been shown to improve by the addition of diffusion-weighted imaging (DWI) and Dynamic Contrast-enhanced MRI (DCE-MRI) to conventional T2 weighted MRI.[8-10] In a radiotherapy setting, however, target localisation puts higher demands on tumour detection accuracy. Every single voxel needs to be assigned to tumour or to normal prostate tissue to delineate the focal boost area accurately. DWI is a powerful tool to identify highly cellular tissue, like tumour.[11,12] For absolute quantification, the apparent diffusion coefficient (ADC) is derived. In prostate, the ADC is thought to be determined by both the amount of free water in the glandular ducts and the water diffusion restriction in the cellular tissue. Although several authors showed a relationship between ADC and cellularity on regional level, the reported correlation coefficients were merely weak to moderate.[11-14] On voxel level, the relationship between ADC and histological presence of tumour is, however, even more ambiguous. Therefore, thresholding the ADC is inadequate for tumour delineation.[15] To understand the limitations of DWI for tumour delineation, detailed analysis on voxel level is required to reveal the strong and weak points of DWI.

In the present study, we performed a detailed comparison between prostate histology and ADC maps, based on a robust and accurate MRI-pathology registration method. The distribution of ADC and histological variables cell density and relative glandular area was described on a voxel level. This was done for tumour areas, as well as for the normal tissues in peripheral zone (PZ) and central gland (CG).

Aim of this study was to reveal the relationship between ADC and histological variables on voxel level to understand the strengths and the limitations of DWI for prostate tumour delineation.

Materials and Methods

Patients

The study was approved by the institutional review board and informed consent was obtained from all patients. Twelve patients were enrolled in the study. All patients had biopsy proven prostate cancer and were scheduled for a Robotic Assisted Laparoscopic Prostatectomy (RALP). Before radical prostatectomy, patients underwent a 3T MRI exam including a T2w sequence and DWI. For registration purposes afterwards, a urinary catheter was inserted before the MRI exam.

Peristalsis was not suppressed. To prevent prostate deformations, no endorectal coil was used. Two patients were excluded from analysis, because of large deformations of the diffusion-weighted images in one patient and because of considerable motion during image acquisition in the second patient. In one other patient, artefacts distorted a small part of the ADC map. This part was excluded from analysis and contained all the healthy PZ voxels. Tumour regions in the PZ of this patient were not affected. Ten patients were eligible for analysis (Table 1).

MR imaging

MRI exams were performed on a 3T Philips Achieva MR scanner (Philips, Best, The Netherlands). T2w images were acquired with a fast spin-echo sequence, TR/TE = 8396/120 ms, echo train length 13, acquisition matrix 256×256, field of view (FOV) = 20 cm, slice thickness 3 mm, inter-section gap 1 mm.

DWI scans were performed using a multislice single shot spin-echo echo-planar imaging (EPI) sequence (FOV = 380×320 mm^2, acquisition matrix = 152×89, acquisition resolution = 2.5×3.5 mm^2, slice thickness = 3 mm, number of slices = 60, intersection gap = 0 mm, TR/TE = 5000/54 ms, EPI-factor = 47, 3 averages, SENSE factor = 2, b-values 0, 300, 500 and 1000 s/mm^2, in three orthogonal directions). ADC values were calculated after exclusion of the perfusion sensitive b = 0 data and resampled to an in-plane resolution of 2.5×2.5 mm^2.[16]

Histopathology

Immediately after prostatectomy, the left and right prostate surfaces were inked with different colours. The whole prostate was fixed in formaldehyde for approximately two days. Three carbon

Table 1. Patient characteristics

Characteristic		Value
Patient age (years)*		63 (48-74)
PSA level (ng/mL)*		13.9 (6.3-29)
Pathological tumour stage#	T2a	2
	T2c	3
	T3a	5
Tumour volume (cm^3)*		2.88 (0.58-9.36)
Gleason score per patient#	3+3=6	3
	3+4=7	4
	3+5=8	3
Gleason score per tumour	3+3=6	3
	3+4=7	5
	3+5=8	2
	4+5=9	2

*median and (range); #patient numbers

rods were inserted into the prostate to facilitate the registration process. Next, the prostate was cut into slices of 3 mm. Finally, whole-mount microscopic slices of 4 mm were cut from the paraffin embedded macroscopic slices and stained with haematoxylin-eosin (H&E). Tumour areas were delineated on the H&E sections by a pathologist. Each tumour region was assigned with a Gleason score in consensus by two observers. Digital photographs were taken of the macroscopic slices and the H&E stained sections including the delineations were digitised using a flatbed scanner (Epson Expression 10000XL).

MRI-pathology registration

MR images were registered to the H&E sections, as described by Groenendaal et al.[17] Three steps were performed: 1) registration of the H&E sections to the macroscopic slices; 2) reconstruction of the prostate specimen from the macroscopic slices; and 3) registration of the reconstructed prostate specimen to the T2w MR images. The protocol was optimised in the last five patients, where the prostate was first embedded in agarose gel to match for the sectioning plane of the prostate and the MRI plane. On average, the registration error in all patients was about 1 voxel (reconstructed voxel size 2.5×2.5×2.5 mm^3).[17]

Analysis of histological variables

Three microscopic slices per patient, containing the dominant tumour nodule and normal PZ and CG, were chosen for further analysis and digital whole slide images were created.[18] Analysis of the cell density and glandular area was performed in a grid of 2.5×2.5 mm^2, corresponding to the MRI voxels. The H&E sections were used for the determination of the cell density and glandular area. With the IHC Nuclear Algorithm v8 in ImageScope v10.0 (Aperio Technologies, Vista, CA, USA) the absolute number of cell nuclei per voxel was identified. Minimum detectable nuclear size was set at 20 mm^2. Glandular area was defined as space without tissue, which predominantly comprised the lumens of glandular structures. The Positive Pixel Count Algorithm v9 was used to identify the relative glandular area per voxel.

Regional analysis

Healthy PZ, CG and tumours were defined as regions of interest (ROI) in each prostate. To account for the registration error and to prevent partial volume effects, a margin of approximately one voxel in the transverse plane was removed from the PZ and CG ROIs. As most tumour regions were too small to apply a margin, we did not apply a margin to tumour regions. Since partial volume effects and registration errors have a large influence on small tumours, we excluded tumour regions with a volume <0.22 cm^3 (diameter < three voxels = 7.5 mm). To investigate the correlation with Gleason score, regions within a tumour with a different Gleason score were separated into different ROIs.

Statistical analysis

On regional level, median ADC, cell density and glandular area were calculated for each ROI. Differences in median ADC and histological variables between PZ, CG and tumour were calculated with the paired Wilcoxon signed rank test (SPSS version 16.0, SPSS, Chicago, IL, USA). The Bonferroni correction was used to correct for multiple testing, P-values ≤0.025 were considered significant.

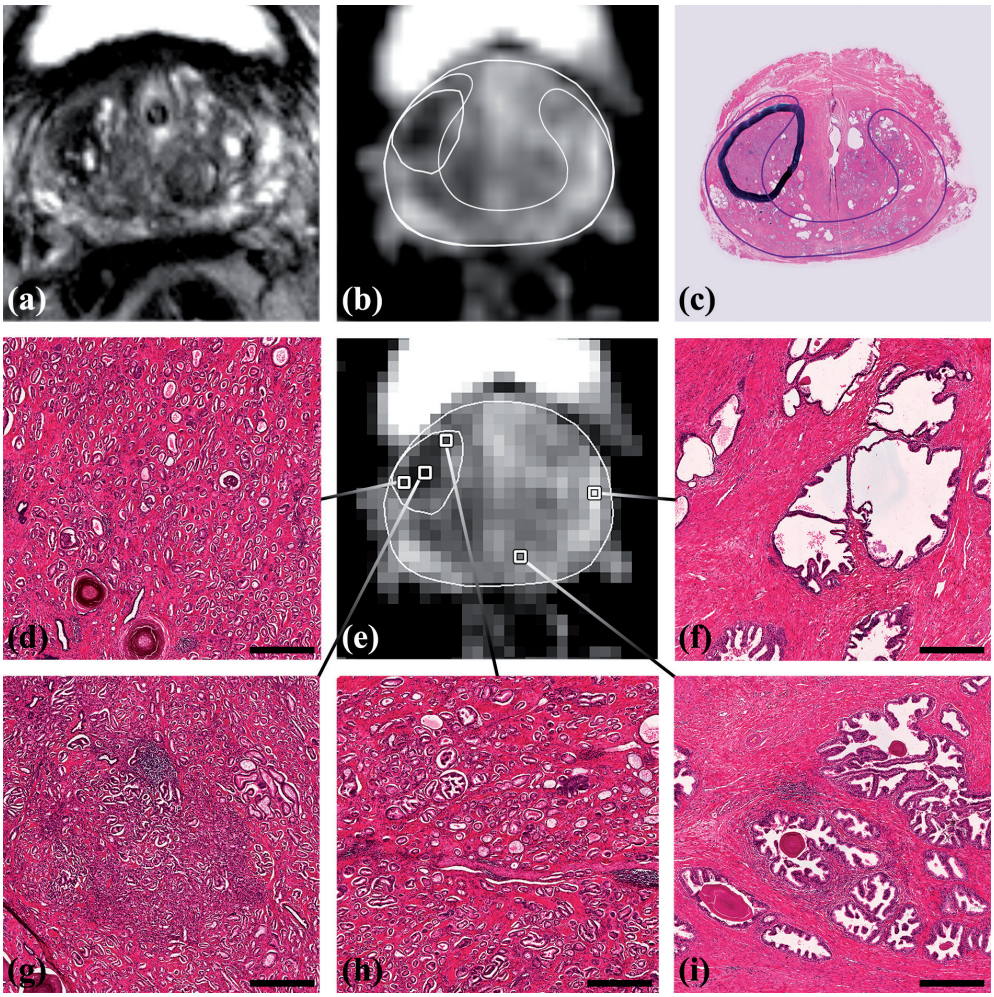

Figure 1. Patient example, showing voxels with an ADC ranging from 0.781 to 1.83 x 10^{-3} mm^2/s and the corresponding microanatomy. (a) T2w image. (b) high resolution ADC map with delineation of tumour and peripheral zone. (c) corresponding H&E section with delineations of a tumour with Gleason score 3+4 = 7 and the peripheral zone (thin line). On the low resolution ADC map in (e) several voxels are selected of which the corresponding microanatomy is shown in (d) and (f-i). (d) and (h) tumour voxels with Gleason grade 3. (g) tumour voxel with Gleason grade 4. (f) and (i) voxels with normal peripheral zone tissue. Benign voxels have apparent lower cell density and more glandular area. Scale bars: 200 µm.

Spearman's correlation coefficients were calculated between the median ADC and histological variables. In addition, a voxel-wise correlation analysis of ADC and histological variables was performed for every single patient. P-values ≤0.05 were considered significant.

Results

In total, 31 ROIs were available for analysis: 12 tumour, nine PZ and 10 CG ROIs. Two patients had a second tumour with a volume >0.22 cm^3 in addition to the dominant tumour. Eleven tumour regions were located in the PZ and one tumour region was found in the CG.

The detailed information available in this study is exemplified by two patients. The first example shows a hypointense region on T2w MRI with low ADC values, clearly corresponding to the delineated tumour on the H&E section (Figure 1). Tumour voxels are highly conspicuous in histology even at low magnification and present with high cell density and small glandular area compared to normal tissue. The variation in histological appearance among the selected voxels is reflected by the variation in ADC values. The voxel with the lowest ADC value (Figure 1g) corresponds to a Gleason grade 4 tumour voxel, whereas both other tumour voxels consist of Gleason grade 3 and contain less dense tumour tissue.

The second example illustrates the heterogeneity in histological appearance of voxels with a similar ADC (Figure 2). Although the dominant tumour in this patient is quite large, it is not easy to distinguish the tumour boundaries on the T2w MRI and ADC map. On the ADC map, several voxels are selected with an ADC of 1.2×10^{-3} mm^2/s. The corresponding histology shows that large differences in microanatomy could be present among voxels, despite a comparable ADC.

For all patients, a wide range in all variables was observed on three levels: 1) on voxel level within tumour and normal tissue ROIs, 2) among different tumours within patients (regional level) and 3) among patients (Table 2). This heterogeneity is visualised in Figure 3 for ADC and cell density in tumours and PZ.

Table 2. Regional histological characteristics and ADC

	GS 6 vs. GS ≥7		Normal PZ vs. tumour		Normal CG vs. tumour	
Variable	**Tumour***	p-value	**PZ***	p-value	**CG***	p-value
ADC (10^{-3} mm^2/s)	1.1 (0.7-1.3)		1.4 (1.0-1.6)	**0.017**	1.2 (1.0-1.4)	0.117
GS 6 regions	1.1 (0.7-1.4)	0.849				
GS ≥7 regions	1.1 (0.8-1.3)					
Cell density (mm^{-2})	4300 (3300-5700)		3100 (2500-4100)	**0.007**	3200 (2200-3600)	**0.002**
GS 6 regions	4000 (3300-5200)	0.239				
GS ≥7 regions	4400 (3300-6100)					
Glandular area	0.16 (0.09-0.26)		0.21 (0.11-0.35)	**0.017**	0.19 (0.09-0.38)	0.099
GS 6 regions	0.15 (0.09-0.27)	0.909				
GS ≥7 regions	0.18 (0.07-0.27)					

*data are medians with ranges. CG, central gland; GS, Gleason score; PZ, peripheral zone.
Bold values are significant values.

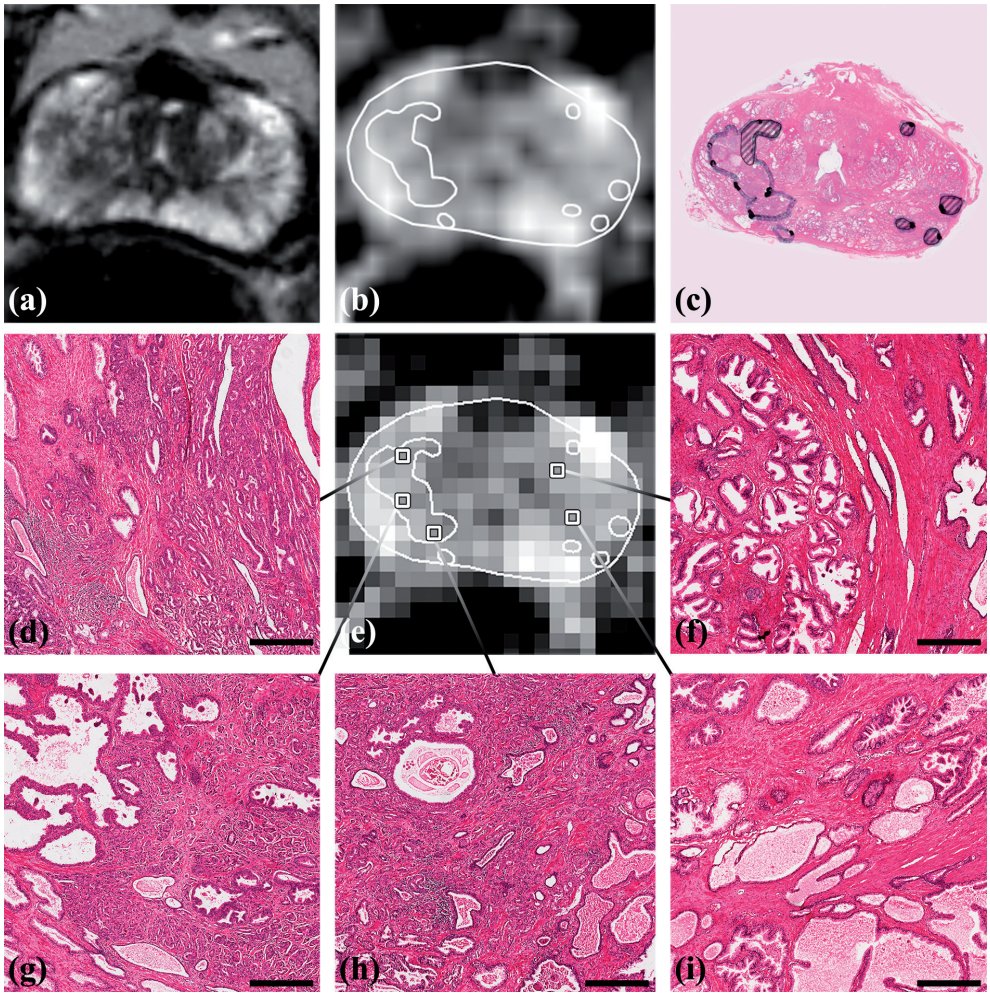

Figure 2. Patient example, showing the broad difference in histology among voxels with an ADC of 1.2 x 10^{-3} mm^2/s. (a) T2w image. (b) high resolution ADC map. (c) corresponding H&E section with delineated tumour. The dominant tumour had a Gleason score 4+5 = 9, striped tumour areas consisted of Gleason grade 3. (d), (g) and (h) tumour voxels. (f) central gland voxels containing benign prostatic hyperplasia. (i) voxel with normal peripheral zone tissue. Scale bars: 200 µm.

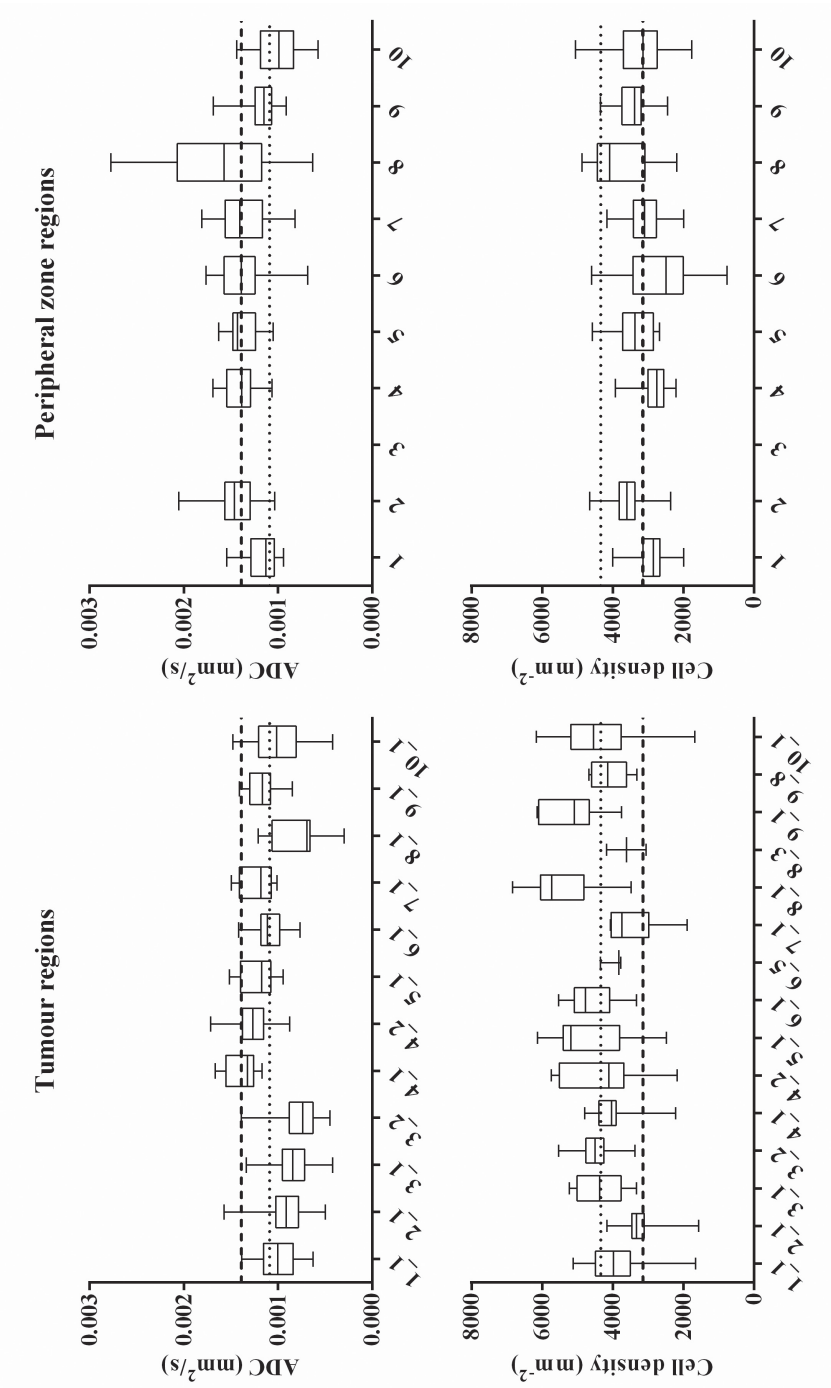

Figure 3. Boxplots of ADC and cell density for tumour and peripheral zone regions. Boxes are per patient with patient 3 and 4 having two separate tumour regions. Dotted line: median value of all tumour regions. Dashed line: median value of all peripheral zone regions.

Notwithstanding the large heterogeneity, significant differences in median values between tumour and normal tissue ROIs could be observed. In tumour regions, ADC and glandular area were lower and cell density was higher compared with PZ. Compared with CG, tumour regions had only significantly higher cell density (Table II). Tumour regions with Gleason score 6 (low-risk disease) and Gleason score ≥7 (intermediate/high-risk disease) were not different in ADC and histological variables. Large overlap between the different Gleason scores was present for all variables. Interestingly, in three of 12 very small tumours, excluded from analysis due to the small tumour volume (range 0.01–0.21 cm^3), areas with high Gleason grades were observed. In Figure 4, two examples are shown of small tumour islets with Gleason grade 4 and Gleason grade 5.

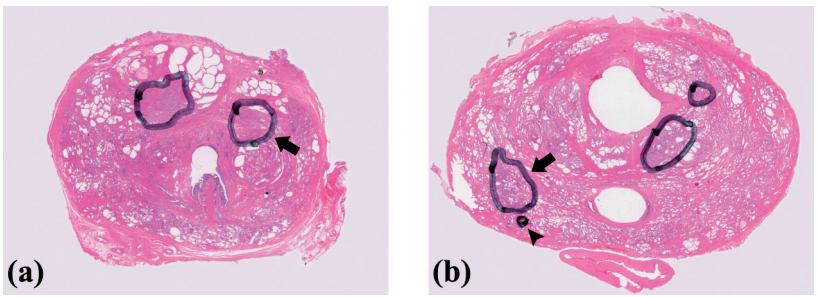

Figure 4. Example showing small tumour islets containing high Gleason grades. (a) arrow pointing at a tumour with a volume <0.22 cm^3 and Gleason score 3+4. (b) arrowhead pointing at a small tumour islet consisting of Gleason grade 5, located directly adjacent to a larger tumour with Gleason score 3+4. This shows that small tumour areas with high Gleason grades can be located outside the larger tumours.

On regional level, Spearman's correlations coefficients were calculated based on the median values of all ROIs. A weak correlation was observed between ADC and glandular area ($r = 0.402$, $p = 0.025$) and the ADC tended to be lower with increasing cell density, which, however, was not significant ($r = -0.327$, $p = 0.073$). No significant correlations were found between Gleason score and ADC and histological variables. Tumour volume was correlated with ADC ($r = -0.608$, $p = 0.036$) (Figure 5), but not with cell density and glandular area.
On voxel level, we determined correlations per patient, since the heterogeneity among patients could be large. Significant correlations between ADC and glandular area were found in five patients and ranged from $r = 0.593$ to $r = 0.207$ ($p < 0.000$ to $p = 0.008$). Significant correlations between ADC and cell density were found in six patients ranging from $r = -0.439$ to $r = 0.261$ ($p < 0.000$ to $p = 0.021$) (Figure 6). One patient showed even a positive correlation of cell density with ADC.

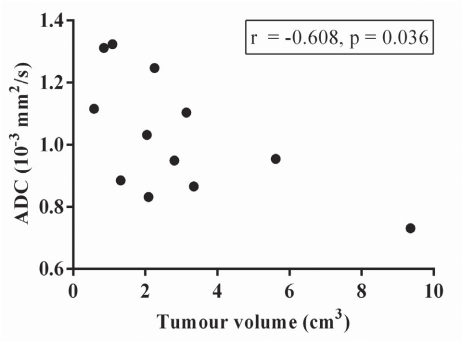

Figure 5. Scatterplot showing the correlation between tumour volume and ADC.

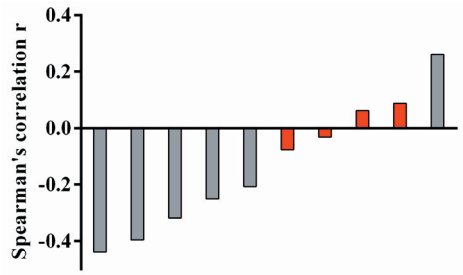

Figure 6. Voxel-wise correlation of ADC with cell density per patient. Red bars represent the non-significant correlations.

Discussion

In this study, we described and illustrated on a voxel level the distribution of ADC and the histological variables cell density and glandular area to understand the strengths and limitations of DWI for prostate tumour delineation. Large heterogeneity played a key role in the histological and diffusional characterisation of malignant and benign prostate tissue.

DWI with ADC maps, as part of multiparametric MRI, is a useful tool for prostate cancer diagnosis.[6,9] Although it is well known that a region with low ADC is suspicious for prostate cancer, ADC maps can be rather vague and the interpretation challenging. Small tumours and parts of tumours might be easily missed. To benefit most of focal boost, accurate tumour delineation including all tumour voxels, is required. As a consequence, there is need for a decision about malignancy on a voxel level. Therefore, we evaluated the variation in ADC and histological variables both on regional and voxel level.

In this study, we found significant differences between tumour and PZ regions. A difference in cell density between tumour and CG was observed, but not a difference in ADC. This might be explained by the high incidence of benign prostatic hyperplasia (BPH) in elderly men with its wide spread in ADC values.[19] In addition, on regional level a weak correlation between ADC and glandular area was observed. These results are consistent with published data. To our knowledge, four studies investigated the relationship of ADC with cell density of prostate tissue. Significant, but weak to moderate correlations were reported. The correlations in these studies were based upon average ADC values and cell density per tumour ROI. MRI data and histopathology were visually matched. Correlations of -0.5 between ADC and cell density were observed by Langer et al. and Zelhof et al.[12,13] A somewhat stronger correlation of -0.69 was found by Gibbs et al. and of -0.64 by Wang et al.[11,14] Together with the results of other investigators, our study showed that the strength of ADC maps is that they reflect the heterogeneity of prostate tissue. The variation in ADC can be explained to a certain extent by a variation in cell density and glandular area. Although a registration error will always have some influence on MRI-pathology correlation analyses, the hypothesis that ADC is determined by cell density might be too simple. Other factors like extracellular and intracellular space and volume as well as membrane permeability might be involved.[20] As more detailed information is needed for optimal tumour delineation, we investigated the distribution of ADC and histological characteristics in tumour, PZ and CG on voxel level. Tumour tissue, as well as normal tissue, showed large heterogeneity in ADC, cell density and glandular area. Overlap between malignant and benign regions was clearly present. Especially between smaller tumours large diversity in ADC was observed. In addition, we observed an inverse correlation between tumour volume and ADC. This might rather reflect partial volume effects than less restricted diffusion, as we did not find a correlation between tumour volume and histological characteristics. Nevertheless, this correlation, together with the heterogeneity of prostate tissue, means that some of the smaller tumours and parts of tumours might be missed on an ADC map. Correlation coefficients found on voxel level, varied a lot among patients. Although this might be partially explained by differences in registration accuracy among patients, we have illustrated that patient specific differences in prostate tissue composition are likely to play an additional important role. In addition, considerable variation in ADC values of normal PZ might be present among patients. In a study by Litjens et al. it was hypothesised that this variation might be the result of normal variations in prostate physiology.[21] The variation in ADC values we found in the present study, was comparable with the variation found in literature.[15] It is, however, hard to compare ADC values between different institutes, as ADC values are influenced by differences in the choice of b-values and other experimental variables.[22]

Further, we sought for a spatial correlation between ADC and Gleason score. Although in literature significant correlations are found, we could not demonstrate a difference in ADCs between tumours with Gleason score 6 (low-risk disease) and Gleason score 7 or higher (intermediate- and high-risk disease).[23,24] Neither was there a difference in cell density, nor in glandular area. The Gleason grading system is the most commonly used system to assess prostate cancer aggressiveness

and consequently a very important clinical and prognostic factor. This system however, is based on tissue architecture and therefore not directly related to cell density, glandular area or ADC. To our knowledge, no correlation of Gleason score with cell density has been reported yet, although we would expect cell density to be higher and glandular area to be sparser in areas with higher Gleason scores.

In our study, tumour regions with Gleason grade 4 or 5 were present in very small lesions (volume <0.22 cm^3), which are beyond the detection level of MRI. Until now, it has been hypothesised that these small lesions are of minor influence on outcome of the patient, because most recurrences originate at the site of the dominant primary tumour.[3,4,25] The clinical consequence of missing these small regions with high Gleason scores, might be resolved by the recently started randomised phase III trial investigating the benefit of a focal lesion ablative microboost (FLAME trial).[5]

This study has some limitations. Although we used a robust and accurate MRI-pathology registration method, this method was not perfect and a registration error of approximately one voxel was present. Furthermore, the number of patients was small.

Altogether, the strength of the ADC is that its heterogeneity reflects the heterogeneity of malignant and benign prostate tissue and that the variation in ADC to a certain extent can be explained by a variation in cell density and glandular area. However, small tumours and parts of tumours might be missed on an ADC map.

In conclusion, we histologically evaluated the strengths and the limitations of DWI for prostate tumour delineation. On voxel level, cell density and glandular area of malignant and benign regions were highly heterogeneous, which was reflected by the heterogeneity of ADC maps. This heterogeneity might however obscure small tumours or parts of tumours. Therefore, DWI has to be used in the context of multiparametric MRI.

References

1. Peeters ST, Heemsbergen WD, Koper PC, et al. Dose-response in radiotherapy for localized prostate cancer: results of the Dutch multicenter randomized phase III trial comparing 68 Gy of radiotherapy with 78 Gy. J Clin Oncol 2006;24:1990-6.
2. Zelefsky MJ, Pei X, Chou JF, et al. Dose escalation for prostate cancer radiotherapy: predictors of long-term biochemical tumor control and distant metastases-free survival outcomes. Eur Urol 2011;60:1133-9.
3. Cellini N, Morganti AG, Mattiucci GC, et al. Analysis of intraprostatic failures in patients treated with hormonal therapy and radiotherapy: implications for conformal therapy planning. Int J Radiat Oncol Biol Phys 2002;53:595-9.
4. Arrayeh E, Westphalen AC, Kurhanewicz J, et al. Does local recurrence of prostate cancer after radiation therapy occur at the site of primary tumor? Results of a longitudinal MRI and MRSI study. Int J Radiat Oncol Biol Phys 2012;82:e787-93.
5. Lips IM, van der Heide UA, Haustermans K, et al. Single blind randomized Phase III trial to investigate the benefit of a focal lesion ablative microboost in prostate cancer (FLAME-trial): study protocol for a randomized controlled trial. Trials 2011;12:255.
6. Groenendaal G, Borren A, Moman MR, et al. Pathologic validation of a model based on diffusion-weighted imaging and dynamic contrast-enhanced magnetic resonance imaging for tumor delineation in the prostate peripheral zone. Int J Radiat Oncol Biol Phys 2012;82:e537-44.
7. Turkbey B, Mani H, Shah V, et al. Multiparametric 3T prostate magnetic resonance imaging to detect cancer: histopathological correlation using prostatectomy specimens processed in customized magnetic resonance imaging based molds. J Urol 2011;186:1818-24.
8. Langer DL, van der Kwast TH, Evans AJ, Trachtenberg J, Wilson BC, Haider MA. Prostate cancer detection with multi-parametric MRI: logistic regression analysis of quantitative T2, diffusion-weighted imaging, and dynamic contrast-enhanced MRI. J Magn Reson Imaging 2009;30:327-34.
9. Haider MA, van der Kwast TH, Tanguay J, et al. Combined T2-weighted and diffusion-weighted MRI for localization of prostate cancer. AJR Am J Roentgenol 2007;189:323-8.
10. Futterer JJ, Heijmink SW, Scheenen TW, et al. Prostate cancer localization with dynamic contrast-enhanced MR imaging and proton MR spectroscopic imaging. Radiology 2006;241:449-58.
11. Gibbs P, Liney GP, Pickles MD, Zelhof B, Rodrigues G, Turnbull LW. Correlation of ADC and T2 measurements with cell density in prostate cancer at 3.0 Tesla. Invest Radiol 2009;44:572-6.
12. Langer DL, van der Kwast TH, Evans AJ, et al. Prostate tissue composition and MR measurements: investigating the relationships between ADC, T2, K(trans), v(e), and corresponding histologic features. Radiology 2010;255:485-94.
13. Zelhof B, Pickles M, Liney G, et al. Correlation of diffusion-weighted magnetic resonance data with cellularity in prostate cancer. BJU Int 2009;103:883-8.
14. Wang XZ, Wang B, Gao ZQ, et al. Diffusion-weighted imaging of prostate cancer: correlation between apparent diffusion coefficient values and tumor proliferation. J Magn Reson Imaging 2009;29:1360-6.
15. Groenendaal G, van den Berg CA, Korporaal JG, et al. Simultaneous MRI diffusion and perfusion imaging for tumor delineation in prostate cancer patients. Radiother Oncol 2010;95:185-90.

16. Padhani AR, Liu G, Koh DM, et al. Diffusion-weighted magnetic resonance imaging as a cancer biomarker: consensus and recommendations. Neoplasia 2009;11:102-25.

17. Groenendaal G, Moman MR, Korporaal JG, et al. Validation of functional imaging with pathology for tumor delineation in the prostate. Radiother Oncol 2010;94:145-50.

18. Huisman A, Looijen A, van den Brink SM, van Diest PJ. Creation of a fully digital pathology slide archive by high-volume tissue slide scanning. Hum Pathol 2010;41:751-7.

19. Noworolski SM, Vigneron DB, Chen AP, Kurhanewicz J. Dynamic contrast-enhanced MRI and MR diffusion imaging to distinguish between glandular and stromal prostatic tissues. Magn Reson Imaging 2008;26:1071-80.

20. Anderson AW, Zhong J, Petroff OA, et al. Effects of osmotically driven cell volume changes on diffusion-weighted imaging of the rat optic nerve. Magn Reson Med 1996;35:162-7.

21. Litjens GJ, Hambrock T, Hulsbergen-van de Kaa C, Barentsz JO, Huisman HJ. Interpatient variation in normal peripheral zone apparent diffusion coefficient: effect on the prediction of prostate cancer aggressiveness. Radiology 2012;265:260-6.

22. Norris DG, Niendorf T. Interpretation of DW-NMR data: dependence on experimental conditions. NMR Biomed 1995;8:280-8.

23. Hambrock T, Somford DM, Huisman HJ, et al. Relationship between Apparent Diffusion Coefficients at 3.0-T MR Imaging and Gleason Grade in Peripheral Zone Prostate Cancer. Radiology 2011;259:453-61.

24. Verma S, Rajesh A, Morales H, et al. Assessment of aggressiveness of prostate cancer: correlation of apparent diffusion coefficient with histologic grade after radical prostatectomy. AJR Am J Roentgenol 2011;196:374-81.

25. Pucar D, Hricak H, Shukla-Dave A, et al. Clinically significant prostate cancer local recurrence after radiation therapy occurs at the site of primary tumor: magnetic resonance imaging and step-section pathology evidence. Int J Radiat Oncol Biol Phys 2007;69:62-9.

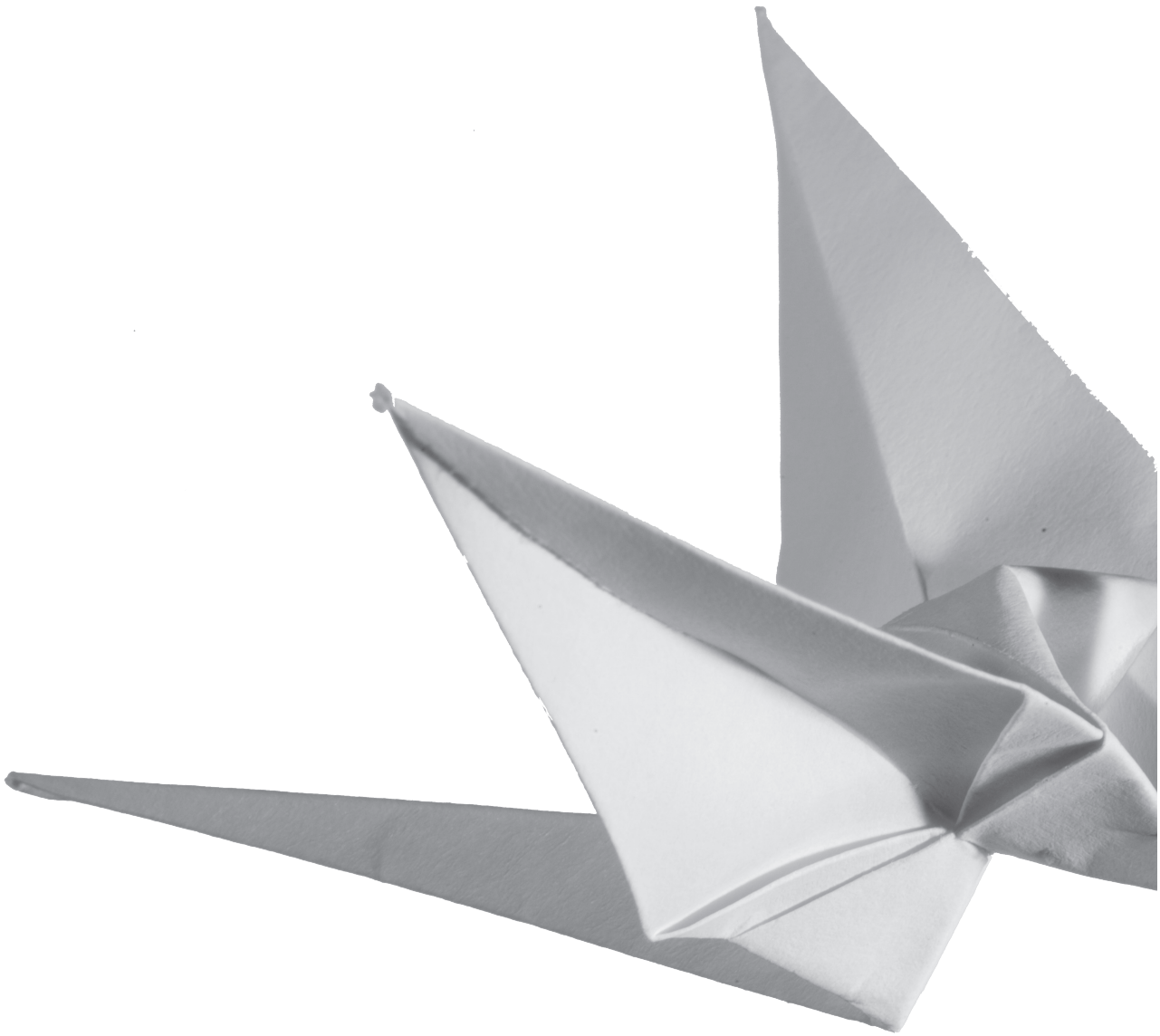

5

Detailed histological validation of dynamic contrast-enhanced MRI and diffusion weighted imaging: Challenge to differentiate prostate cancer from benign prostatic hyperplasia

A. Borren,
G. Groenendaal,
M.R. Moman,
A.E. Boeken Kruger,
P. J. van Diest,
P. van der Groep,
U.A. van der Heide,
M. van Vulpen,
M.E.P. Philippens.

Abstract

Background

Improving prostate cancer outcome with focal boosting requires accurate delineation of tumour areas. In the central gland of the prostate, precise tumour delineation is challenging, as on MRI the presence of tumour is mimicked by glandular (GH) and stromal (SH) benign prostatic hyperplasia (BPH). This resemblance might be explained by a variation in microanatomical characteristics such as cell density, microvessel density and glandular area. Therefore, in this study, the differences in microanatomical characteristics between tumour and BPH were investigated and compared with differences in MRI parameters, to understand the complexity in differentiating tumour from BPH.

Materials and Methods

Fifteen prostatectomy patients underwent a pre-operative multiparametric MRI at 3.0T, including dynamic contrast-enhanced (DCE) MRI and diffusion-weighted imaging (DWI). Whole-mount histological sections were evaluated for the presence of tumour, SH and GH, which were delineated as regions of interest (ROI). From the MR images, median values of K^{trans}, k_{ep} and apparent diffusion coefficient (ADC) were determined in tumour, SH and GH. In addition, from the whole-mount sections median cell density, glandular area and microvessel density were retrieved for all ROIs. Differences were calculated and correlations between variables assessed.

Results

Tumour regions showed low ADC, high K^{trans} and k_{ep} and high cell density and microvessel density. Large heterogeneity and considerable overlap with GH and SH was present. Nevertheless, tumour had highest microvessel density ($p \leq 0.018$) and higher cell density than GH ($p = 0.005$). Glandular area was higher in tumour compared to SH ($p = 0.018$). For the MRI parameters, k_{ep} showed a trend towards lower values in SH compared to GH and tumour ($p = 0.037$). K^{trans} was high in GH and SH, not different from tumour ($p > 0.074$). No difference in ADC was observed between tumour and GH and SH ($p > 0.093$).

Conclusions

Microanatomical differences are present between tumour and BPH, with microvessel density being the most pronounced. However, large heterogeneity and considerable overlap is present. This heterogeneity is reflected in the MRI parameters, limiting the differentiation between tumour and BPH. Nevertheless, the trend towards low k_{ep} in SH might help to distinguish this type of BPH from tumour.

Introduction

Local recurrences of prostate cancer are often seen at the primary tumour location.[1] As dose escalation has proven benefit, an additional radiation boost dose to this area might improve tumour control probability.[2,3] Focal boosting of tumour areas is therefore an emerging radiation technique to improve treatment outcome of prostate cancer patients.[4,5] In addition, treatment side effects can be reduced with targeted focal therapy to the index lesion only without treating the entire prostate gland.[6] Essential element of focal therapy is that all significant cancer is detected and treated. Both focal therapy and focal boosting therefore require precise delineation of the entire tumour area. Multiparametric magnetic resonance imaging (mp-MRI) has been established as the imaging modality of choice for the non-invasive localisation of prostate tumours.[7,8] The inclusion of functional techniques like dynamic contrast-enhanced MRI (DCE-MRI) and diffusion-weighted imaging (DWI) to T2w imaging, provides high diagnostic performance.[9,10]

To enable optimal usage of mp-MRI, detailed information about the radiological appearance of the various prostate tissue types and their underlying histological characteristics is needed. The peripheral zone (PZ) has already been investigated extensively. Correlations between MR imaging and tissue characteristics have been found and models for tumour detection have been developed.[11-13] Less has been published about the central parts of the prostate, although being the most challenging for tumour delineation. In aging men, prostate tissue might become very heterogeneous. Especially in the central gland (CG) it is challenging to distinguish tumour from benign changes, like benign prostatic hyperplasia (BPH), cystic changes and prostatitis.[10]

In the present study, we therefore investigated the histological and DCE-MRI and DWI characteristics of the CG. Neovascularisation in tumours frequently results in an increase in leaky and highly disorganised blood vessels, leading to alterations in tissue perfusion and the extravasation rate of contrast agent, which are measured with DCE-MRI. DWI is a powerful tool to identify highly cellular tissue, measuring the restricted motion of water molecules.[11,14] For absolute quantification, the apparent diffusion coefficient (ADC) is derived. Based on a robust MRI-pathology registration method, we performed a comparison of microvessel density, cell density, relative glandular area and MRI parameters between tumour areas and glandular and stromal subtypes of BPH.

Aim of this study was to investigate and compare the differences in microanatomical and MRI characteristics between tumour and BPH to understand the complexity in differentiating tumour from BPH.

Materials and Methods

Patients

The study was approved by the institutional review board and informed consent was obtained from all patients. Twenty patients were enrolled in the study. All patients had biopsy proven prostate cancer and were scheduled for a Robotic Assisted Laparoscopic Prostatectomy (RALP). Five patients were excluded from analysis, because of unavailability of pathologic material in two patients, considerable motion during MR image acquisition in one patient, and in two patients the

Table 1. Patient characteristics

Characteristic		Value
Patient age (years)*		63 (48-74)
PSA level (ng/mL)*		12 (5-29)
Pathological tumour stage#	T2a	2
	T2c	5
	T3a	8
Tumour volume (cm^3)*		1.44 (0.35-9.36)
Gleason score per patient#	3+3=6	6
	3+4=7	6
	3+5=8	3
Gleason score per tumour#	3+3=6	7
	3+4=7	10
	3+5=8	2
	4+5=9	2

*median and (range); #patient numbers

prostate specimen was severely deformed which hampered accurate registration. One patient was excluded from DWI-analysis only, because of motion distortion of the ADC maps. Clinical characteristics of the 15 eligible patients are shown in Table 1.

MR imaging

Multi-parametric imaging was performed on a 3T MRI-scanner (Philips Achieva Philips, Best, The Netherlands), including a T2w sequence, DCE-MRI and DWI. A 6-element phased array coil (sense cardiac) was used as receive coil. T2w images were acquired with a fast spin-echo sequence (field of view (FOV) = 20 cm, acquisition matrix 256×256, slice thickness 3 = mm, slice gap = 1 mm, TR/TE=8396/120ms, echo train length = 13).

The DCE-MRI protocol consisted of a 3D spoiled gradient echo sequence (FOV = 40 cm, acquisition matrix = 160×128×20, resolution 2.5×3.1×2.5 mm^3, TR/TE=4.0/1.7 ms, flip angle = 8°). Scans were repeated 120 times at 2.5s interval. A concentration of 0.1ml/kg of Gadobutrol (1.0M) (Gadovist, Schering AG, Berlin, Germany) contrast was injected with 2ml/s, followed by a saline flush. To quantify perfusion parameters, 3D absolute K^{trans} and k_{ep} parameter maps were caluclated using the general Tofts model as described previously.[15] This tracer kinetics model was chosen, as the fractional blood plasma volume (v_p) in the prostate is low, and thus v_p cannot be fitted accurately from the DCE-MRI data. A generic arterial input function (AIF) was used for all patients, because of measurement errors on the patient specific input functions. To account for patient specific differences in AIF, DCE-MRI parameters were normalised to the median value in normal

PZ for correlation analyses.[12] The DCE-MRI parameter maps were resampled to an in-plane resolution of 2.5×2.5 mm^2.
DWI scans were performed using a multislice single shot spin-echo echo-planar imaging (EPI) sequence (FOV=380×320 mm^2, acquisition matrix=152×89, slice thickness = 3 mm, number of slices 60, intersection gap = 0 mm, TR/TE=5000/54 ms, EPI-factor=47, 3 averages, SENSE factor =2, b-values 0, 300, 500 and 1000 s/mm^2 in three orthogonal directions). ADC values were calculated after exclusion of the perfusion sensitive b = 0 s/mm^2data and resampled to an in-plane resolution of 2.5×2.5 mm^2.

Histopathology

Immediately after prostatectomy, the left and right prostate surfaces were inked with different colours. The whole prostate was fixed in formaldehyde for approximately two days. Three carbon rods were inserted into the prostate to facilitate the registration process. Next, the prostate was cut into slices of 3 mm. Finally, whole-mount microscopic slices of 4 mm were cut from the paraffin embedded macroscopic slices and stained with haematoxylin-eosin (H&E). Tumour areas were delineated on the H&E sections by a pathologist. Each tumour region was assigned with a Gleason score in consensus by two observers. Digital photographs were taken of the macroscopic slices and the H&E stained sections including the delineations were digitised using a flatbed scanner (Epson Expression 10000XL).

MRI-pathology registration

MR images were registered to the H&E sections, as described previously.[15] Three steps were performed: 1) registration of the H&E sections to the macroscopic slices; 2) reconstruction of the prostate specimen from 3 mm-thick macroscopic slices; and 3) registration of the reconstructed prostate specimen to the T2w MR images. The protocol was optimised in the last ten patients, where the prostate was first embedded in agarose gel to match for the sectioning plane of the prostate and the MRI plane. On average, the registration error in all patients was about one voxel (reconstructed voxel size 2.5×2.5×2.5 mm^3).[12]

Immunohistochemistry

After deparaffination and rehydration, endogenous peroxidase activity was blocked and antigen retrieval performed. Slides were incubated for one hour at room temperature with a monoclonal primary antibody mouse-anti-human CD31, 1:50 (Leica Microsystems, Wetzlar, Germany). Subsequently, slides were incubated with poly-HRP-conjugated secondary antibody (Novolink Polymer Detection System, Leica Microsystems) and diaminobenzidine and counterstained with haematoxylin. Throughout, appropriate positive and negative controls were used.

Analysis of histological variables

Three whole-mount microscopic slices per patient, containing normal tissue, the index tumour and probable secondary tumours, were chosen for further analysis. H&E and CD31 stained slices were digitised at microscopic resolution and analysed in ImageScope v10.0 using a grid of 2.5×2.5 mm^2. Cell density (CD) was assessed with the IHC Nuclear Algorithm v8, relative glandular area (GA) with the Positive Pixel Count Algorithm v9 and the microvessel density (MVD) with the Microvessel Analysis Algorithm v1 (Aperio Technologies, Vista, CA). To account for aspecific background staining, the minimum detectable nuclear size was set at 20mm^2 and the minimum vessel area threshold was set at 50 mm^2. To compensate for variation in staining intensity, the settings of the algorithms were evaluated qualitatively and optimised for every batch by adjusting on test regions.

Regional analysis

Based on histopathology, normal PZ, CG and tumours were delineated in each prostate and defined as regions of interest (ROI). Hyperplastic nodules in the CG were identified and separated into stromal nodules (SH), consisting almost exclusively of stromal tissue, and glandular nodules (GH),

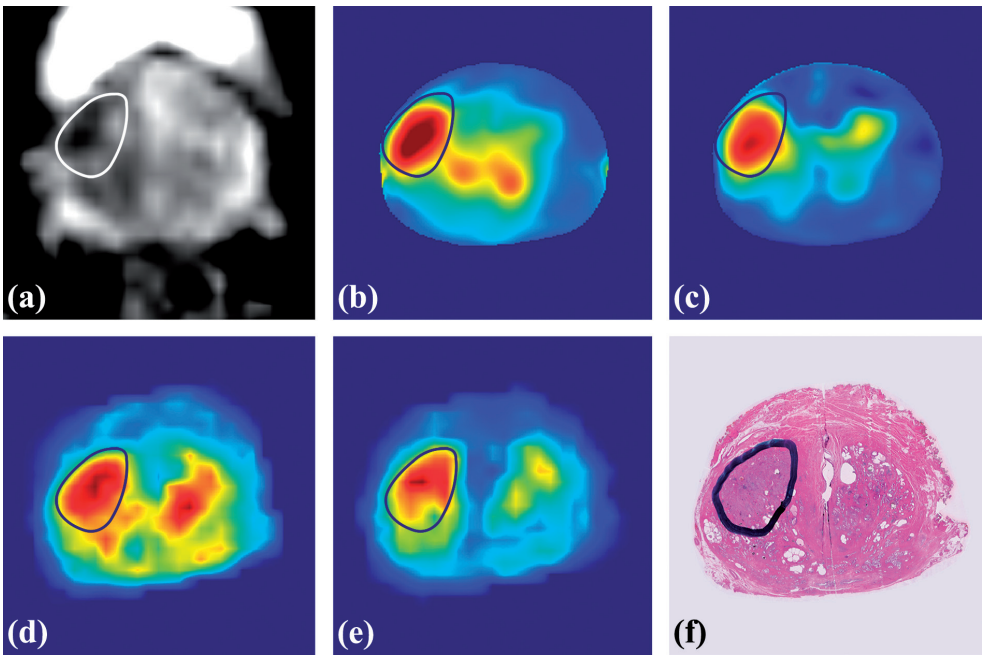

Figure 1. Patient example showing a well-defined tumour region originating in the peripheral zone and extending into the central gland. (a) ADC. (b) K^{trans}. (c) k_{ep}. (d) cell density. (e) microvessel density and (f) H&E section with tumour delineation.

comprising glandular as well as stromal tissue. The delineated ROIs were transferred to the K^{trans}, k_{ep} and ADC maps.
To account for the registration error and to prevent partial volume effects, a margin of approximately one voxel in the transverse plane was removed from the PZ and CG ROIs. Most other regions were too small to apply a margin. Since partial volume effects and registration errors have large influence on small tumours, it was decided to exclude tumour regions with a volume <0.22 cm^3 (diameter <3 voxels = 7.5 mm).

Statistical analysis

Median K^{trans}, k_{ep}, ADC, cell density, glandular area and microvessel density were calculated for each ROI and used for further analyses. Differences between ROIs were assessed pairwise with the Wilcoxon signed rank test (SPSS v20, SPSS, Chicago, IL). To calculate differences between tumour and hyperplastic nodules, only those patients were used for analysis in which GH or SH were determined. This subgroup was not statistically different from the total patient group. Differences between tumour regions with different Gleason scores were assessed with the Kruskal Wallis and Mann-Whitney U test. Spearman correlation coefficients were calculated using median values of tumour, CG and PZ ROIs. For these tests, normalised DCE-MRI parameters were used to account for interpatient variability. After Bonferroni correction, p-values ≤0.05/2 = 0.025 were considered significant.

Results

In the 15 patients, 15 PZ, 15 CG and 21 tumours ROIs were available for analysis, including a secondary tumour lesion with a volume >0.22 cm^3 in six patients. One tumour originated from the CG, the remainder originated from the PZ, but could extend into the CG (n = 6). In the CG, 10 GH and 7 SH ROIs were determined.
The characteristics of the different ROIs are illustrated in two figures. The first example shows a well-defined tumour region in the PZ, extending into the CG. High K^{trans} and k_{ep} and low ADC values characterise this tumour (Figure 1).
The second example shows a more caudal slice of the prostate of the same patient. Here, many small tumour areas are present, which cannot be easily distinguished. In the central gland, however, is an area present with low ADCs and high K^{trans} and k_{ep} values, clearly corresponding to a glandular BPH nodule (Figure 2).
Large heterogeneity was observed among patients for the microanatomical variables, as well as for MRI parameters. Considerable overlap between tumour and other regions of interest was present for every variable.
In comparison with PZ, tumour showed significantly higher CD, MVD, K^{trans} and k_{ep} and lower GA and ADC. However, the distinction between tumour and GH and SH was less clear (Table 2 and 3). For the MRI parameters, a trend was observed towards lower k_{ep} in SH compared with

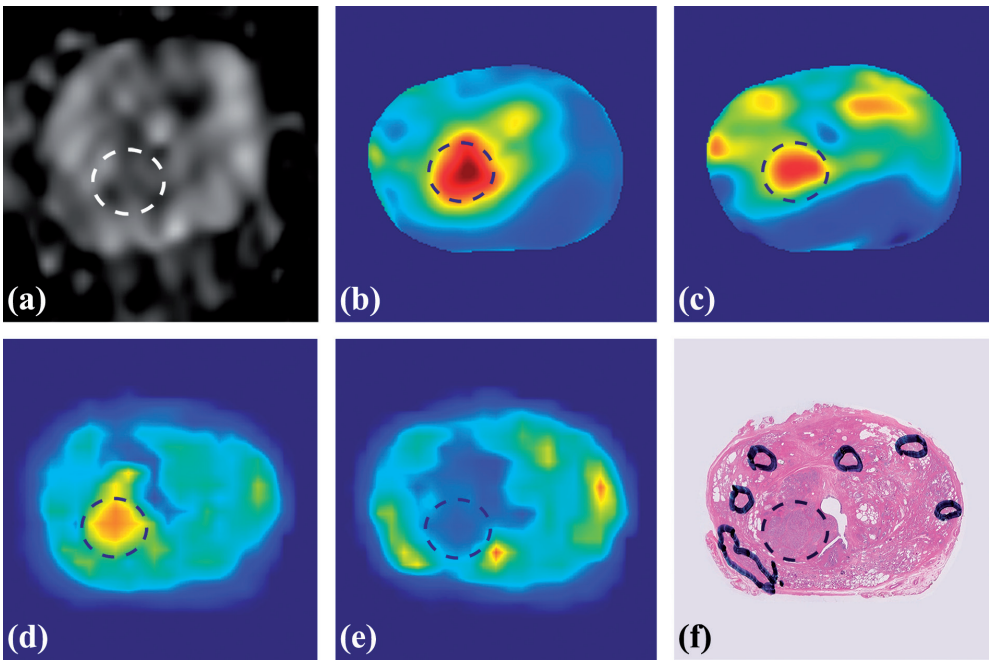

Figure 2. Patient example of glandular hyperplasia. (a) ADC. (b) K^{trans}. (c) k_{ep}. (d) cell density. (e) micro-vessel density and (f) H&E section with tumour delineation. Dashed circle: glandular hyperplastic nodule.

Table 2. MR imaging characteristics of tumour and normal tissue

	ADC*		**K^{trans}***		**k_{ep}***	
Region	10^{-3} mm^2 s^{-1}	p-value#	min^{-1}	p-value#	min^{-1}	p-value#
tumour	1.12 (0.76-1.45)		0.23 (0.10-0.58)		0.35 (0.05-0.59)	
GH	1.21 (0.95-2.33)	0.221	0.30 (0.20-0.40)	0.074	0.32 (0.20-0.38)	0.551
SH	1.21 (1.06-1.70)	0.093	0.35 (0.17-0.56)	0.114	0.12 (0.10-0.37)	0.037
PZ	1.25 (0.97-1.45)	**0.001** ↑	0.21 (0.12-0.36)	**0.006** ↓	0.25 (0.07-0.45)	**0.003** ↓

*Data are medians with (range); #difference with tumour; ↑ higher compared with tumour; ↓ lower compared with tumour; GH, glandular hyperplasia; SH, stromal hyperplasia; PZ, peripheral zone.

Table 3. Histological characteristics of tumour and normal tissue

	CD*		**GA***		**MVD***	
Region	10^3 mm^{-2}	p-value#		p-value#	mm^{-2}	p-value#
tumour	3.70 (2.45-5.16)		0.17 (0.08-0.32)		133 (71-196)	
GH	3.09 (2.13-4.37)	**0.005** ↓	0.18 (0.13-0.31)	0.363	81 (69-122)	**0.002** ↓
SH	3.63 (2.44-4.64)	0.237	0.08 (0.06-0.15)	**0.018** ↓	66 (50-87)	**0.018** ↓
PZ	3.26 (2.28-4.71)	**0.002** ↓	0.19 (0.12-0.37)	**0.023** ↑	112 (83-151)	**0.021** ↓

*Data are medians with (range); #difference with tumour; ↑ higher compared with tumour; ↓ lower compared with tumour; CD, cell density; GA, relative glandular area per voxel; MVD, microvessel density; GH, glandular hyperplasia; SH, stromal hyperplasia; PZ, peripheral zone.

tumour (p = 0.037). K^{trans} was high in both GH and SH and not different from tumour. Maximum ADC values in areas with GH and SH were higher compared with tumour, without reaching significance as large overlap with tumour regions was present.

For the microanatomical variables, tumour areas presented with higher microvessel density compared with GH and SH and higher cell density compared with GH but not SH. The variation in microvessel density according to the different ROIs is illustrated in Figure 3. Vessels in tumour regions are typically small, irregularly shaped and heterogeneous, while in GH and SH often larger vessels can be found. Wide variation in the amount of GA was found in tumour and GH. Compared to both regions, SH had smallest GA with less variation.

Tumours with Gleason score ≥7 (intermediate/high-risk disease) presented frequently with high K^{trans}, k_{ep}, CD and MVD. However, all variables were largely overlapping with tumours with Gleason score 6 (low-risk disease). No significant differences between tumours with Gleason score ≥7 and Gleason score 6 were observed (p >0.25).

Correlations were observed between ADC and cell density (r = -0.334, p = 0.022), ADC and glandular area (r = 0.402, p = 0.005) and k_{ep} and cell density (r = 0.321, p = 0.023). Tumour volume was neither related to K^{trans} (r = 0.183, p = 0.439), k_{ep} (r = 0.244, p = 0.301) and ADC (r = -0.257, p = 0.274), nor to histological variables (r < -0.068, p >0.7).

Discussion

When it comes to focal treatment of tumour areas in the prostate, perfect tumour delineation in the central gland is a challenging task. Knowledge of the various tissue types and their MRI characteristics in this part of the prostate is needed for careful interpretation of imaging. In this study, we described MRI perfusion and diffusion and detailed histological characteristics of two BPH subtypes and investigated the differences with tumour.

Major finding was the striking heterogeneity of all imaging and histological characteristics. Large overlap was present between the different tissue types.

As expected, microvessel density in tumour tissue was high.[16,17] The tumour blood vessels were mostly small and irregularly shaped. In tumour tissue, the process of neovascularisation results in a disorganised network of many small and leaky blood vessels. With DCE-MRI, the leakage of contrast agent from blood vessels into tumour tissue will therefore be different from normal tissue, resulting in differences in the measured signal enhancement curves.[13,18] Consistently, in this study K^{trans} values in tumour tissue were high.

On the other hand, GH and SH presented with lower MVD, although especially GH showed overlap with tumour tissue. The vascular network in BPH was comprised of larger and regularly shaped vessels. From literature is known that stromal BPH might present with low MVD, whereas glandular BPH might have MVDs similar to tumour tissue.[19] The observed differences in vascularity of BPH with tumour tissue did, however, not have significant impact on K^{trans} values, which were high and in the range of tumour tissue. High perfusion in CG containing BPH has been described

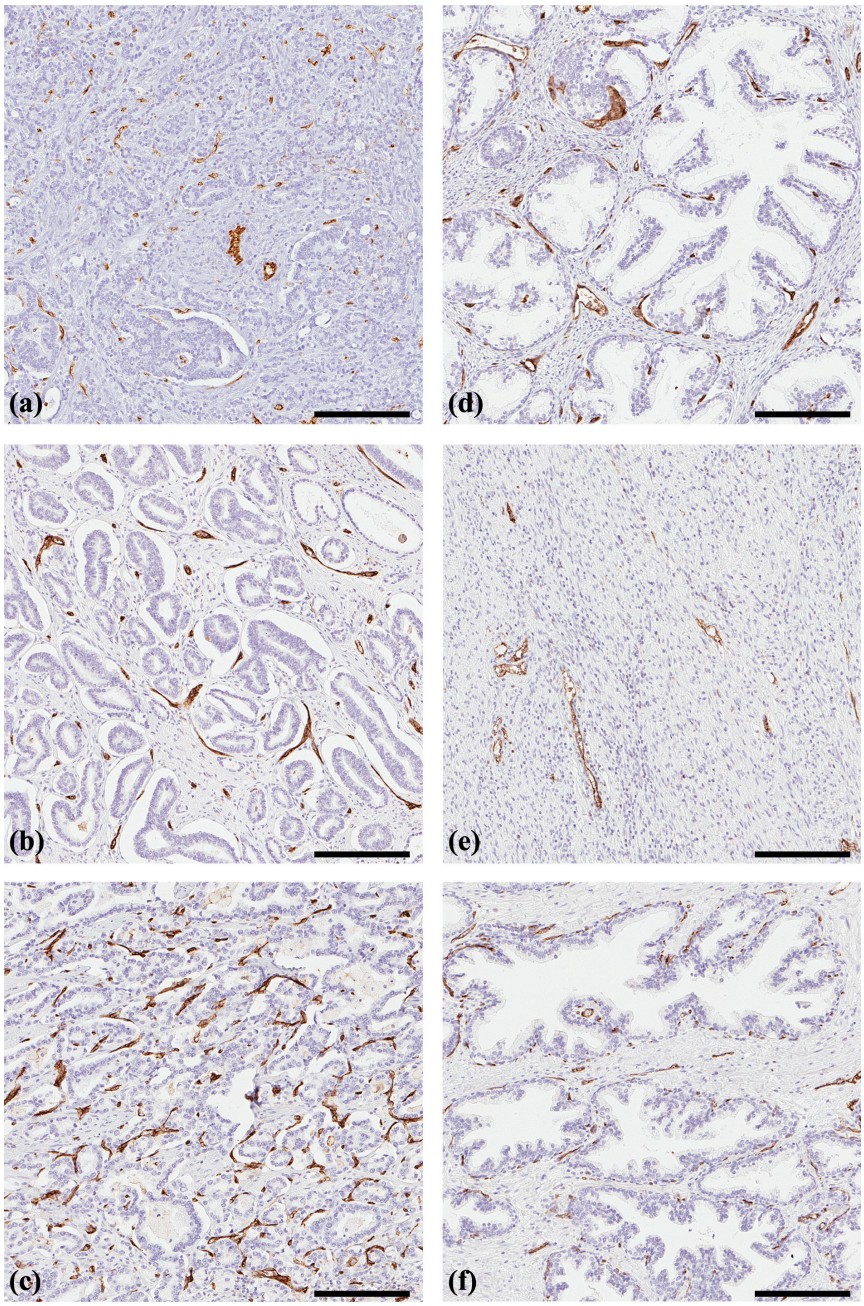

Figure 3. Immunohistochemical staining of CD31 showing microvessels in tumour (a-c), glandular hyperplasia (d), stromal hyperplasia (e) and normal peripheral zone (f). Scale bar: 100μm.

previously.[20] Especially in stromal tissues including stromal BPH, high perfusion has been reported. Although differences with tumour have been observed, overlap in perfusion between tumour and glandular or stromal BPH was present in all studies.[10,21,22]

In addition, we did not observe a correlation between microvessel density and K^{trans} or k_{ep}. Differences in study setup and patient cohort might account for the discrepancy with literature, reporting weak to moderate correlations between microvessel density and (semi-)quantitative DCE-MRI parameters.[13,23-25] An additional correlation between k_{ep} and cell density was observed. It could be speculated that this correlation might be an indirect effect of alterations in extracellular space and volume.

Our results indicate that microvessel density on its own is not satisfactory to explain perfusion characteristics of tissue. Tissue enhancement is an interplay between tissue physiology and micro-anatomy. Factors such as blood flow, vessel perfusion and the permeability or leakiness of vessels might play an important role. Enhancement of tumour tissue with many, small and leaky blood vessels might therefore equal the enhancement of BPH tissue with large, regularly shaped and well perfused vessels. In addition, this might clarify the weakness of correlations between MVD and DCE-MRI parameters reported in literature. To understand the complex relationship with perfusion, vascular area, vessel perimeter and permeability might be additional and interesting variables, but were in this study unfortunately either not available or not reliable enough.

Despite overlapping K^{trans} values, k_{ep} showed more encouraging results with a trend towards lower values in SH compared with tumour tissue. This feature of SH might therefore be of some help to distinguish this type of BPH from tumour tissue.

Tumour tissue and the stromal type of BPH presented with high cell densities. Cell density of glandular BPH was in the range of PZ tissue. For relative glandular area, wide variation was observed in tumour areas and in GH. In tumour tissue, this variation might be related to the presence of different Gleason grade patterns, although not confirmed in this study. In GH the variation might be partly induced by the selection criteria used in this study, with SH being exclusively composed of stromal tissue and GH being the remainder of the BPH tissue. GH could therefore comprise a varying amount of glandular and stromal tissue.

Despite lower cell density in GH and less GA in SH compared with tumour, no differences in ADC were observed. From literature is known that the difference in ADC values between tumour and BPH can be very ambiguous. BPH nodules might present with low and inhomogeneous ADCs.[22,26,27] However, in a study by Oto et al., significant differences in ADC have been observed between tumour, GH and SH, with highest ADCs in GH. However, considerable overlap was present between tumour regions and SH, which was also present in our study. Based on these results, the authors suggested that ADC values might help to differentiate between tumour and GH, but might be less helpful in the differentiation with SH.[10] This suggestion is, however, not supported by the results of the present study.

Weak correlations were observed between cell density and ADC and between glandular area and ADC, consistent with results of other investigators.[11,14] In addition to cell density and glandular

area, the variation in ADC values is likely to be influenced by several other factors. For instance, extracellular and intracellular space and volume, as well as membrane permeability might have important effect on the free diffusional motion of water molecules.[28]

As a reference, tumour tissue was compared with PZ, which already has been investigated thoroughly. Corresponding to literature, we found a clear difference in K^{trans}, k_{ep} and ADC between tumour and PZ.[29-31] In addition, differences in microanatomy were observed, as tumour tissue presented with higher cell density and microvessel density and less glandular area.

There are some limitations to this study. First, the number of patients was small. Second, a generic arterial input function was used for all patients. This required normalisation of the DCE-MRI variables to median PZ values to calculate correlations with histological variables.

In conclusion, this study shows that microanatomical differences are present between tumour and BPH, with microvessel density being the most pronounced. However, large heterogeneity and considerable overlap is present. This heterogeneity is reflected in the MRI parameters, limiting the differentiation between tumour and BPH based on ADC and K^{trans} values. Nevertheless, the trend towards low k_{ep} in SH might help to distinguish this type of BPH from tumour.

References

1. Cellini N, Morganti AG, Mattiucci GC, et al. Analysis of intraprostatic failures in patients treated with hormonal therapy and radiotherapy: implications for conformal therapy planning. Int J Radiat Oncol Biol Phys 2002;53:595-9.
2. Peeters ST, Heemsbergen WD, Koper PC, et al. Dose-response in radiotherapy for localized prostate cancer: results of the Dutch multicenter randomized phase III trial comparing 68 Gy of radiotherapy with 78 Gy. J Clin Oncol 2006;24:1990-6.
3. Zelefsky MJ, Pei X, Chou JF, et al. Dose escalation for prostate cancer radiotherapy: predictors of long-term biochemical tumor control and distant metastases-free survival outcomes. Eur Urol 2011;60:1133-9.
4. Lips IM, van der Heide UA, Haustermans K, et al. Single blind randomized Phase III trial to investigate the benefit of a focal lesion ablative microboost in prostate cancer (FLAME-trial): study protocol for a randomized controlled trial. Trials 2011;12:255.
5. Pinkawa M, Holy R, Piroth MD, et al. Intensity-modulated radiotherapy for prostate cancer implementing molecular imaging with 18F-choline PET-CT to define a simultaneous integrated boost. Strahlenther Onkol 2010;186:600-6.
6. Ahmed HU, Hindley RG, Dickinson L, et al. Focal therapy for localised unifocal and multifocal prostate cancer: a prospective development study. Lancet Oncol 2012;13:622-32.
7. Turkbey B, Mani H, Shah V, et al. Multiparametric 3T prostate magnetic resonance imaging to detect cancer: histopathological correlation using prostatectomy specimens processed in customized magnetic resonance imaging based molds. J Urol 2011;186:1818-24.
8. Padhani AR. Integrating multiparametric prostate MRI into clinical practice. Cancer Imaging 2011;11 Spec No A:S27-37.
9. Futterer JJ, Heijmink SW, Scheenen TW, et al. Prostate cancer localization with dynamic contrast-enhanced MR imaging and proton MR spectroscopic imaging. Radiology 2006;241:449-58.
10. Oto A, Kayhan A, Jiang Y, et al. Prostate cancer: differentiation of central gland cancer from benign prostatic hyperplasia by using diffusion-weighted and dynamic contrast-enhanced MR imaging. Radiology 2010;257:715-23.
11. Langer DL, van der Kwast TH, Evans AJ, et al. Prostate tissue composition and MR measurements: investigating the relationships between ADC, T2, K(trans), v(e), and corresponding histologic features. Radiology 2010;255:485-94.
12. Groenendaal G, Borren A, Moman MR, et al. Pathologic validation of a model based on diffusion-weighted imaging and dynamic contrast-enhanced magnetic resonance imaging for tumor delineation in the prostate peripheral zone. Int J Radiat Oncol Biol Phys 2012;82:e537-44.
13. Schlemmer HP, Merkle J, Grobholz R, et al. Can pre-operative contrast-enhanced dynamic MR imaging for prostate cancer predict microvessel density in prostatectomy specimens? Eur Radiol 2004;14:309-17.
14. Gibbs P, Liney GP, Pickles MD, Zelhof B, Rodrigues G, Turnbull LW. Correlation of ADC and T2 measurements with cell density in prostate cancer at 3.0 Tesla. Invest Radiol 2009;44:572-6.
15. Groenendaal G, Moman MR, Korporaal JG, et al. Validation of functional imaging with pathology for tumor delineation in the prostate. Radiother Oncol 2010;94:145-50.

16. van Niekerk CG, van der Laak JA, Borger ME, et al. Computerized whole slide quantification shows increased microvascular density in pT2 prostate cancer as compared to normal prostate tissue. Prostate 2009;69:62-9.

17. Pallares J, Rojo F, Iriarte J, Morote J, Armadans LI, de Torres I. Study of microvessel density and the expression of the angiogenic factors VEGF, bFGF and the receptors Flt-1 and FLK-1 in benign, premalignant and malignant prostate tissues. Histol Histopathol 2006;21:857-65.

18. Franiel T, Ludemann L, Rudolph B, Lutterbeck E, Hamm B, Beyersdorff D. Differentiation of prostate cancer from normal prostate tissue: role of hotspots in pharmacokinetic MRI and histologic evaluation. AJR Am J Roentgenol 2010;194:675-81.

19. Deering RE, Bigler SA, Brown M, Brawer MK. Microvascularity in benign prostatic hyperplasia. Prostate 1995;26:111-5.

20. Kershaw LE, Hutchinson CE, Buckley DL. Benign prostatic hyperplasia: evaluation of T1, T2, and microvascular characteristics with T1-weighted dynamic contrast-enhanced MRI. J Magn Reson Imaging 2009;29:641-8.

21. Noworolski SM, Henry RG, Vigneron DB, Kurhanewicz J. Dynamic contrast-enhanced MRI in normal and abnormal prostate tissues as defined by biopsy, MRI, and 3D MRSI. Magn Reson Med 2005;53:249-55.

22. Noworolski SM, Vigneron DB, Chen AP, Kurhanewicz J. Dynamic contrast-enhanced MRI and MR diffusion imaging to distinguish between glandular and stromal prostatic tissues. Magn Reson Imaging 2008;26:1071-80.

23. Ren J, Huan Y, Wang H, et al. Dynamic contrast-enhanced MRI of benign prostatic hyperplasia and prostatic carcinoma: correlation with angiogenesis. Clin Radiol 2008;63:153-9.

24. Franiel T, Ludemann L, Rudolph B, et al. Prostate MR imaging: tissue characterization with pharmacokinetic volume and blood flow parameters and correlation with histologic parameters. Radiology 2009;252:101-8.

25. Oto A, Yang C, Kayhan A, et al. Diffusion-weighted and dynamic contrast-enhanced MRI of prostate cancer: correlation of quantitative MR parameters with Gleason score and tumor angiogenesis. AJR Am J Roentgenol 2011;197:1382-90.

26. Ren J, Huan Y, Wang H, et al. Diffusion-weighted imaging in normal prostate and differential diagnosis of prostate diseases. Abdom Imaging 2008;33:724-8.

27. Wang XZ, Wang B, Gao ZQ, et al. Diffusion-weighted imaging of prostate cancer: correlation between apparent diffusion coefficient values and tumor proliferation. J Magn Reson Imaging 2009;29:1360-6.

28. Anderson AW, Zhong J, Petroff OA, et al. Effects of osmotically driven cell volume changes on diffusion-weighted imaging of the rat optic nerve. Magn Reson Med 1996;35:162-7.

29. Engelbrecht MR, Huisman HJ, Laheij RJ, et al. Discrimination of prostate cancer from normal peripheral zone and central gland tissue by using dynamic contrast-enhanced MR imaging. Radiology 2003;229:248-54.

30. Isebaert S, De Keyzer F, Haustermans K, et al. Evaluation of semi-quantitative dynamic contrast-enhanced MRI parameters for prostate cancer in correlation to whole-mount histopathology. Eur J Radiol 2012;81:e217-22.

31. Haider MA, van der Kwast TH, Tanguay J, et al. Combined T2-weighted and diffusion-weighted MRI for localization of prostate cancer. AJR Am J Roentgenol 2007;189:323-8.

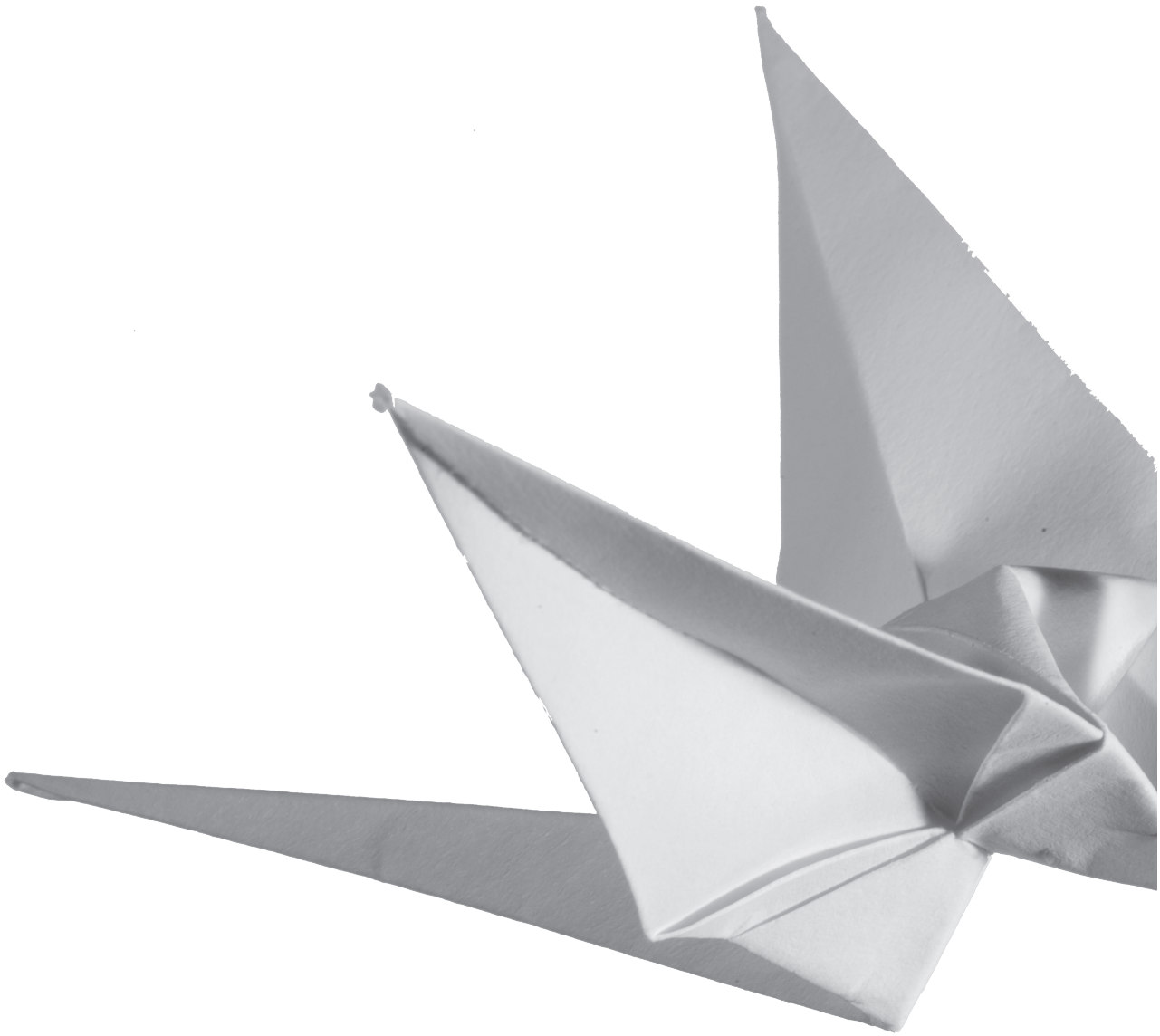

6

Expression of Hypoxia-Inducible Factor-1α and -2α in whole-mount prostate histology: Relation with dynamic contrast-enhanced MRI and Gleason score

A. Borren,
G. Groenendaal,
P. van der Groep,
M.R. Moman,
A.E. Boeken Kruger,
U.A. van der Heide,
T.N. Jonges,
P.J. van Diest,
M. van Vulpen,
M.E.P. Philippens.

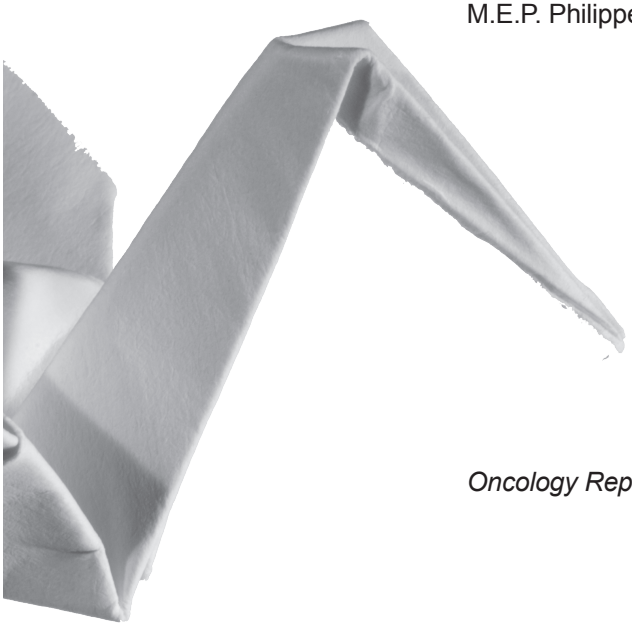

Oncology Reports. 2013;29:2249-54

Abstract

Background

The aim of this study was to investigate the association between the immunohistochemical expression of hypoxia-inducible factor (HIF)-1α and HIF-2α and dynamic contrast-enhanced magnetic resonance imaging (DCE-MRI) parameters K^{trans} and k_{ep} in prostate cancer.

Materials and Methods

Fifteen patients with biopsy-confirmed prostate cancer underwent a pre-operative 3T DCE-MRI scan. Immunohistochemical analysis of HIF-1α and HIF-2α, and of CD31 for microvessel density (MVD) was performed. Tumour areas were delineated on whole-mount histopathological sections. Nuclear HIF expression was correlated with the quantitative DCE-MRI parameters K^{trans} and k_{ep}, MVD and Gleason score.

Results

HIF expression was highly heterogeneous within tumours and between patients. Pronounced expression of HIF-2α was present, while HIF-1α expression was more limited. Larger tumours showed higher HIF-2α expression ($p = 0.041$). A correlation between HIF-2α and K^{trans} $p5^{th}$ was found ($r = 0.30$, $p = 0.02$), but no differences in K^{trans}, k_{ep} and MVD were observed for different levels of HIF expression. HIF-expression was not associated with Gleason score.

Conclusions

In this whole-mount prostate cancer study, larger prostate tumours showed frequently high HIF-2α expression, suggesting that larger tumours are clinically most relevant. However, HIF-1α and HIF-2α were not correlated with DCE-MRI parameters. Given the pronounced expression of HIF-2α and independence of Gleason score, HIF expression might function as a biomarker to guide boost dose prescription.

Introduction

Biochemical failure and local recurrences of prostate cancer after radiotherapy could be reduced by escalation of the radiation dose to the prostate.[1,2] As local recurrences frequently originate at the site of the macroscopic tumour, the focus for further dose escalation has to be on focal tumour areas most in need of aggressive treatment.[3-5]

Based on recent studies, we know that hypoxia-inducible factor (HIF) may be related to prostate cancer outcome, as higher HIF-expression was found to be associated with increased risk of biochemical failure and with reduced survival.[6-8] Because of this relationship, tumour areas with high HIF expression might be candidates for focal boost.

HIF is a transcription factor which can be regulated by hypoxia- dependent and hypoxia-independent mechanisms. The hypoxia-dependent mechanism has been the most investigated; levels of HIFα subunits in the cell increase under hypoxic conditions resulting from an imbalance between oxygen demand and oxygen delivery to the tissue. In this pathway, HIF transcription factors act as key regulators of the cellular response to hypoxia and modulate the expression of genes involved in processes such as cell metabolism, proliferation and angiogenesis. The hypoxia-independent pathway of HIF-regulation is the induction of HIFα expression by increased oncogenic signaling in cancer cells.[9] Most studies have focused on the presence of HIF-1α. However, HIF-2α may play an additional and important role in prostate cancer.[8,9] The role of HIF-2α in prostate cancer is still underexposed and its distribution in whole-mount prostate histology not yet described. This is the first study describing the distribution of HIF-2α expression in whole-mount prostate histology.

For the non-invasive detection of prostate tumour areas, dynamic contrast-enhanced magnetic resonance imaging (DCE-MRI) is one of the tools currently used in clinical practice.[10] The aim of the present study was to investigate the relation of the DCE-MRI parameters K^{trans} and k_{ep} with the immunohistochemical expression of HIF-1α and HIF-2α in whole-mount prostate histology.

Materials and Methods

Patients

The study was approved by the Institutional Review Board of the University Medical Center Utrecht, and informed consent was obtained from all patients. Twenty patients were enrolled in the study. All patients had biopsy-confirmed prostate cancer and were scheduled for a robotic-assisted laparoscopic prostatectomy (RALP). None of the patients was treated with androgen deprivation therapy. Five patients were excluded from analysis, due to the unavailability of pathological material in 2 patients, considerable motion during MR image acquisition in 1 patient, and in 2 patients the prostate specimen was severely deformed which hampered accurate registration. Clinical characteristics of the 15 eligible patients are shown in Table 1.

Table 1. Patient characteristics

Characteristic		Value
Patient number		15
Patient age (years)*		63 (48-74)
PSA level (ng/mL)*		12 (5-29)
Pathological tumor stage#	T2a	2
	T2c	5
	T3a	8
Gleason score#	3+3=6	2
	3+4=7	10
	3+5=8	3
Tumor number		34
	<0.22 cm^3	14
	>0.22 cm^3	20
Tumor volume*		0.73 (0.01-9.36)
	<0.22 cm^3	0.17 (0.01-0.21)
	>0.22 cm^3	1.59 (0.42-9.36)

*median and (range); #patient numbers

MR imaging

Multi-parametric imaging was performed on a 3T MRI-scanner (Philips Achieva, Best, The Netherlands), including a T2w sequence and DCE-MRI. No endorectal coil was used. T2w images were acquired with a fast spin-echo sequence, TR/TE=8396/120 ms, echo train length 13, acquisition matrix 256×256, field of view (FOV)= 20 cm, slice thickness 3 mm, slice gap 1 mm. The DCE-MRI protocol consisted of a 3D spoiled gradient echo sequence (20 transverse slices, slice thickness = 2.5 mm, TR/TE = 4.0/1.7 ms, flip angle 8°, FOV = 40 cm, acquisition matrix 160×128). Scans were repeated 120 times at an interval of 2.5 s. A concentration of 0.1 ml/kg of Gadobutrol (1.0M) (Gadovist®, Schering AG, Berlin, Germany) contrast was injected at 2 ml/s, followed by a saline flush. The tracer kinetics data were analysed with the Tofts model, as previously described.[11] This yielded 3D absolute K^{trans} and k_{ep} parameter maps. A generic arterial input function (AIF) was used for all patients, due to measurement errors on the patient-specific input functions. To account for patient-specific differences in AIF, DCE-MRI parameters were normalized to the median value in normal PZ for correlation analyses.[12]

MRI-pathology registration

After prostatectomy, the prostate specimens were processed and registered as previously described.[12] In short, the prostate was cut into 3-mm thick slices, and whole-mount microscopic slices stained with hematoxylin and eosin (H&E) were created. Tumour areas were delineated by a pathologist and assigned with a Gleason score. The registration process was performed in three steps:

1) reconstruction of the prostate from 3-mm thick macroscopic slices; 2) registration of microscopic slices to the reconstructed prostate; and 3) registration between the reconstructed prostate and the T2w MR images. On average, the registration error between MR images and histopathological data was approximately one voxel (reconstructed voxel size 2.5×2.5×2.5mm^3).[12]

Immunohistochemistry

After deparaffination and rehydration, endogenous peroxidase was blocked and antigen retrieval was performed. For microvessel density analysis, slides were incubated for 1 hour at room temperature with a monoclonal mouse anti-human CD31 antibody (1:50) (Leica Microsystems, Wetzlar, Germany). For HIF-1α and HIF-2α, slides were incubated overnight at 4°C using a monoclonal mouse anti-human HIF-1α antibody (1:50) (BD Transduction Laboratories, Lexington, KY, USA) and a polyclonal rabbit anti-human HIF-2α antibody (1:700) (Novus Biologicals, Littleton, CO, USA), respectively. Subsequently, slides were incubated with a secondary antibody (CD31 and HIF-1α: Novolink Polymer Detection System; Leica Microsystems and HIF-2α: Brightvision; Immunologic, Duiven, The Netherlands). All slides were developed with diaminobenzidine followed by hematoxylin counterstaining.

Tissue evaluation

Three whole-mount microscopic slides per patient containing normal tissue, the index tumour and probable secondary tumours, were chosen for further analysis. CD31-stained slides were digitised at microscopic resolution and analysed in ImageScope v10.0 using the Microvessel Analysis Algorithm v1 (Aperio Technologies, Vista, CA, USA) to assess the microvessel density (MVD). To compensate for variation in staining intensity, the settings of the algorithm were evaluated qualitatively and optimised for every batch by adjusting on test regions.

Scoring of HIF-1α and HIF-2α was performed by consensus of two observers. The percentage of positively stained nuclei in whole tumour regions was estimated per slide, ignoring diffuse cytoplasmic staining.

Regions of interest (ROI) were defined based on the HIF-expression pattern. Areas within a tumour with a distinct HIF-expression pattern were investigated as separate regions, which could result in more regions of interest within a single tumour. This was carried out separately for HIF-1α and HIF-2α.

Statistical analysis

Median K^{trans}, k_{ep} and MVD were calculated for each ROI. For analysis of K^{trans}, k_{ep} and MVD, ROIs were selected within tumours with a volume >0.22 cm^3 (diameter >3 voxels = 7.5 mm), as partial volume effects and registration errors have a large influence on smaller tumours. Normalised DCE-MRI parameters were used for statistical analysis to account for interpatient variability. Differences between ROIs were assessed with the Mann-Whitney U and Kruskal-Wallis test and Spearman's correlation coefficients were calculated (SPSS v20, SPSS Inc., Chicago, IL, USA). P-values ≤0.05 were considered to indicate statistically significant differences.

Table 2. Distribution of HIF-1α and HIF-2α in patients and tumours

Characteristics		**HIF-1a** [n/total (%)]	**HIF-2a** [n/total (%)]
Patients	*HIF-positive*	12/15 (80)	14/15 (93)
Tumors total	*HIF-positive*	20/34 (59)	28/34 (82)
Tumors <0.22 cm^3	*HIF-positive*	7/14 (50)	9/14 (64)
	*Maximum HIF-expression**	20%	35%
Tumors >0.22 cm^3	*HIF-positive*	13/20 (65)	19/20 (95)
	*Maximum HIF-expression**	50%	90%

*Percentage of tumour cells with positive staining; HIF, hypoxia-inducible factor.

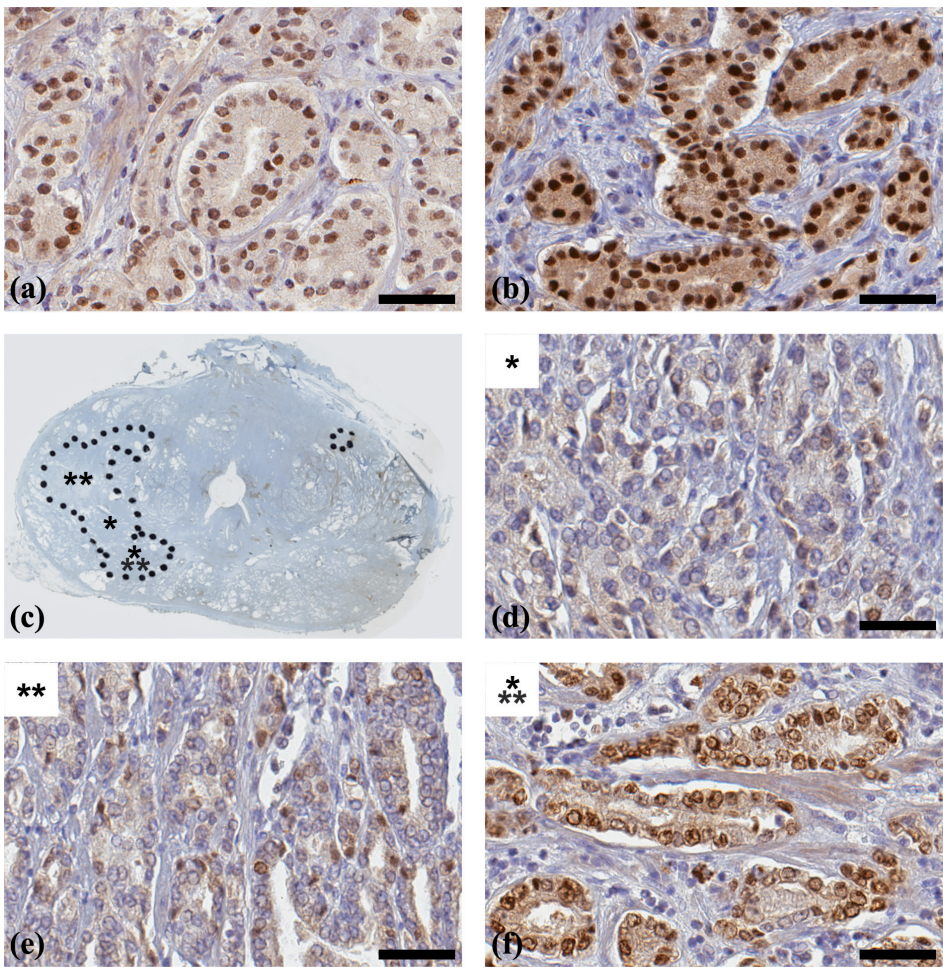

Figure 1. Example of (a) strong HIF-1α staining and (b) strong HIF-2α staining in the same patient. Second patient example showing the heterogeneity of HIF-2α expression within one tumour. (c) Overview of HIF-2α positive areas with HIF-2α expression of (d) 5%, (e) 10% and (f) 90%. Scale bar: 50 μm.

Results

Of the 15 patients, most showed HIF-1α and HIF-2α positive tumour areas (Table 2). The distribution of HIF expression was highly heterogeneous: (1) negative and positive tumours were found within patients, (2) negative and positive areas were found within tumours, and (3) within a single tumour the range in HIF-positivity could be large with 5-35% for HIF-1α and 2-90% for HIF-2α. In Figure 1, this heterogeneous distribution is illustrated for HIF-2α. Tumour areas showing HIF expression, could either be very small or comprise the entire tumour. There was a marked difference in the distribution of HIF-1α and HIF-2α. HIF-1α expression was often present focally in small regions within tumours, while HIF-2α frequently was expressed in whole tumour regions. Furthermore, the maximum HIF 1α expression was 50%, whereas HIF-2α ranged to 90%. HIF-expression was sometimes found in normal tissue, but was not taken into account.
For all HIF-1α ROIs, median values (range) were: K^{trans} 0.241 min^{-1} (0.108-0.599), k_{ep} 0.356 min^{-1} (0.049-0.581) and MVD 135/mm^2 (50-230). For HIF-2α these values were: K^{trans} 0.256 min^{-1} (0.109-0.609), k_{ep} 0.362 (0.051-0.888) and MVD 115/mm^2 (55-225). No differences in median K^{trans}, k_{ep} and MVD were observed between different HIF-expression levels (Figure 2). In addition, classification into groups according to different HIF-expression levels (e.g. HIF-positive vs.

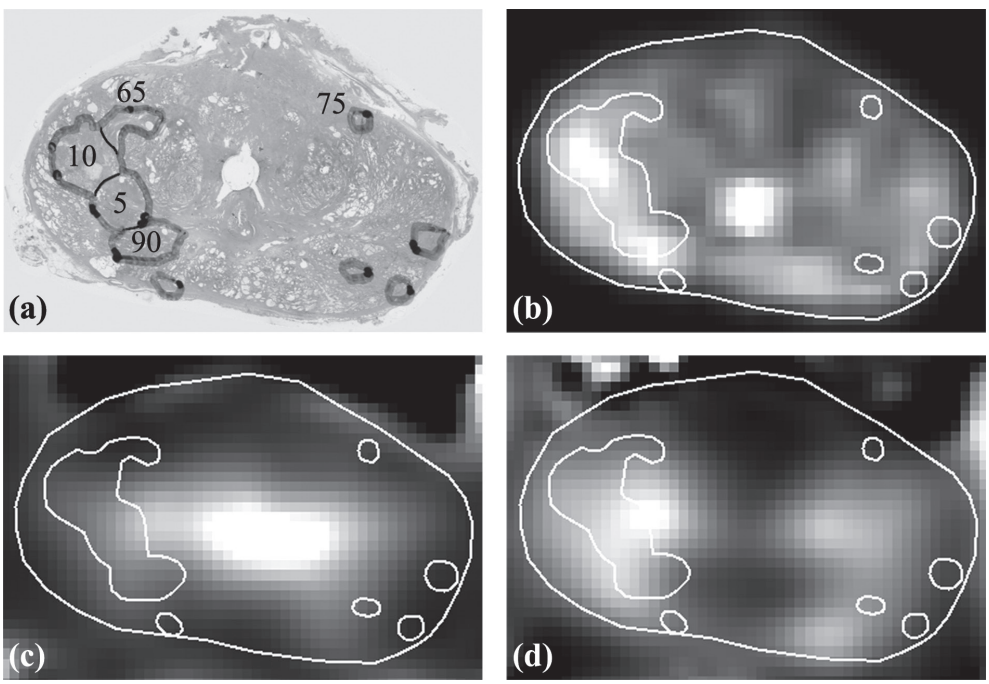

Figure 2. Patient example showing the absence of correlations between (a) percentages of HIF-2α expression and (b) K^{trans}, (c) k_{ep} and (d) MVD. HIF-1α expression in this patient was 0% in all tumour regions.

HIF-negative and 0-1% vs. >1%) did not show any significant differences. As shown in Figure 3, the perfusion parameters and MVD in HIF-negative tumour regions (with 0% HIF expression) overlapped with those in all other HIF-positive ROIs.
Furthermore, ROIs were classified into groups with high/low K^{trans} and high/low k_{cp}, using median normalised K^{trans} and k_{ep} values as threshold. No differences in HIF expression were present between groups ($p > 0.16$).

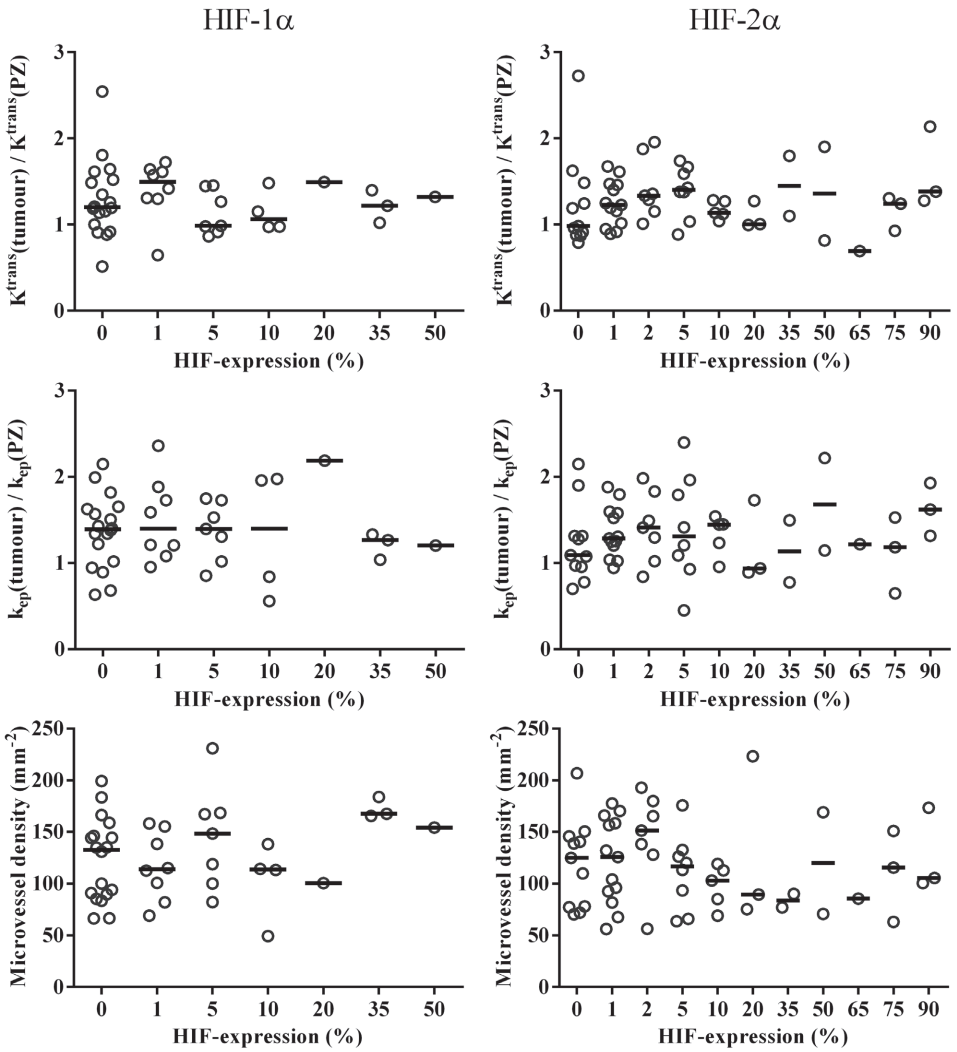

Figure 3. Graphs indicating the large heterogeneity of K^{trans}, k_{ep} and MVD for the different HIF-expression levels. Bar, median.

Percentages of HIF-1α and HIF-2α expression were not correlated with median K^{trans}, k_{ep} and MVD (p >0.2).HIF-2α expression was correlated with the K^{trans} 5th percentile (r = 0.30, p = 0.02) and with the MVD 95th percentile (r = -0.39, p = 0.002). HIF-1α and HIF-2α were not correlated with each other (p = 0.49) and did both not correlate with Gleason score (p >0.77).
Larger tumours (>0.22 cm^3) were more often HIF-2α positive (p = 0.023) than smaller tumours and showed higher levels of HIF-2α expression (p = 0.041). This association of HIF-expression with tumour volume was less clear for HIF-1α (Figure 4). In addition, larger tumours showed more frequent presence of Gleason grade 4 (p = 0.005), but for Gleason grade 5 no difference between smaller and larger tumours was observed (p = 0.955).

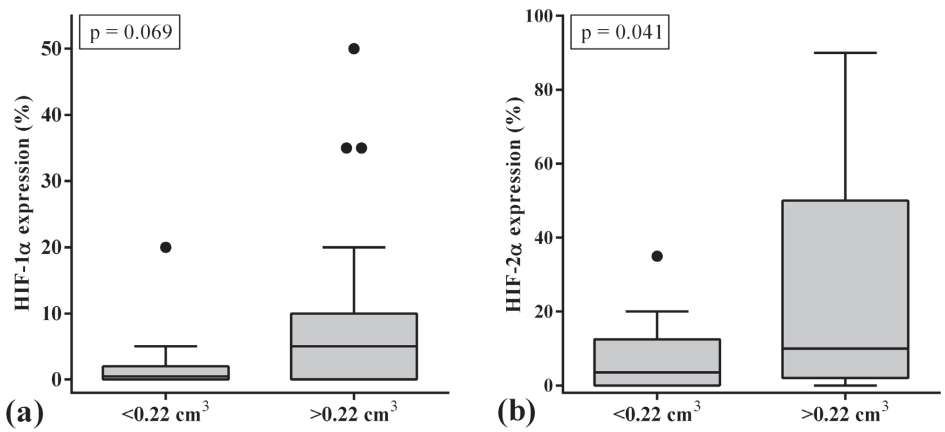

Figure 4. (a) HIF-1α and (b) HIF-2α expression vs. tumour volume.

Discussion

This is the first study describing the distribution of HIF-2α expression in whole-mount prostate histology. We described the distribution of nuclear HIF-1α and HIF-2α expression in prostate cancer and investigated the relationship with DCE-MRI parameters and MVD. HIF distribution was highly heterogeneous, with pronounced expression of HIF-2α, while HIF-1α was more limited. To date, the presence of HIF-2α in primary prostate cancer has been described in regards to data of tissue microarrays only.[8,13] Boddy et al suggested that HIF-2α may be the most important isoform in prostate cancer, as they showed that HIF-2α expression was negatively correlated with the presence of prolyl hydroxylase enzyme PHD2.[13] Under hypoxic conditions, this enzyme becomes inactive, with subsequent higher levels of HIF-2α. In the present study, we underscore this suggestion, as we found that the expression of HIF-2α was more pronounced and reached higher levels compared with HIF-1α.

In addition, we observed higher HIF-2α expression levels in larger tumours. In light of the prognostic relevance of HIF expression, this suggests that the larger tumours are most clinically relevant. These larger tumours have higher chance to be detected with MRI compared with smaller tumours.[14] However, we found that high HIF expression could be present as well in small tumour regions. Unfortunately, these small tumours may not be detected with MRI.

Furthermore, we observed a weak positive correlation between HIF-2α and the K^{trans} 5th percentile, which indicates that the minimum K^{trans} is higher in tumours with higher HIF-2α expression. This may facilitate tumour detection, as higher K^{trans} will increase the conspicuity of tumours voxels.[12]

Despite these encouraging results, we did not observe any differences and correlations between HIF expression and median DCE-MRI parameters or MVD. The question is whether HIF expression in prostate cancer is regulated in an hypoxia-dependent or hypoxia-independent manner. If hypoxia-dependent, HIF induces angiogenesis by upregulation of vascular endothelial growth factor. Therefore, we would expect high MVD and high K^{trans} in regions with high HIF expression. However, HIF-expression may be induced by several non-hypoxia-related factors.[15] In a recent study, Garcia-Parra et al put a critical note on the association between HIF-1α expression and hypoxia.[16] While they found variable HIF-1α staining, they were not able to show hypoxia in prostate cancer with ^{18}F-FAZA PET/CT or with immunohistochemical staining of CAIX which is a downstream target of HIF-1α. Based on these findings, they suggest that the expression of HIF-1α may be independent of tissue hypoxia.

Hypoxia-independence of HIF-expression may clarify why we did not observe a correlation between HIF expression and DCE-MRI parameters and MVD.

For both HIF-1α and HIF-2α, a number of studies have shown an inverse relationship between HIF expression and biochemical recurrence.[6-8] This prognostic value of HIF expression appears to be independent of the Gleason score. Similar to other reports, we did not find a correlation between expression of HIF-1α or HIF-2α and Gleason score.[6,13,16] Therefore, HIF expression in prostate tumour biopsies may be used as input for individual boost dose prescription, to achieve personalised radiotherapy.[17]

This study has some limitations. First, the number of patients was relatively small. Definitive conclusions on the relationship between HIF expression and DCE-MRI must be verified in larger studies. Nevertheless, as in this study the p-values found with correlation analyses were far from significance, clinical relevant correlations might be absent as well in larger cohorts. Second, although we used a robust registration method, a registration error existed between DCE-MRI data and pathology.

In conclusion, in the present study we demonstrated that expression of HIF-1α and HIF-2α is not correlated with DCE-MRI parameters. Larger tumours showed frequently high HIF-2α expression, which suggests that larger tumours are most clinically relevant tumours. Given the pronounced expression of HIF-2α and independence of Gleason score, HIF expression might function as biomarker to guide boost dose prescription.

References

1. Peeters ST, Heemsbergen WD, Koper PC, et al. Dose-response in radiotherapy for localized prostate cancer: results of the Dutch multicenter randomized phase III trial comparing 68 Gy of radiotherapy with 78 Gy. J Clin Oncol 2006;24:1990-6.
2. Zelefsky MJ, Pei X, Chou JF, et al. Dose escalation for prostate cancer radiotherapy: predictors of long-term biochemical tumor control and distant metastases-free survival outcomes. Eur Urol 2011;60:1133-9.
3. Cellini N, Morganti AG, Mattiucci GC, et al. Analysis of intraprostatic failures in patients treated with hormonal therapy and radiotherapy: implications for conformal therapy planning. Int J Radiat Oncol Biol Phys 2002;53:595-9.
4. Pucar D, Hricak H, Shukla-Dave A, et al. Clinically significant prostate cancer local recurrence after radiation therapy occurs at the site of primary tumor: magnetic resonance imaging and step-section pathology evidence. Int J Radiat Oncol Biol Phys 2007;69:62-9.
5. Lips IM, van der Heide UA, Haustermans K, et al. Single blind randomized Phase III trial to investigate the benefit of a focal lesion ablative microboost in prostate cancer (FLAME-trial): study protocol for a randomized controlled trial. Trials 2011;12:255.
6. Vergis R, Corbishley CM, Norman AR, et al. Intrinsic markers of tumour hypoxia and angiogenesis in localised prostate cancer and outcome of radical treatment: a retrospective analysis of two randomised radiotherapy trials and one surgical cohort study. Lancet Oncol 2008;9:342-51.
7. Gravdal K, Halvorsen OJ, Haukaas SA, Akslen LA. Proliferation of immature tumor vessels is a novel marker of clinical progression in prostate cancer. Cancer Res 2009;69:4708-15.
8. Nanni S, Benvenuti V, Grasselli A, et al. Endothelial NOS, estrogen receptor beta, and HIFs cooperate in the activation of a prognostic transcriptional pattern in aggressive human prostate cancer. J Clin Invest 2009;119:1093-108.
9. Keith B, Johnson RS, Simon MC. HIF1alpha and HIF2alpha: sibling rivalry in hypoxic tumour growth and progression. Nat Rev Cancer 2011;12:9-22.
10. Futterer JJ, Heijmink SW, Scheenen TW, et al. Prostate cancer localization with dynamic contrast-enhanced MR imaging and proton MR spectroscopic imaging. Radiology 2006;241:449-58.
11. Groenendaal G, Moman MR, Korporaal JG, et al. Validation of functional imaging with pathology for tumor delineation in the prostate. Radiother Oncol 2010;94:145-50.
12. Groenendaal G, Borren A, Moman MR, et al. Pathologic validation of a model based on diffusion-weighted imaging and dynamic contrast-enhanced magnetic resonance imaging for tumor delineation in the prostate peripheral zone. Int J Radiat Oncol Biol Phys 2012;82:e537-44.
13. Boddy JL, Fox SB, Han C, et al. The androgen receptor is significantly associated with vascular endothelial growth factor and hypoxia sensing via hypoxia-inducible factors HIF-1a, HIF-2a, and the prolyl hydroxylases in human prostate cancer. Clin Cancer Res 2005;11:7658-63.
14. Roethke MC, Lichy MP, Jurgschat L, et al. Tumorsize dependent detection rate of endorectal MRI of prostate cancer--a histopathologic correlation with whole-mount sections in 70 patients with prostate cancer. Eur J Radiol 2011;79:189-95.
15. Banham AH, Boddy J, Launchbury R, et al. Expression of the forkhead transcription factor FOXP1 is associated both with hypoxia inducible factors (HIFs) and the androgen receptor in prostate cancer but is not directly regulated by androgens or hypoxia. Prostate 2007;67:1091-8.

16. Garcia-Parra R, Wood D, Shah RB, et al. Investigation on tumor hypoxia in resectable primary prostate cancer as demonstrated by ^{18}F-FAZA PET/CT utilizing multimodality fusion techniques. Eur J Nucl Med Mol Imaging 2011;38:1816-23.

17. Bentzen SM, Gregoire V. Molecular imaging-based dose painting: a novel paradigm for radiation therapy prescription. Semin Radiat Oncol 2011;21:101-10.

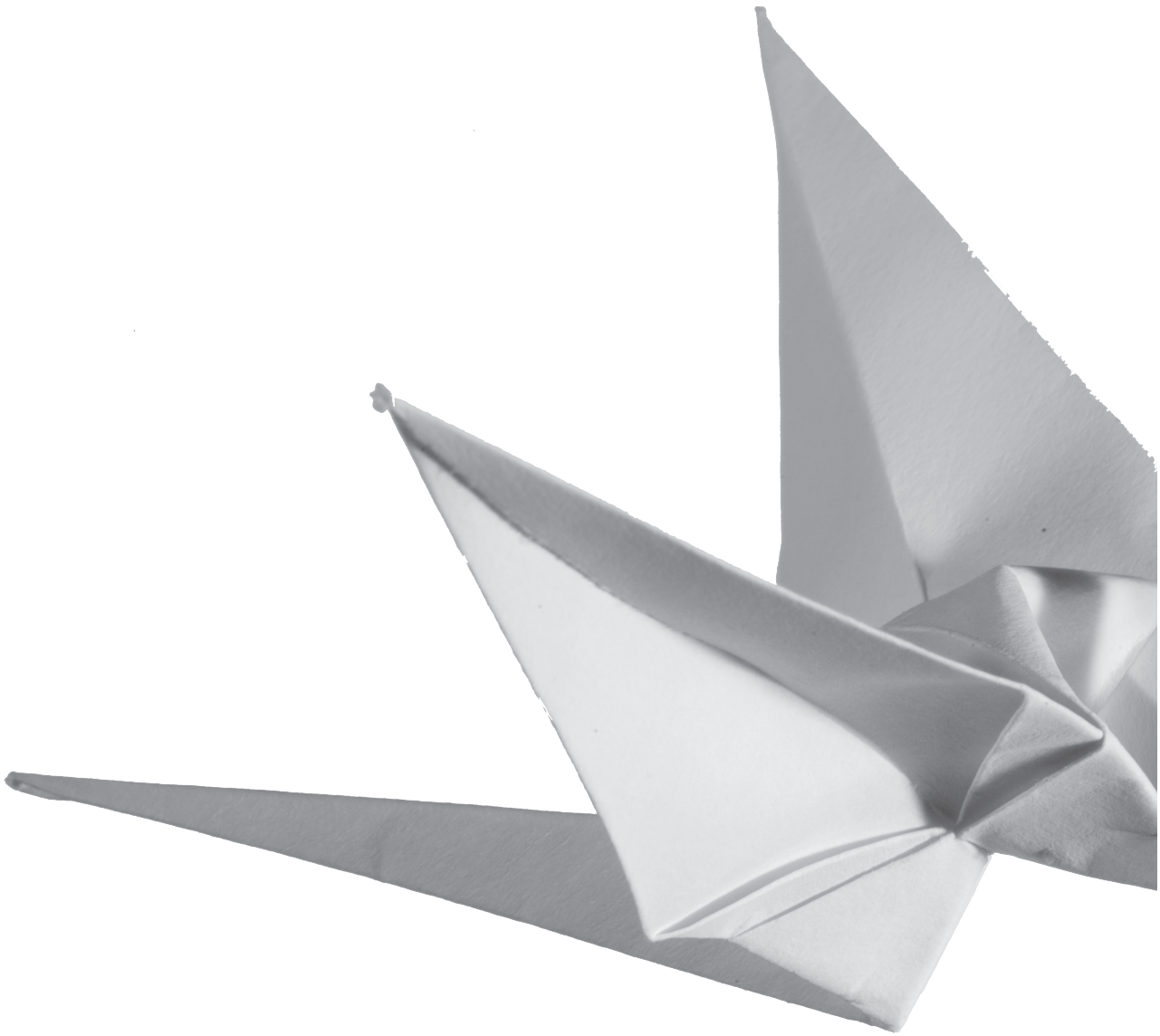

7

Summary and general discussion

Clinical background

Focal boost to the most important areas in the prostate is a promising technique to improve the outcome of patients with intermediate- and high-risk prostate cancer. With this approach, a very high radiation dose can be delivered without exceeding the dose constraints on organs at risk and therefore avoiding an increase in toxicity. Several studies have shown that it is feasible to deliver such a high dose to a selected area in the prostate. With minor adjustments, the technique of focal boosting can be used to give focal therapy to low-risk prostate cancer patients, diminishing their treatment side effects.

In focal boosting and focal therapy, the selection of intra-prostatic tumour areas is a crucial step. There are two important selection criteria. The first criterion is the location of the dominant tumour lesion, as local recurrences frequently originate at this side.[1-3] The second criterion is the presence of aggressive and radioresistant tumour characteristics, for example with high Gleason score and high cell density.[4,5]

For the non-invasive visualization of the tumour areas multiparametric MRI is the modality of choice.[6] In this thesis, we used T2w MR scans for visualization of anatomical details and added DCE-MRI and DWI sequences to gather information about the perfusion and diffusion characteristics of the tissue.[7,8] This mp-MRI combination is applied in a randomized trial at our radiotherapy department and used for the determination of the dominant tumour.[9] Although it is feasible to delineate the tumour region in most patients, the interpretation of the MRI scans remains a challenge. Especially the exact tumour boundaries are often difficult to define.

The main goal of this thesis was to understand the histological background of functional MR imaging of the prostate, to come to more robust, MRI-based voxel-wise prostate tumour delineation.

Model with high accuracy

Step 1: improve manual delineation with a statistical model.

To come to objective tumour delineation, we developed a statistical model to predict the tumour probability for every single voxel in the peripheral zone, based on DCE-MRI and DWI parameters (chapter 2). The model was validated on prostate histology of a group of prostatectomy patients. The diagnostic performance appeared to be very good, yielding an area under the curve (AUC) of 0.89. The continuous model outcome was stratified into three different risk levels for tumour presence: gross tumour volume, high-risk clinical target volume and non-suspicious tissue. These risk levels could serve as an input for tumour delineation and in turn for radiation dose planning, with higher doses according to higher risk levels. Implementation of the model in clinical practice will significantly reduce observer dependence in the delineation of tumour areas and make delineation more objective and robust. In theory, the continuous model outcome could even be used as guidance for voxel based dose planning, without delineation of a certain tumour area. Voxels with higher tumour probability might receive correspondingly higher doses.[10]

Characteristics of detected vs. non-detected tumour voxels

Step 2: model is nevertheless not perfect: voxels are missed. What are the characteristics of these voxels? In other words: how important are the missed voxels? Are they going to diminish the effect of focal boosting? Are they aggressive and do they definitely need to be treated in case of focal therapy?

Although the diagnostic performance is high, prediction of tumour presence with the model is not perfect. Before starting tweaking the model in order to improve tumour detection accuracy, we investigated whether tissue characteristics are related to the model outcome (chapter 3). Correlation with prostate histology revealed in correctly detected tumour voxels high cell density, high microvessel density and a trend towards higher Gleason scores. On the other hand, non-detected tumour voxels had cell densities and microvessel densities resembling normal tissue. This indicates that the detection of tumour voxels depends on their histological characteristics, rather than on presence of tumour or not. Additional factors, studied in this thesis, were tumour volume and the expression of hypoxia-inducible factor (HIF) 1α and HIF-2α. Larger tumour volumes were associated with lower ADC values (chapter 4) and with higher levels of HIF-2α expression. Furthermore, larger tumours showed more frequent high Gleason grades (chapter 6). Larger tumours are detected more frequently and determining outcome after radiotherapy.[11,12] Altogether these results indicate that the clinically most important tumour voxels, which are likely in need of higher radiation doses, are detected accurately.

The major finding of this thesis was the striking heterogeneity of prostate tissue and of MRI parameters. Large overlap in histological parameters was present between different tissue types. Tumour tissue can present with relative low cell density, likely to be associated with Gleason grade 3. On the other hand, normal tissue can present with high cell density and microvessel density. Although not investigated, benign conditions of the tissue such as prostatitis, basal cell hyperplasia and peripheral zone atrophy, might be responsible for the extensive variation in non-malignant tissue. The heterogeneity indicates that already in histology for the investigated characteristics it is hard to define a clear cut-off between tumour tissue and normal tissue.

The variation in MRI parameters like ADC and K^{trans} could, however, only be partly explained by the variation in cell density and microvessel density (chapter 4 and 5). The observed correlations were all weak to moderate. Despite the very accurate MRI-histology registration method, the registration error of approximately one voxel might in this case have influenced the results. Moreover, the investigated histological parameters are a strong simplification of the complexity of the tissue microanatomy. The measured MRI signal is the resultant of interplay among all various aspects of this environment, including tissue physiology with factors like blood flow, leakiness of vessels and membrane permeability. Therefore, for MRI parameters 100% differentiation between tumour and normal tissue will be an illusion.

It is the heterogeneity that is of some concern. Small tumours (in this thesis <0.22 mL), might easily disappear in the variation of surrounding signal intensities. Some of these small lesions might contain Gleason grades associated with intermediate to high-risk prostate cancer. How are we going to detect these lesions? And is detection and treatment of these small lesions really required?

Model improvement and validation

Step 3: improve tumour detection methods

The model performs very well in our own institute an in our own hands. With implementation of the model, the interpretation of DCE-MRI and DWI will become less observer dependent. To facilitate more widespread use, the model performance has to be validated in other radiotherapy departments on an independent patient cohort and in a different measurement setting. Threshold settings chosen to stratify the model are based upon the positive and negative predictive values, which are influenced by tumour voxel prevalence. Therefore, threshold values might need to be adjusted according to differences in the patient cohort influencing tumour voxel prevalence, for example differences in T-stage. The model is currently validated at the Netherlands Cancer Institute on a large prostatectomy patient cohort from the University Hospitals Leuven. Very first results are promising (data unpublished).

Next step would be the extension of the model from the peripheral zone to the entire prostate gland. Over 70% of prostate tumours arises in the peripheral zone, which is already covered by the model.[13,14] Extension to the central parts of the prostate would however be a challenge, as the imaging characteristics of benign conditions in the central parts of the prostate frequently resemble prostate cancer (chapter 5). Especially BPH is a mimicker of prostate cancer, presenting with high K^{trans} and low ADC values. Adjustment of parameter values will be necessary for tumour segmentation in central prostate regions. Future research might reveal the possibilities of our model to discriminate tumour from benign conditions. Promising results have been obtained by Oto et al., although significant overlap was present, especially between tumour tissue and the stromal variant of BPH.[8]

In the current model the median K^{trans} value of the peripheral zone was used to calculate a relative K^{trans} for every voxel. This method is feasible, unless >50% of the PZ is comprised of tumour. This approach was needed to equalise K^{trans} values among patients. To analyse the DCE-MRI data, a population based arterial input function (AIF) was used instead of a patient-specific AIF. The population based AIF was preferred, as the measurement precision of an exam-specific AIF was not accurate enough (and thereby the repeatability of K^{trans} maps). Patient specific variations are not taken into account and hence K^{trans} values are not comparable among patients. This compels the use of relative K^{trans} values. In the future, improved quantification of DCE-MRI might allow the use of absolute K^{trans} values in the model.[15]

As mentioned previously, the detection of tumour voxels is likely to depend on tissue micro-anatomy and physiology rather than the presence of tumour. The addition of MR imaging techniques measuring specific tumour tissue characteristics might boost tumour detection accuracy. With MR spectroscopy, for example, alterations in tissue metabolism can be assessed.[16,17] However, the spatial resolution of MR spectroscopy is low and has to be improved for detailed prediction of tumour presence.

Clinical relevance: care vs. cure

Step 4: translation to clinical practice: are we ready for focal boost and focal therapy?
What do we aim for?

Major clinical aim of the model development and the investigation of MRI versus histology was to come to robust tumour delineation in the setting of focal boosting for patients with intermediate- to high-risk prostate cancer and focal therapy for patients with low-risk prostate cancer. Although in the previous section some improvements are suggested, the question is whether tumour delineation is yet robust enough for routine implementation in clinical practice. Based on the results of this thesis, it is postulated that the most important tumour voxels are included. These are the voxels from the largest lesions and the voxels with high cell density, HIF-expression and high Gleason scores. However, given the marked heterogeneity of tissue, small tumour areas will always be prone to remain undetected and resemblance between tumour and benign tissue will make perfect discrimination highly challenging.

As the dominant tumour lesion is a leading factor in outcome after radiation treatment, it is both in the scenario of focal boosting and of focal therapy essential to treat this lesion.[18,19] Above all, this condition has to be met.

With focal boosting, non-delineated tumour voxels will receive substantial radiation dose, as still the entire prostate gland is treated with curative intent. In addition, voxels at the boundaries of boost areas will benefit from the limited steepness in dose falloff of the boost area and receive additional dose.

With focal therapy, the non-delineated tumour voxels will be withheld from treatment. Without careful selection of patients, this might have negative impact on treatment outcome. Several selection criteria have been proposed and used in clinical trials. Patients with unifocal prostate cancer, organ confined disease and a maximum Gleason score of 7 seem to be suitable for focal therapy. In addition, patients with multifocal disease are eligible if all secondary tumour foci show features of clinically insignificant disease: total volume < 0.5 mL and Gleason score ≤ 6.[20-22] The debate on selection criteria is still ongoing. Without ignoring its relevance, for extensive discussion of this topic is referred to literature.[23-25]

Aside from the selection criteria for focal therapy, it is likely that treatment concepts have to be changed. Instead of the intention to cure patients, clinicians might change their attitude towards care of patients. The dominant lesion might be eradicated with focal therapy with the least treatment side effects, while with active surveillance an eye is kept on possible progression of less urgent lesions. When needed, focal therapy can be reiterated on a different location in the prostate. Prerequisites for focal therapy are, in addition to treatment of the dominant tumour lesion, the possibility of dosimetry and better or similar cancer specific survival compared to conventional treatment options.

With either focal boosting or focal therapy, treatment of prostate cancer patients will become more personalized. Additionally, with focal therapy, overtreatment of patients will be reduced with patients suffering less from treatment side effects. Several studies are currently ongoing to assess toxicity and survival of focal therapy.[26]

Conclusion

This thesis addressed several aspects regarding prostate tumour voxel detection and delineation, in relation to histological characteristics. Relevant tumour voxels, most in need of aggressive treatment, can be detected with high accuracy. The obtained knowledge of histological characteristics of detected and missed tumour voxels is of relevance when in the future the treatment of prostate cancer becomes more personalized with focal boost and focal therapy.

References

1. Cellini N, Morganti AG, Mattiucci GC, et al. Analysis of intraprostatic failures in patients treated with hormonal therapy and radiotherapy: implications for conformal therapy planning. Int J Radiat Oncol Biol Phys 2002;53:595-9.
2. Pucar D, Hricak H, Shukla-Dave A, et al. Clinically significant prostate cancer local recurrence after radiation therapy occurs at the site of primary tumor: magnetic resonance imaging and step-section pathology evidence. Int J Radiat Oncol Biol Phys 2007;69:62-9.
3. Arrayeh E, Westphalen AC, Kurhanewicz J, et al. Does local recurrence of prostate cancer after radiation therapy occur at the site of primary tumor? Results of a longitudinal MRI and MRSI study. Int J Radiat Oncol Biol Phys 2012;82:e787-93.
4. Webb S, Nahum AE. A model for calculating tumour control probability in radiotherapy including the effects of inhomogeneous distributions of dose and clonogenic cell density. Phys Med Biol 1993;38:653-66.
5. Epstein JI. An update of the Gleason grading system. J Urol 2010;183:433-40.
6. Barentsz JO, Richenberg J, Clements R, et al. ESUR prostate MR guidelines 2012. Eur Radiol 2012;22:746-57.
7. Futterer JJ, Heijmink SW, Scheenen TW, et al. Prostate cancer localization with dynamic contrast-enhanced MR imaging and proton MR spectroscopic imaging. Radiology 2006;241:449-58.
8. Oto A, Kayhan A, Jiang Y, et al. Prostate cancer: differentiation of central gland cancer from benign prostatic hyperplasia by using diffusion-weighted and dynamic contrast-enhanced MR imaging. Radiology 2010;257:715-23.
9. Lips IM, van der Heide UA, Haustermans K, et al. Single blind randomized Phase III trial to investigate the benefit of a focal lesion ablative microboost in prostate cancer (FLAME-trial): study protocol for a randomized controlled trial. Trials 2011;12:255.
10. van der Heide UA, Houweling AC, Groenendaal G, Beets-Tan RG, Lambin P. Functional MRI for radiotherapy dose painting. Magn Reson Imaging 2012;30:1216-23.
11. Roethke MC, Lichy MP, Jurgschat L, et al. Tumorsize dependent detection rate of endorectal MRI of prostate cancer--a histopathologic correlation with whole-mount sections in 70 patients with prostate cancer. Eur J Radiol 2011;79:189-95.
12. Turkbey B, Mani H, Shah V, et al. Multiparametric 3T prostate magnetic resonance imaging to detect cancer: histopathological correlation using prostatectomy specimens processed in customized magnetic resonance imaging based molds. J Urol 2011;186:1818-24.
13. Chen ME, Johnston DA, Tang K, Babaian RJ, Troncoso P. Detailed mapping of prostate carcinoma foci: biopsy strategy implications. Cancer 2000;89:1800-9.
14. Meiers I, Waters DJ, Bostwick DG. Preoperative prediction of multifocal prostate cancer and application of focal therapy: review 2007. Urology 2007;70:3-8.
15. Korporaal JG, van den Berg CA, van Osch MJ, Groenendaal G, van Vulpen M, van der Heide UA. Phase-based arterial input function measurements in the femoral arteries for quantification of dynamic contrast-enhanced (DCE) MRI and comparison with DCE-CT. Magn Reson Med 2011;66:1267-74.
16. Kurhanewicz J, Swanson MG, Nelson SJ, Vigneron DB. Combined magnetic resonance imaging and spectroscopic imaging approach to molecular imaging of prostate cancer. J Magn Reson Imaging 2002;16:451-63.

17. Murphy G, Haider M, Ghai S, Sreeharsha B. The expanding role of MRI in prostate cancer. AJR Am J Roentgenol 2013;201:1229-38.

18. Wise AM, Stamey TA, McNeal JE, Clayton JL. Morphologic and clinical significance of multifocal prostate cancers in radical prostatectomy specimens. Urology 2002;60:264-9.

19. Noguchi M, Stamey TA, McNeal JE, Nolley R. Prognostic factors for multifocal prostate cancer in radical prostatectomy specimens: lack of significance of secondary cancers. J Urol 2003;170:459-63.

20. Karavitakis M, Ahmed HU, Abel PD, Hazell S, Winkler MH. Anatomically versus biologically unifocal prostate cancer: a pathological evaluation in the context of focal therapy. Ther Adv Urol 2012;4:155-60.

21. Barret E, Ahallal Y, Sanchez-Salas R, et al. Morbidity of focal therapy in the treatment of localized prostate cancer. Eur Urol 2013;63:618-22.

22. Bott SR, Ahmed HU, Hindley RG, Abdul-Rahman A, Freeman A, Emberton M. The index lesion and focal therapy: an analysis of the pathological characteristics of prostate cancer. BJU Int 2010;106:1607-11.

23. van den Bos W, Muller BG, Ahmed H, et al. Focal Therapy in Prostate Cancer: International Multidisciplinary Consensus on Trial Design. Eur Urol 2014;.

24. Langley S, Ahmed HU, Al-Qaisieh B, et al. Report of a consensus meeting on focal low dose rate brachytherapy for prostate cancer. BJU Int 2012;109 Suppl 1:7-16.

25. Katz B, Srougi M, Dall'Oglio M, et al. Are we able to correctly identify prostate cancer patients who could be adequately treated by focal therapy? Urol Oncol 2012;30:794-7.

26. *ClinicalTrials.gov*. Feb 4, 2014.

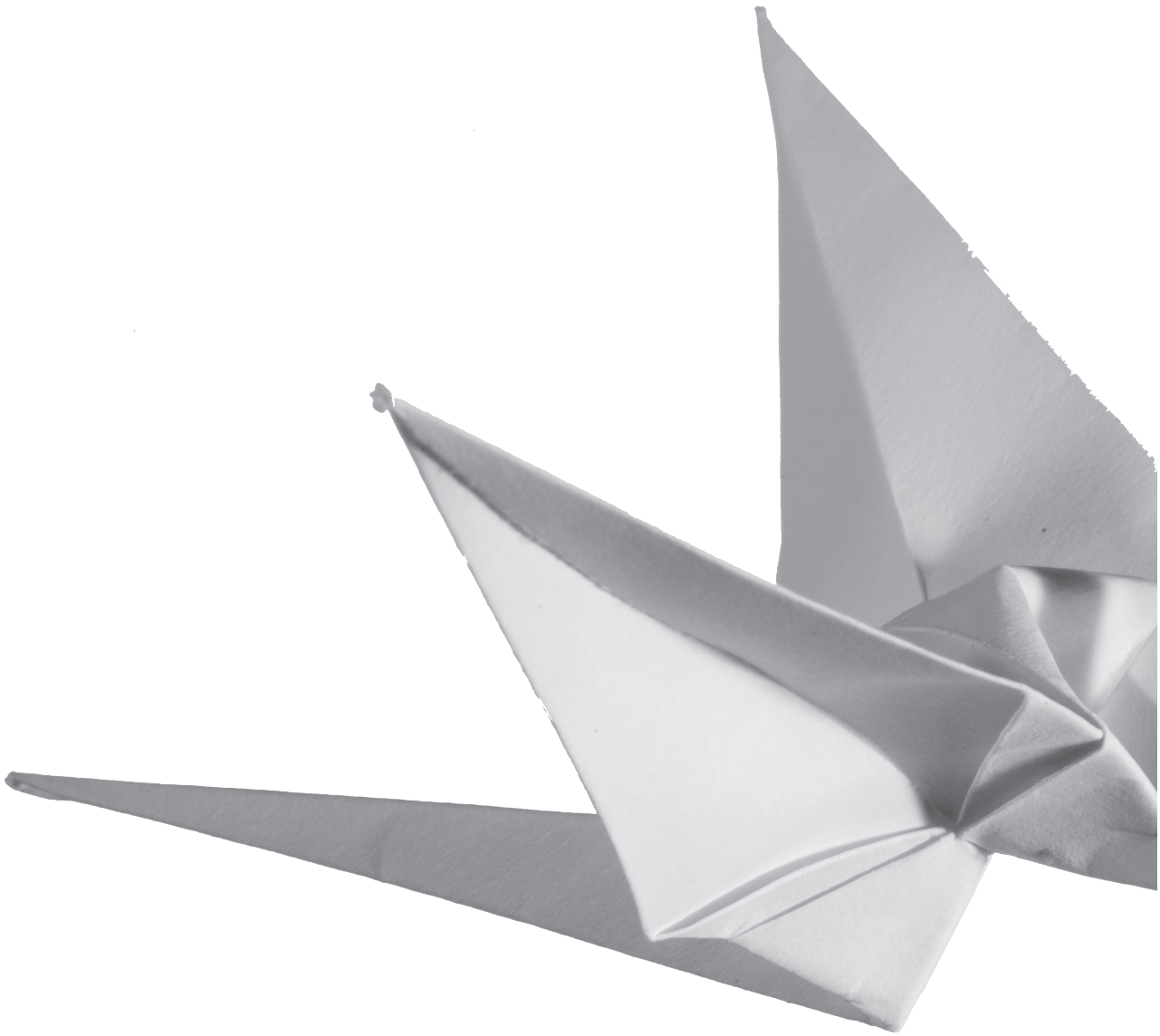

8

Nederlandse samenvatting

Dankwoord

Curriculum Vitae

Klinische achtergrond

Prostaatkanker is één van de meest voorkomende tumoren bij mannen. Het is bekend dat één op de acht mannen deze ziekte zal ontwikkelen voor de leeftijd van 80 jaar. Het beloop van de ziekte kan zowel agressief als indolent zijn. Dit hangt samen met belangrijke factoren als de hoogte van prostaat specifiek antigeen (PSA) in het bloed, het tumor stadium en de Gleason score (een maat voor tumoragressiviteit).
Prostaatkanker komt in veel gevallen op meerdere plaatsen tegelijk voor in de prostaat. Dit is de reden dat tot nog toe de prostaat altijd in zijn geheel behandeld werd. De behandelingsresultaten bij patiënten met laag-risico prostaatkanker zijn erg goed. Bij matig tot hoog-risico prostaatkanker daarentegen, zijn de resultaten minder goed: 15-50% van de patiënten krijgt een PSA-stijging in 5-10 jaar na behandeling met uitwendige radiotherapie. Bij beide patiëntengroepen kan de behandeling met radiotherapie mogelijk verbeterd worden: 1)bij patiënten met laag-risico prostaatkanker door alleen het tumorgebied te bestralen en 2) bij patiënten met matig-hoog risico prostaatkanker door de bestralingsdosis te verhogen.
Het bestralen van de prostaat in zijn geheel gaat vrijwel altijd samen met het ontstaan van bijwerkingen. Dit wordt veroorzaakt door straling die terecht komt op nabijgelegen organen, zoals blaas en darmen. Deze bijwerkingen hebben uiteraard negatieve invloed op de kwaliteit van leven van patiënten. Door heel selectief alleen het tumorgebied in de prostaat te bestralen, kunnen deze bijwerkingen mogelijk beperkt worden.
In het verleden is aangetoond dat het verhogen van de stralingsdosis een positief effect heeft op het ziektebeloop. Het nog verder verhogen van de dosis bij matig tot hoog-risico prostaatkanker zou daarom het aantal biochemisch recidieven (PSA-stijgingen) verder kunnen terug dringen. Het nadeel hiervan is dat de bijwerkingen van de behandeling onacceptabel zullen worden. Een oplossing hiervoor kan zijn om de dosis slechts plaatselijk te verhogen, alleen op het tumorgebied, en de rest van de prostaat de standaard behandeling te geven. Het effect van het geven van zo'n focale boost wordt onderzocht in de FLAME-trial.
In geval van laag-risico prostaatkanker zou de hoeveelheid bijwerkingen verminderd kunnen worden door het toepassen van focale therapie. Hierbij wordt selectief alleen het tumorgebied behandeld en krijgt de rest van de prostaat geen dosis.
Een belangrijke stap bij focale behandeling is het selecteren van tumor gebieden in de prostaat. In het algemeen is er, ook bij multifocale ziekte, een dominante tumorhaard aanwezig. De locatie van deze dominante haard is belangrijk, omdat deze leidend is in het ziektebeloop na behandeling. Het is bekend dat lokale recidieven vaak juist op deze plek worden gezien. Een tweede belangrijk punt is het selecteren van de meest agressieve tumorgebieden. Dit kunnen gebieden zijn met hoge Gleason score, hoge celdichtheid of vaatdichtheid, of hypoxische gebieden.
Multiparametrische MRI is de voorkeursmethode om tumorgebieden te detecteren en in te tekenen voor behandeling met radiotherapie. Hierbij worden anatomische scans gecombineerd met functionele technieken, die informatie geven over de perfusie van weefsel (DCE-MRI) en over de diffusie in het weefsel (DWI). Tumorweefsel heeft vaak een ongeorganiseerd

vaatnetwerk dat bestaat uit kleine en lekke bloedvaten. De perfusie variabele K^{trans}, zoals gemeten met DCE-MRI, zal daardoor hoger zijn in tumor dan in het omringende gezonde weefsel. Verder heeft tumorweefsel vaak een hoge celdichtheid, waardoor de vrije beweging van watermoleculen tussen cellen gehinderd wordt. De ADC-waarde, zoals gemeten met DWI, zal daardoor in tumorweefsel veelal laag zijn.
Ondanks dat dit vrij rechttoe rechtaan klinkt, is het precies intekenen van tumoren een uitdagende zaak. DCE-MRI en DWI brengen verschillende weefseleigenschappen in beeld en overlappen daardoor vaak niet exact. Daarbij komt dat er in de prostaat ook goedaardige aandoeningen voorkomen, zoals benigne prostaat hypertrofie (BPH) en prostatitis. Deze aandoeningen kunnen sterk lijken op tumorweefsel, wat het onderscheid bemoeilijkt. Hoewel het bij de meeste patiënten mogelijk is om handmatig tumoren in te tekenen, is het interpreteren van de MRI beelden regelmatig een ingewikkelde klus.
Het doel van dit proefschrift is om de histologische achtergrond van functionele MRI-beelden te begrijpen, om zo te komen tot meer robuuste en accurate intekening van prostaattumoren.

Model met hoge accuraatheid

Stap 1: handmatig intekenen van tumoren verbeteren door middel van een statistisch model
Om het intekenen van tumoren meer te objectiveren hebben wij een statistisch model ontworpen op basis van DWI en DCE-MRI. Met dit model wordt het risico op aanwezigheid van tumor voorspeld voor elk voxel (3D pixel) in de perifere zone van de prostaat. Uit validatie op prostaathistologie van patiënten die een prostatectomie hebben ondergaan, blijkt dat de accuraatheid van het model goed is. Voor klinische toepasbaarheid, is de continue modeluitkomst (een getal tussen 0 en 1) verdeeld in 3 verschillende risicogroepen: 1) vrijwel zeker tumor (GTV), 2) hoog-risico CTV en 3) onverdacht voor tumor. Deze risicogroepen kunnen gebruikt worden voor het maken van bestralingsplannen, waarbij een hogere dosis gegeven wordt naarmate het risico op tumor toeneemt.

Karateristieken van gedetecteerde vs. niet gedetecteerde tumor voxels

Stap 2: het model is accuraat, maar niet perfect: er worden tumor voxels gemist. Wat zijn de karakteristieken van deze voxels?
Met andere woorden: hoe belangrijk zijn deze gemiste voxels? Zullen zij het effect van een focale boost verminderen? Zijn ze agressief en is het absoluut noodzakelijk om ze te behandelen in geval van focale therapie?
Ondanks de goede accuratesse is de voorspelling van het model niet perfect. Het blijkt dat gedetecteerde tumor voxels hoge celdichtheid en hoge vaatdichtheid hebben en mogelijk ook samengaan met een hogere Gleason score. Aan de andere kant hebben de niet-gedetecteerde tumor voxels celdichtheden en vaatdichtheden die sterk lijken op die van normaal weefsel. Dit

betekent dat het detecteren van tumor voxels afhankelijk is van histologische karakteristieken. Een andere factor die een rol speelt, is het tumorvolume. Grotere tumoren zijn geassocieerd met lagere ADC waarden en hogere expressie van hypoxia-inducible factor (HIF) 2α. Het zijn de grotere tumoren die beter gedetecteerd kunnen worden en die samenhangen met het ziektebeloop na radiotherapie. Deze resultaten duiden erop dat de klinisch meest relevante tumor voxels met het model gedetecteerd worden.
Een belangrijke bevinding in dit proefschrift is de sterke heterogeniteit van prostaatweefsel en van MRI variabelen. Er is forse overlap aanwezig tussen tumorweefsel en normaal weefsel in de prostaat. De variatie in normaal weefsel kan mogelijk verklaard worden door aanwezigheid van de al eerder genoemde goedaardige aandoeningen. Deze variatie heeft tot gevolg dat het lastig is om een duidelijke grens te trekken tussen tumor en normaal weefsel op basis van celdichtheid en vaatdichtheid.
De heterogeniteit van de MRI variabelen kan slechts voor een deel verklaard worden door de variatie in celdichtheid en vaatdichtheid. Dit kan enerzijds te maken hebben met technische problemen. Anderzijds is het gemeten MRI signaal het resultaat van een complex samenspel van diverse factoren, die niet te vangen zijn in enkel celdichtheid en vaatdichtheid.
De heterogeniteit baart enige zorgen. De zichtbaarheid van kleine tumoren kan verloren gaan in de enorme variatie van het omringende weefsel. Het is mogelijk dat enkele van deze kleine laesies matig tot hoog-risico Gleason scores hebben.

Model verbetering en validatie

Stap 3: verbeteren van tumor detectie methoden
Het model werkt goed in onze eigen handen. Validatie in andere patiëntengroepen en andere radiotherapeutische instituten zal uitwijzen of het model ook breder toepasbaar is. Deze validatie vindt plaats in het NKI-AVL in samenwerking met het UZ Leuven. De voorlopige resultaten hiervan zijn veel belovend.
Een volgende stap is de uitbreiding van het model van de perifere zone naar de gehele prostaat. Dit is een hele uitdaging, omdat juist in de meer centrale delen van de prostaat vaak BPH voorkomt.
Tot slot zijn er enkele technische zaken die aandacht behoeven. Dit betreft bijvoorbeeld de K^{trans} waarde, die op een meer patiënt-specifieke manier bepaald zou kunnen worden.

Klinische relevantie: care vs. cure

Stap 4: vertaling naar de klinische praktijk: zijn we er klaar voor om te behandelen met focale boost en focale therapie? Wat willen we precies bereiken?
Het belangrijkste doel van het ontwikkelen van het model en van het onderzoeken van de relatie tussen MRI en histologie was het robuuster maken van tumor intekeningen in het kader

van focale boost en focale therapie. De vraag is of deze methode op dit moment robuust genoeg is om daadwerkelijk te gebruiken in de klinische praktijk. Op basis van de resultaten van dit proefschrift kunnen we stellen dat de belangrijkste tumor voxels geïncludeerd worden. Dit neemt echter niet weg dat het door de heterogeniteit kan voorkomen dat kleine tumorgebieden gemist worden.
Zowel bij focale boost als bij focale therapie is het essentieel om de dominante tumorhaard te behandelen. Aan deze voorwaarde moet boven alles voldaan worden. Verder zullen bij focale boost de niet ingetekende tumor voxels nog steeds behandeld worden met de normale stralingsdosis. Bij focale therapie daarentegen, zullen deze voxels niet behandeld worden. Het is daarom cruciaal om juist die patiënten voor deze behandeling te selecteren, waarbij de kans op aanwezigheid van hoog-risico prostaatkanker minimaal is.
Los van alle selectie criteria, verdient nog een andere overweging de aandacht. Het zou kunnen zijn dat in de toekomst behandelconcepten zullen veranderen. In plaats van patiënten te behandelen met de intentie hen te willen genezen, aangeduid met het Engelse woord 'cure', zouden behandelaars hun intentie kunnen verleggen naar 'care', het zorgen voor. In dit scenario zou de dominante tumorhaard behandeld kunnen worden met focale therapie, terwijl minder urgente tumorhaarden in de gaten gehouden worden door middel van het zogenoemde 'waakzaam wachten'. Indien dit in de loop van de tijd nodig blijkt te zijn, kan de focale therapie dan herhaald worden op een volgende plek in de prostaat.
Welke behandelstrategie er dan ook gekozen wordt, de behandeling van prostaatkanker patiënten zal meer gepersonaliseerd worden.

Conclusie

Dit proefschrift behandelt diverse aspecten ten aanzien van het detecteren van tumor voxels in relatie tot histologische karakteristieken. De meest relevante tumor voxels, die de meest agressieve behandeling behoeven, kunnen accuraat gedetecteerd worden. De verkregen kennis over de histologische kenmerken van zowel gedetecteerde als gemiste voxels is van belang als in de toekomst de behandeling van prostaatkanker meer gepersonaliseerd zal worden met focale boost en focale therapie.

Dankwoord

Promoveren is een uitdagend en dynamisch proces, waarbij veel mensen om mij heen van invloed zijn geweest op het uiteindelijke welslagen. Ik wil iedereen bedanken die, op welke manier dan ook, heeft bijgedragen aan de totstandkoming van dit proefschrift.

Prof. Van Vulpen, beste Marco, dank voor je begeleiding en je oneindige enthousiasme en optimisme. Menig topoverleg met jou heeft alle goede moed in mij aangewakkerd.

Prof. Van Diest, beste Paul, dank voor al je intekenwerk en alle overlegmomenten. Jouw enthousiasme heeft zeker aanstekelijk gewerkt. Ik heb nog geen moment spijt gehad dat ik de weg van de pathologie ben ingeslagen.

Marielle, dank voor je dagelijkse begeleiding. Van alle besprekingen en discussies met jou heb ik veel geleerd. Data werden tot een verhaal en menig puntje werd op de 'i' gezet.

Uulke, als ik jouw mening ergens over nodig had, wist ik dat je reactie snel zou zijn en doeltreffend. Het heeft me diverse keren enorm geholpen.

Petra, fijn dat ik altijd bij je binnen kon lopen. Dank dat je mijn kennis over het doen van immuno's ruimschoots hebt weten bij te schaven. Ik blijf trots op mijn HIF-kleuringen op whole-mount prostaten.

Léonie, Therèse en Judith, dank voor al jullie praktische hulp en gezelligheid. Jullie zijn goud waard.

Dank aan al mijn collega's van de afgelopen jaren: OIO's, arts-onderzoekers en arts-assistenten: als jullie niet zo gezellig waren geweest, was er van dit proefschrift minder terecht gekomen. Al het koffiezetten en drinken, alle luisterende oren en werk- en niet-werk-gerelateerde discussies hebben mijn promotietijd tot een succes gemaakt. Bijzonder dank aan degenen met wie ik intensief heb mogen samenwerken, ik ben blij met alle vruchten die geplukt zijn.

Christel en Tim, mijn kamergenoten van de laatste jaren: de sfeer in onze kamer was top! Dank voor het tolereren van mijn slingers met wetenschappelijke bijproducten. Dank voor alle serieuze en minder serieuze momenten. Jullie zijn geweldig!

Vrienden, dank voor alle keren dat jullie er voor mij waren, luisterden en me gezellige en ontspannen momenten bezorgden.

Broers en zussen, dankzij jullie vereende krachten kon ik twee keer verhuizen tijdens mijn promotie. Dank dat ik altijd op jullie kan rekenen.

Papa en mama, dank voor jullie onvoorwaardelijke steun, interesse en liefde. Dank dat jullie er altijd voor mij zijn.

Tot slot, zonder mijn God was van dit alles niets terecht gekomen.

Soli Deo Gloria

Curriculum Vitae

Aaltje Borren werd geboren op 7 februari 1984 te Harderwijk en groeide op in Garderen. Na het behalen van haar Gymnasium diploma op de Jacobus Fruytier Scholengemeenschap te Apeldoorn begon zij in 2002 met de studie Geneeskunde aan de Universiteit Utrecht. Tijdens haar studie ontdekte zij haar interesse in het doen van onderzoek en gaf dit vorm door als student-onderzoeker te werken op de afdeling Chirurgische Oncologie van het Universitair Medisch Centrum Utrecht. Na haar afstuderen in 2008 zette zij het doen van onderzoek voort door te starten met haar promotieonderzoek op de afdeling Radiotherapie, in samenwerking met de afdeling Pathologie. Dit onderzoek resulteerde in het huidige proefschrift. In april 2013 is zij begonnen met de opleiding tot patholoog in het Academisch Medisch Centrum te Amsterdam.